AD NUMBER

AD227158

LIMITATION CHANGES

TO:

Approved for public release; distribution is unlimited.

FROM:

Distribution authorized to DoD only; Administrative/Operational Use; MAY 1959. Other requests shall be referred to Army Transportation Research and Engineering Command, Fort Eustis, VA.

AUTHORITY

TRECOM ltr Jun 1975

"NOTICE: When Government or other drawings, specifications or other data are used for any purpose other than in connection with a definitely related Government procurement operation, the U.S. Government thereby incurs no responsibility, nor any obligation whatsoever; and the fact that the Government may have formulated, furnished, or in any way supplied the said drawings, specifications or other data is not to be regarded by implication or otherwise as in any manner licensing the holder or any other person or corporation, or conveying any rights or permission to manufacture, use or sell any patented invention that may in any way be related thereto."

PRINCETON UNIVERSITY

DEPARTMENT OF AERONAUTICAL ENGINEERING

AD No. 27158
ASTIA FILE COPY

U.S. Army Transportation Research and Engineering Command
Fort Eustis, Virginia

Project Number : 9-38-01-000 ST112
Contract Number: DA 44-177-TC-392

LONGITUDINAL STABILITY AND CONTROL OF A DUCTED-ROTOR FLYING PLATFORM

by

Joseph J. Traybar
Department of Aeronautical Engineering
Princeton University

Report No. 454 May, 1959

1357

Agencies within the Department of Defense and their contractors may obtain copies of this report on a loan basis from:

Armed Services Technical
Information Agency
Arlington Hall Station
Arlington 12, Virginia

Others may obtain copies from:

Office of Technical Services
Acquisition Section
Department of Commerce
Washington 25, D.C.

The views contained in this report are those of the contractor and do not necessarily reflect those of the Department of the Army. The information contained herein will not be used for advertising purposes.

Prepared by:

Joseph J. Traybar
Joseph J. Traybar
Research Assistant

Approved by:

Edward Seckel
Edward Seckel
Associate Professor

CRD 959

FOREWORD

The research in this Report was conducted by Princeton University under the sponsorship of the United States Army Transportation Research and Engineering Command.

This work was performed under the supervision of Professor Edward Seckel, Department of Aeronautical Engineering, Princeton University, and was administered for the United States Army by Mr. J. Nelson Daniel of the Transportation Research and Engineering Command.

TABLE OF CONTENTS

TABLE OF CONTENTS (cont.)

LIST OF FIGURES

LIST OF FIGURES (cont.)

LIST OF FIGURES (cont.)

LIST OF TABLES

LONGITUDINAL STABILITY AND CONTROL OF A DUCTED-ROTOR FLYING PLATFORM

SUMMARY

An analysis is presented for the prediction of the longitudinal stability and control characteristics of a ducted-rotor flying platform. The stability characteristics of this vehicle are corroborated by the investigations and exhibited rather clearly by various stability diagrams. Artificial stabilization is discussed and can be used to stabilize certain configurations. The predictions of excessive trim requirements and large tilt angles for forward flight are substantiated. Also, the effects of changing duct design and vertical center of gravity location on the stability derivatives are discussed, and material is presented to reflect the degree to which these changes can be used as aids in stabilizing the platform.

LONGITUDINAL STABILITY AND CONTROL OF A DUCTED-ROTOR FLYING PLATFORM

INTRODUCTION

The ducted-rotor Flying Platform is essentially a stand-on type, VTOL, lifting device operated by a pilot. Lift is produced by two, counter-rotating, non-articulated, rotors located below the pilot's stand-on platform and powered by reciprocating engines. (Fig. 1)

The conventional control systems of airplanes and helicopters are eliminated, since control is primarily obtained by the method often referred to as "kinesthetic control". (Ref. 1)

Longitudinal and lateral control is maintained when the pilot, acting as an automatic feedback by his instinctive balancing reactions, provides the correcting moment necessary to control and stabilize the machine after a disturbance. In steady forward flight he provides the required control moment by shifting his weight and leaning in the direction of the desired motion.

Directional control is obtained through the movement of yaw vanes located in the duct and operated by the twist grip handle bars, which also provide a method for power adjustment.

In this Report, all references to the term "Flying Platform" should be construed to mean the subject vehicle.

The purpose of this Report is to predict and understand, by theoretical and analytical studies, the attainable flying qualities associated with the stability and control of the ducted-rotor Flying Platform as affected by changes in duct design, vertical center of gravity location and artificial stabilization.

The ducted-rotor Flying Platform has been flying for many years and several models have been built.

Stability and control problems have developed for the longitudinal mode of motion of these machines. The main difficulties are associated with large nose-up pitching moments, poor gust response, large tilt angles for forward flight and marginal handling qualities.

For the studies in this Report, equations of motion based on small perturbation theory were developed and the static stability derivatives were calculated from data obtained by wind tunnel tests performed at the David Taylor Model Basin. (Ref. 2)

Variations in vertical center of gravity location, together with radically different duct designs, (Fig. 2), were analyzed for their effect on the stability and control of the vehicle.

The effects of artificial stabilization of the type used on vehicles of this design were also considered.

NOTATION

a	slope of blade section lift curve per radian
b	number of blades
c	chord length of duct (ft.)
f	equivalent flat plate area of pilot (approximately 9 sq. ft.)
$h_Y = \frac{I}{\Omega \tau} \left(\frac{k_Y}{R}\right)^2$	non-dimensional moment of inertia parameter (0.0108)
$k_Y = \sqrt{I_Y / m}$	radius of gyration (ft.)
l_p	distance between drag center of pilot and center of gravity of gross weight aircraft (ft.)
m	mass of complete aircraft (slugs)
p	poles for root locus for $\bar{C}_{m_\mu}$
q	dynamic pressure (lbs. per sq. ft.)
t	time (sec.)
x_T	distance between line of action of thrust force and center of gravity of gross weight aircraft (ft.)
z	zero for root locus for $\bar{C}_{m_\mu}$
$z_D \approx l_p \cos \alpha$	distance between line of action of pilot drag force and center of gravity of gross weight aircraft (ft.)
z_H	distance between line of action of H-force and center of gravity of gross weight aircraft (ft.)
A, B, C, D, E	coefficients of the characteristic equation in forward flight
A_H, B_H, C_H, D_H	coefficients of the characteristic equation in hover

$C_1, C_2, C_3, D_1, D_2, D_3$ E_1, E_2	increments to coefficients of characteristic equations for $\bar{C}_{m_\mu}$ and $\bar{C}_{m_\alpha}$ in root locus equation
$C_D = C_D' \mu^2/2$	drag coefficient of pilot where $C_D' = f/S_R$
$C_H = \frac{H}{\rho \pi R^2 (\Omega R)^2}$	H-force coefficient
$C_m = \frac{M}{\rho \pi R^2 (\Omega R)^2 R}$	pitching moment coefficient
$C_T = \frac{T}{\rho \pi R^2 (\Omega R)^2}$	thrust coefficient
$C_W = \frac{W}{\rho \pi R^2 (\Omega R)^2}$	weight coefficient
$C_{T_\alpha} = \frac{\partial C_T}{\partial \alpha}$	static stability force and moment coefficient derivatives, (moments taken about the quarter chord)
$C_{T_\mu} = \frac{\partial C_T}{\partial \mu}$	
$C_{H_\alpha} = \frac{\partial C_H}{\partial \alpha}$	
$C_{H_\mu} = \frac{\partial C_H}{\partial \mu}$	
$C_{m_\alpha} = \frac{\partial C_m}{\partial \alpha}$	
$C_{m_\mu} = \frac{\partial C_m}{\partial \mu}$	
$C_{H_{d(\Delta\theta)}} = \frac{\partial C_H}{\partial d(\Delta\theta)}$	
$C_{m_{d(\Delta\theta)}} = \frac{\partial C_m}{\partial d(\Delta\theta)}$	
$\bar{C}_{T_\alpha}, \bar{C}_{T_\mu}, \bar{C}_{H_\alpha}, \bar{C}_{H_\mu}$ $\bar{C}_{m_\alpha}, \bar{C}_{m_\mu}, \bar{C}_{m_{d(\Delta\theta)}}$	overall values of force and moment coefficient derivatives
$D = f\rho V^2 / 2$	drag force of the pilot (lbs.)
F_h	horizontal force (lbs)
F_X	total force measured along X body axis (lbs.)

F_Z	total force measured along Z body axis (lbs.)
H	total force parallel to rotor disc (lbs.)
$I_Y = mk_Y^2$	pitching moment of inertia of gross weight aircraft (approximately 125 slug-ft.^{2})
K	gain of artificial stabilization feedback loop
L.C.D.	Long Chord Duct
$M = M_{Y_{cg}} - M_P$	pitching moment excluding pilot control moment, measured about Y axis (ft.-lbs.)
$M_{c/4}$	aerodynamic moment created by the aircraft, without pilot, measured about the c/4 point (ft.-lbs.)
M_P	control moment exerted by the pilot (ft.-lbs.)
$M_{Y_{cg}}$	total moment measured about the Y axis (ft.-lbs.)
P	period of oscillation (sec.) also poles for root locus for $\bar{C}_{m_\alpha}$
R	rotor radius (3.5 ft.) also Routh's discriminant
RLBP	abbreviation for Root Locus Break Points
$S_R = \pi R^2$	area of rotor (ft.^{2})
S.C.D.	Short Chord Duct
T	total thrust, force of duct and rotor measured normal to the rotor disc (lbs.) also time to half or double amplitude (sec.) also time constant for phase lag of artificial stabilization feedback loop
V	resultant velocity of aircraft (ft. per sec.)
W	gross weight of complete aircraft including pilot (550 lbs.)

X,Y,Z	body axis system
Z	zero for root locus for $\bar{C}_{m_\alpha}$
α	angle of attack, angle between relative wind vector and plane perpendicular to the rotor axis (radians)
γ	flight path angle measured with reference to horizon (radians)
θ	aircraft pitch angle with reference to horizon (radians)
λ	root of the characteristic equation
$\mu = \frac{V}{\Omega R}$	tip speed ratio or velocity ratio
ρ	air density (slugs per cubic ft.)
$\tau = \frac{m}{\rho \pi R^2 \Omega R}$	aerodynamic time (sec.)
Ω	rotor angular velocity (radians per sec.)

General

$d \equiv \frac{d(\ )}{d(t/\tau)}$ $d^2 \equiv \frac{d^2(\ )}{d(t/\tau)^2}$	differential operator forms for time ratio t/τ
$(\dot{}) \equiv \frac{d(\ )}{dt}$ $(\ddot{}) \equiv \frac{d^2(\ )}{dt^2}$	differential operator forms for time t
$(\ )_o$	subscript zero designates initial condition before perturbation
$\Delta(\ )$	designates perturbation quantities

DEVELOPMENT

Equations of Longitudinal Motion

The development of the equations of motion for this system is based on the commonly used methods for the study of aeronautical dynamics. The basic theory is the familiar small perturbation theory that assumes the disturbed motion of the aircraft to be one of small oscillations about some steady-state flight condition.

As usual, the equations of motion are written in accordance with the Newtonian laws of motion with the important requirement that all accelerations and rates of change of moments of momentum must be expressed along axes fixed in space.

Equations of motion, as well as other important work in this area, have been developed at the Advanced Research Division of Hiller Aircraft Company by G. J. Sissingh and A. H. Sacks.

Also, dynamic stability of a machine similar to a Flying Platform has been treated at Princeton University in Refs. 3 and 4.

The development of the equations of motion in this Report follows the latter work, the principle differences being in definition and notation.

For the specific case of the longitudinal motion of the Flying Platform, we have a dynamic system with three degrees of freedom; namely, translation forward or backward, translation upward or downward and rotation about the pitch axis.

This system will be described sufficiently by three equations of motion for the so-called control-fixed case similar to that studied in airplane dynamics. The control-fixed case of the Flying Platform can be thought of as the condition where the pilot remains rigid on the Platform, from the initial condition, and induces no new or additional increments of control movement throughout the motion to be studied.

In order to facilitate the description of these motions, choice is made of the Eulerian or moving axis system fixed within the aircraft and always moving with it. For this axis system, the standard N.A.S.A. right-hand axis system is selected with the positive X, Y, Z, axes in the forward, right side, and downward directions respectively. Choosing these axes as body axes, the origin will always be located at the center of gravity and will move slightly with respect to the aircraft whenever the center of gravity is shifted. The positive X axis is directed toward the front of the aircraft, parallel to the rotor plane, and aligned with the relative wind in azimuth but not necessarily in pitch. The positive Z axis is directed downward, perpendicular to the rotor plane, i.e. aligned parallel to the thrust line or rotor shaft.

The Y axis will be the aircraft pitching axis located at the center of gravity. This axis system, with notation for the forces, moments, and displacements, is shown in Fig. 3.

In this discussion, the forces and moments to be resolved along and about the body axis system, together with other notation, are described as follows:

$M_{Y_{c.g.}}$ total moment measured about the Y axis located at the center of gravity. Clockwise or nose-up moments are considered positive.

$M_{c/4}$ aerodynamic moment created by the aircraft without pilot and measured positive clockwise (nose-up) about the quarter chord point. (This notation arises from the wind tunnel balance design for measuring H-force and moments in connection with data reduction when transferring moments to an arbitrary

axis located at the so-called quarter chord point. This quarter chord axis is parallel to the Y axis and passes through the thrust line at the quarter chord point.)

W — total gross weight of the aircraft, including pilot and all components.

T — force measured positive upward along rotor shaft line, perpendicular to the rotor plane and parallel, but directed opposite to the positive Z direction.

H — force measured perpendicularly to T force and in the X direction. It is taken as acting in the quarter chord plane parallel to the rotor plane. The H-force is positive (as in the case of forward flight) when acting aft or in the negative X direction.

D — drag of the pilot measured parallel to the relative wind and acting at the drag center of the pilot. Drag Center and center of gravity location of the pilot alone were assumed to coincide. Also, aerodynamic lift caused by the pilot was assumed to be negligible.

x_T — moment arm for T force or displacement of center of gravity from thrust line measured along X direction. Distance is positive when center of gravity is displaced aft of thrust line, and negative when forward of thrust line as in the case of forward flight.

z_D — moment arm for drag force of pilot where $z_D \approx l_p \cos\alpha$ and l_p is the distance from the total center of gravity position to the drag center of the pilot as shown in Fig. 1.

z_H moment arm for H-force or distance along Z direction, between the center of gravity and the line of H-force.

α angle of attack, measured between the rotor tip path plane and the relative wind where nose-up is positive alpha. (Alpha is negative in forward flight.)

θ attitude or pitch angle, measured between rotor tip path plane and the horizon where nose-up is positive theta.

γ flight path angle measured to the horizon. As shown in Fig. 3, $\gamma = \theta - \alpha$ where gamma is negative as shown.

In the development of the equations of motion of the Flying Platform, it is assumed that the disturbed motion of the aircraft is one of small displacements or oscillations about each steady-state equilibrium-trim flight condition. This steady-state equilibrium-trim condition is achieved whenever the summation of all the aerodynamic and gravity forces acting on the aircraft equals zero. Also, with regard to the inertia terms, the Newtonian laws of motion apply to any axis system, provided that the forces and moments are resolved along and about the particular axis system and that the accelerations expressed along and about these axes are the true accelerations with reference to fixed space.

With these considerations the dynamic equations of motion may be written in the form:

$$\sum F_X = F_{X_{AERODYNAMIC}} + F_{X_{GRAVITY}} + F_{X_{INERTIA}} = 0 \qquad (1a)$$

$$\sum F_Z = F_{Z_{AERODYNAMIC}} + F_{Z_{GRAVITY}} + F_{Z_{INERTIA}} = 0 \qquad (1b)$$

$$\sum M_{Y_{c.g.}} = M_{Y_{c.g._{AERODYNAMIC}}} + M_{Y_{c.g._{INERTIA}}} = 0 \qquad (1c)$$

Resolving the aerodynamic and gravity contributions along body axes (Fig. 3), the steady-state equations of motion become:

$$F_{X_A} + F_{X_G} = -H - D\cos\alpha - W\sin\theta = 0 \tag{2a}$$

$$F_{Z_A} + F_{Z_G} = -T - D\sin\alpha + W\cos\theta = 0 \tag{2b}$$

$$M_{Y_{c.g._A}} = M_{c/4} - H\cdot z_H + T\cdot x_T + D\cdot z_D = 0 \tag{2c}$$

Using the small angle assumptions where:

$$\sin\alpha \approx \alpha \qquad \cos\alpha \approx 1$$
$$\sin\theta \approx \theta \qquad \cos\theta \approx 1 \tag{3}$$

the steady-state equations are:

$$F_{X_A} + F_{X_G} = -H - D - W\theta = 0 \tag{4a}$$

$$F_{Z_A} + F_{Z_G} = -T - \alpha D + W = 0 \tag{4b}$$

$$M_{Y_{c.g._A}} = M_{c/4} - H\cdot z_H + T\cdot x_T + D\cdot z_D = 0 \tag{4c}$$

Expressing the inertia contributions by using the Newtonian frame of reference of fixed axes and body axes as the moving axes, the inertia terms become:

$$F_{x_i} = -m\dot{V}\cos\alpha - mV\dot{\gamma}\sin\alpha = -m\dot{V} - \alpha mV\dot{\gamma} \tag{5a}$$

$$F_{z_i} = mV\dot{\gamma}\cos\alpha - m\dot{V}\sin\alpha = mV\dot{\gamma} - m\dot{V}\alpha \tag{5b}$$

$$M_{Y_{c.g.;}} = -I_Y \ddot{\theta} \tag{5c}$$

These inertia terms arise when an aircraft accelerates along a curved flight path as shown in Fig. 4, where the forces and moments are expressed as d'Alembert's inertia-resistance reactions. It should be noted that the Z component of $m\dot{V}$ namely, the contribution $- m\dot{V}\alpha$, is small compared to the contribution of the Z component of centrifugal force $mV\dot{\gamma}$ and is hereafter omitted from F_{Z_i}, since it is assumed to be a higher order term. No similar conclusions can be made about the relative size of the X components of these forces so that both contributions must be retained in F_{X_i}.

Summing all the forces and moments as stated in Eq. 1, the longitudinal dynamic equations of motion for the Flying Platform become:

H-Force Equation

$$\Sigma F_x = -H - D - W\theta - m\dot{V} - \alpha m V\dot{\gamma} = 0 \tag{6a}$$

Thrust Equation

$$\Sigma F_z = -T - \alpha D + W + mV\dot{\gamma} = 0 \tag{6b}$$

Moment Equation

$$\Sigma M_{Y_{c.g.}} = M_{c/4} - H \cdot z_H + T \cdot x_T + D \cdot z_D - I_Y \ddot{\theta} = 0 \tag{6c}$$

In addition to the small perturbation assumptions, it is assumed that the changes in the external forces and moments acting on the Platform, because of the small departure from steady-state motion, will depend entirely on the displacement and disturbance velocities along and about the aircraft axis, and also that the frequency of the motions is low so that the external forces and moments do not depend on the accelerations involved.

Expanding all the aerodynamic forces and moments of the former set of equations as a Taylor series in the appropriate variables, but neglecting the higher order terms;

$$T = T_0 + \frac{\partial T}{\partial \mu}\Delta\mu + \frac{\partial T}{\partial \alpha}\Delta\alpha + \cdots \tag{7a}$$

$$H = H_0 + \frac{\partial H}{\partial \mu}\Delta\mu + \frac{\partial H}{\partial \alpha}\Delta\alpha + \frac{\partial H}{\partial \dot{\theta}}\Delta\dot{\theta} + \cdots \tag{7b}$$

$$D = D_0 + \frac{\partial D}{\partial \mu}\Delta\mu + \cdots \tag{7c}$$

$$M_{c/4} = M_{0_{c/4}} + \frac{\partial M_{c/4}}{\partial \mu}\Delta\mu + \frac{\partial M_{c/4}}{\partial \alpha}\Delta\alpha + \frac{\partial M_{c/4}}{\partial \dot{\theta}}\Delta\dot{\theta} + \cdots \tag{7d}$$

and letting:

$$\begin{array}{lll} \alpha = \alpha_0 + \Delta\alpha & \dot{\alpha} = \dot{\alpha}_0 + \Delta\dot{\alpha} & \dot{\alpha} = \Delta\dot{\alpha} \\ \theta = \theta_0 + \Delta\theta & \dot{\theta} = \dot{\theta}_0 + \Delta\dot{\theta} & \dot{\theta} = \Delta\dot{\theta} \\ V = V_0 + \Delta V & \dot{V} = \dot{V}_0 + \Delta\dot{V} & \dot{V} = \Delta\dot{V} \\ \gamma = \theta - \alpha & \dot{\gamma} = \dot{\theta} - \dot{\alpha} & \end{array} \tag{8}$$

where the delta variables denote the perturbations and $\dot{\alpha}_0$, $\dot{\theta}_0$ and $\dot{V}_0$ are equal to zero, since it is assumed that the motion takes place about some steady-state trimmed flight condition where the initial rates are zero.

Also, during the disturbed motion of the aircraft, the rotor angular velocity Ω is assumed constant, so that $\Delta\mu = \Delta V/\Omega R$.

Now solving the longitudinal dynamic equations (Eq. 6) in terms of the perturbations, the convenient substitution of Eq. 6b into Eq. 6a may be made:

$$mV\dot{\gamma} = T + \alpha D - W \tag{6b}$$

so that Eq. 6a becomes:

$$\Sigma F_x = -m\dot{V} - \alpha(T + \alpha D - W) - H - D - W\theta = 0 \tag{9}$$

Substituting Eq. 7 and Eq. 8 into Eq. 9 and neglecting higher order terms, the H-Force equation becomes:

$$\Sigma F_x = -m\dot{V} - H_o - D_o - W\theta_c - \alpha(T_o - W + \alpha_o D_o) - \alpha_o \frac{\partial T}{\partial \mu}\Delta\mu \tag{10}$$
$$-\alpha_o \frac{\partial T}{\partial \alpha}\Delta\alpha - \frac{\partial H}{\partial \alpha}\Delta\alpha - \frac{\partial H}{\partial \dot{\theta}}\Delta\dot{\theta} - \frac{\partial D}{\partial \mu}\Delta\mu - W\Delta\theta = 0$$

For the initial steady-state condition (subscript o) before any acceleration occurred, Eq. 4 may be written as:

$$-H_o - D_o - W\theta_c = 0 \tag{11a}$$

$$-T_o - \alpha_o D_o + W = 0 \tag{11b}$$

$$M_{c/4} - H_o \cdot z_H + T_o \cdot x_T + D_o \cdot z_D = 0 \tag{11c}$$

Substituting Eq. 11a and Eq. 11b in Eq. 10 reduces the H-Force equation to:

$$0 = -m\dot{V} - \alpha_0 \frac{\partial T}{\partial \mu}\Delta\mu - \alpha_0 \frac{\partial T}{\partial \alpha}\Delta\alpha - \frac{\partial H}{\partial \mu}\Delta\mu$$

$$- \frac{\partial H}{\partial \alpha}\Delta\alpha - \frac{\partial H}{\partial \dot{\theta}}\Delta\dot{\theta} - \frac{\partial D}{\partial \mu}\Delta\mu - W\Delta\theta \qquad (12)$$

Non-dimensionalizing this equation by dividing Eq. 12 by $\rho\pi R^2 (\Omega R)^2$ and treating the drag term as:

$$C_D = \frac{D}{\rho\pi R^2 (\Omega R)^2} = \frac{\frac{1}{2} f V^2}{\rho\pi R^2 (\Omega R)^2} = \frac{f\mu^2}{2 S_R} = C_D' \frac{\mu^2}{2} \qquad (13a)$$

where:

$$C_D' = \frac{f}{S_R} \qquad (13b)$$

then:

$$\frac{\partial C_D}{\partial \mu} = \frac{\partial}{\partial \mu}\left(C_D' \frac{\mu^2}{2}\right) = C_D' \frac{\partial}{\partial \mu}\left(\frac{\mu^2}{2}\right) = \mu C_D' \qquad (14)$$

Also introducing the aerodynamic time parameter:

$$\tau = \frac{m}{\rho\pi R^2 \Omega R} \qquad (15)$$

and using the notation:

$$d(\ ) \equiv \frac{d(\ )}{d(t/\tau)} \qquad (16)$$

where time is counted in the dimensionless time ratio t/τ , the H-Force equation in the usual aerodynamic form is:

$$\left[C_{H_\mu} + \alpha_s C_{T_\mu} + \mu_o C_D' + d\right]\Delta\mu + \left[C_{H_\alpha} + \alpha_o C_{T_\alpha}\right]\Delta\alpha$$

$$+\left[C_W + C_{H_{d(\Delta\theta)}} \cdot d\right]\Delta\theta = 0 \qquad (17)$$

The thrust force equation may be developed directly from Eq. 6b using the same methods:

$$m V \dot{\gamma} - T - \alpha D + W = 0 \qquad (6b)$$

and using Eq. 15 and Eq. 16 with Eq. 8:

$$d\gamma = d\theta - d\alpha$$

$$d\theta = d(\Delta\theta)$$

$$d\alpha = d(\Delta\alpha) \qquad (8')$$

the thrust force equation becomes:

$$\left[C_{T_\mu} + \alpha_o/\mu_o C_D'\right]\Delta\mu + \left[C_{T_\alpha} + \frac{\mu_o^2}{2} C_D' + \mu_o d\right]\Delta\alpha - \left[\mu_o d\right]\Delta\theta = 0 \qquad (18)$$

For the moment equation (Eq. 6c) non-dimensionalization is accomplished by using $\rho\pi R^2 (\Omega R)^2 R$, and defining $I_Y = mk_Y^2$ or:

$$k_Y = \sqrt{\frac{I_Y}{m}} \qquad \text{and} \qquad h_Y = \frac{1}{\Omega\tau}\left(\frac{k_Y}{R}\right)^2 \qquad (19)$$

where k_Y is the radius of gyration and h_Y is the non-dimensional moment of inertia parameter.

The moment equation is:

$$\left[C_{m_\mu} + C_{T_\mu} \cdot \frac{X_T}{R} - C_{H_\mu} \cdot \frac{Z_H}{R} + \mu_0 C_D' \frac{Z_D}{R}\right]\Delta\mu + \left[C_{m_\alpha} + C_{T_\alpha} \cdot \frac{X_T}{R} - C_{H_\alpha} \cdot \frac{Z_H}{R}\right]\Delta\alpha + \left[C_{m_{\alpha(\Delta\theta)}} \cdot \alpha - C_{H_{\alpha(\Delta\theta)}} \cdot \frac{Z_H}{R} \cdot \alpha - h_Y \alpha^2\right]\Delta\theta = 0 \quad (20)$$

Hence, the three equations of motion in familiar aerodynamic form are Eqs. 17, 18, and 20:

H-Force Equation

$$\left[C_{H_\mu} + \alpha_0 C_{T_\mu} + \mu_0 C_D' + \alpha\right]\Delta\mu + \left[C_{H_\alpha} + \alpha_0 C_{T_\alpha}\right]\Delta\alpha + \left[C_W + C_{H_{\alpha(\Delta\theta)}} \cdot \alpha\right]\Delta\theta = 0 \quad (17)$$

Thrust Equation

$$\left[C_{T_\mu} + \alpha_0 \mu_0 C_D'\right]\Delta\mu + \left[C_{T_\alpha} + \frac{\mu_0^2}{2} C_D' + \mu_0 \alpha\right]\Delta\alpha - \left[\mu_0 \alpha\right]\Delta\theta = 0 \quad (18)$$

Moment Equation

$$\left[C_{m_\mu} + C_{T_\mu} \cdot \frac{X_T}{R} - C_{H_\mu} \frac{Z_H}{R} + \mu_0 C_D' \frac{Z_D}{R}\right]\Delta\mu + \left[C_{m_\alpha} + C_{T_\alpha} \cdot \frac{X_T}{R} - C_{H_\alpha} \cdot \frac{Z_H}{R}\right]\Delta\alpha + \left[C_{m_{\alpha(\Delta\theta)}} \cdot \alpha - C_{H_{\alpha(\Delta\theta)}} \cdot \frac{Z_H}{R} \cdot \alpha - h_Y \alpha^2\right]\Delta\theta = 0 \quad (20)$$

Explanation of the Terms of the Equations of Motion

The three equations of motion are simultaneous, homogeneous, ordinary, differential equations with constant coefficients. These constant coefficients are expressed by stability derivatives, velocity ratios, a non-dimensional inertia parameter, angle measurements and drag coefficients. In this Report, the stability derivatives C_{H_μ}, C_{H_α}, C_{T_μ}, C_{T_α}, C_{m_μ} and C_{m_α} are evaluated from data obtained by wind tunnel experiment. The method of evaluating the stability derivatives and drag terms is explained in the Appendices.

The individual terms, expressed in non-dimensional or coefficient form, in the equations of motion, in effect, represent the following:

Term

1. $C_{H_\mu} \cdot \Delta\mu$ represents the H-Force due to the change $\Delta\mu$ in the velocity ratio where C_{H_μ} is the rate of change of H-Force coefficient with velocity ratio. For the case of C_{H_μ}, H-Force obtained from wind tunnel data included the measurement of all the aerodynamic forces of the rotor and duct assembly acting normal to the thrust axis.

2. $C_{H_\alpha} \cdot \Delta\alpha$ represents the H-Force due to a change $\Delta\alpha$ in the angle of attack where C_{H_α} is the rate of change of H-Force coefficient with angle of attack.

3. $C_{T_\mu} \cdot \Delta\mu$ represents the thrust force due to a change $\Delta\mu$ in velocity ratio where C_{T_μ} is the rate of change of thrust force coefficient with velocity ratio.

For the case of C_{T_μ}, thrust force obtained from the wind tunnel data, included the measurement of all the aerodynamic forces of the rotor and duct assembly acting along the thrust axis.

4. $C_{T_\alpha} \cdot \Delta\alpha$ represents the thrust force due to the change $\Delta\alpha$ in angle of attack where C_{T_α} is the rate of change of thrust

force coefficient with angle of attack.

5. $\mu_o C_D' \Delta\mu$ represents the drag force in the X direction contributed by the pilot due to the change $\Delta\mu$ in the velocity ratio. The term C_D' equals $\frac{f}{S_R}$ and μ_o is the initial, steady-state velocity ratio.

(See Appendix I for additional explanation of terms 5, 6, and 7.)

6. $\alpha_o \mu_o C_D' \Delta\mu$ represents the drag force in the Z direction, contributed by the pilot, due to the change $\Delta\mu$ in the velocity ratio. The initial, steady-state angle of attack is defined as α_o.

7. $\frac{\mu_o^2}{2} C_D' \Delta\alpha$ represents the drag force in the Z direction contributed by the pilot due to the change $\Delta\alpha$ in the angle of attack.

8. $C_{m_\mu} \cdot \Delta\mu$ represents the moment contribution measured about the quarter chord point, due to the change $\Delta\mu$ in the velocity ratio where C_{m_μ} is the stability derivative denoting the rate of change of pitching moment coefficient about the quarter chord point with velocity ratio.

The stability derivative C_{m_μ} was evaluated in wind tunnel experiments by measuring the moment created by the duct and rotor only. This moment was arbitrarily transferred to the quarter chord point for convenience in accomplishing additional transfers when vertical c.g. location was varied in order to study the effect on the stability derivatives. Changes in vertical c.g. location change the distances z_H, x_T, and z_D.

9. $C_{m_\alpha} \cdot \Delta\alpha$ represents the moment contribution measured about the quarter chord point due to the change $\Delta\alpha$ in the angle of attack where C_{m_α} is the rate of change of pitching moment coefficient about the quarter chord point with angle of attack. This derivative was evaluated as explained in term 8.

10. $\frac{x_T}{R} C_{T_\mu}$ $\Delta\mu$ represents the moment contribution about the center of gravity due to the thrust force $C_{T_\mu} \cdot \Delta\mu$ acting at the moment arm x_T.

11. $\frac{x_T}{R} C_{T_\alpha}$ $\Delta\alpha$ represents the moment contribution about the center of gravity due to the thrust force $C_{T_\alpha} \cdot \Delta\alpha$ acting at the moment arm x_T.

12. $\frac{z_H}{R} C_{H_\mu} \cdot \Delta\mu$ represents the moment contribution about the center of gravity due to the H-Force $C_{H_\mu} \cdot \Delta\mu$ acting at the moment arm z_H.

13. $\frac{z_H}{R} C_{H_\alpha} \cdot \Delta\alpha$ represents the moment contribution about the center of gravity due to the H-Force $C_{H_\alpha} \cdot \Delta\alpha$ acting at the moment arm z_H.

14. $\frac{z_D}{R} \mu_o C_D' \Delta\mu$ represents the moment contribution about the center of gravity due to the drag force $\mu_o C_D' \Delta\mu$ acting parallel to the relative wind. The perpendicular distance from the center of gravity to the line of action of this drag force is the moment arm z_D.

15. $C_W \Delta\theta$ represents the weight force component in the X direction due to a change $\Delta\theta$ in attitude angle of the machine. For the component $C_W\theta$ in the X direction, $C_W\theta_o$ drops out from Eq. 12 due to the initial condition (Eq. 11a) so that:

$$C_W\theta = C_W\theta_o + C_W\Delta\theta$$

or:

$$C_W\theta = C_W \Delta\theta$$

However, in the thrust equation, the weight term has no perturbation component and drops out entirely from Eq. 6b due to Eq. 11b.

16. $C_{H_{d(\Delta\theta)}} \cdot d(\Delta\theta)$ represents the additional H-Force due to the linear velocity caused by an angular pitch rate $d(\Delta\theta)$ about the center of gravity.

The derivative $C_{H_{d(\Delta\theta)}}$ represents the rate of change of H-Force coefficient with pitching velocity $d(\Delta\theta)$.

17. $\frac{z_H}{R} \cdot C_{H_{d(\Delta\theta)}} \cdot d(\Delta\theta)$ represents the moment contribution about the center of gravity due to the H-Force $C_{H_{d(\Delta\theta)}}$ acting at the moment arm z_H. This term can be thought of as a contribution to the damping in pitch of the aircraft.

18. $C_{m_{d(\Delta\theta)}} \cdot d(\Delta\theta)$ represents the moment contribution due to the pitch rate $d(\Delta\theta)$. This term is the familiar pitch damping term and in these equations refers to the pitch damping created by the rotor and duct. Determination of this value is difficult but an attempt has been made to evaluate the rotor and duct contribution to pitch damping in Appendix II.

19. $d(\Delta\mu)$ represents the component along the X axis of the inertia term due to a linear acceleration of the aircraft.

20. $\mu_o d(\Delta\alpha) - \mu_o d(\Delta\theta)$-----taken together, these terms represent the component along the Z axis of the centrifugal force inertia term caused by the rate of change of flight path angle $\dot{\gamma}$.

21. $\alpha_o C_{T_\mu} \Delta\mu + \alpha_o C_{T_\alpha} \Delta\alpha$ -----taken together, these terms represent the component along the X axis of the centrifugal force inertia term caused by the rate of change of flight path angle $\dot{\gamma}$. The form of this term is due to the substitution performed in Eq. 9 where Eq. 6b:

$$mV\dot{\gamma} = T + L - D - W \qquad (6b)$$

was substituted into the H-Force equation as a matter of convenience in solving the set of equations. If Eq. 6a had been solved as it stands, this inertia term would have been in a form similar to term 20 in the thrust equation. However, the centrifugal force component in the X direction, $mV\dot{\gamma}\alpha$, of Eq. 6a, after the mathematical substitution and operations, takes the form of term 21:

$$\alpha_0 C_{T_\mu} \Delta\mu - \alpha_0 C_{T_\alpha} \Delta\alpha = mV\dot{\gamma}\alpha$$

This indicates that this body axis inertia term is now represented by components of forces parallel to the relative wind. All terms in the original equations represent the summation of forces and moments along and about body axes and, in this case, because of the aforementioned substitution, the body axis inertia force is represented by components of forces parallel to the relative wind. However, these still represent only the body axis inertia term and the equations are still consistent with the body axis frame of reference. Changes in variables and substitutions among the set of Eq. 6 in no way change the validity or meaning of the original body axes equations of motion describing the dynamic system.

22. $h_Y d^2(\Delta\theta)$ represents the pitching moment inertia term due to the distribution of the mass of the vehicle where h_Y is the non-dimensional moment of inertia parameter measured about the Y axis. The term $d^2(\Delta\theta)$ represents the perturbation angular acceleration about the Y axis measured with respect to the time ratio (t/τ) as indicated by the symbol (d).

Solution of the Equations of Motion

In order to solve the equations of motion the form is altered slightly by letting:

$$\bar{C}_{H_\mu} = C_{H_\mu} + \alpha_o C_{T_\mu} + \mu_o C_D' \tag{21a}$$

$$\bar{C}_{H_\alpha} = C_{H_\alpha} + \alpha_o C_{T_\alpha} \tag{21b}$$

$$\bar{C}_{T_\mu} = C_{T_\mu} + \alpha_o \mu_o C_D' \tag{21c}$$

$$\bar{C}_{T_\alpha} = C_{T_\alpha} + \frac{\mu_o^2}{2} C_D' \tag{21d}$$

$$\bar{C}_{m_\mu} = C_{m_\mu} + \frac{X_T}{R} \cdot C_{T_\mu} - \frac{Z_H}{R} C_{H_\mu} + \frac{Z_D}{R} \mu_o C_D' \tag{21e}$$

$$\bar{C}_{m_\alpha} = C_{m_\alpha} + \frac{X_T}{R} C_{T_\alpha} - \frac{Z_H}{R} C_{H_\alpha} \tag{21f}$$

$$\bar{C}_{m_{Z(\Delta\theta)}} = C_{m_{Z(\Delta\theta)}} - \frac{Z_H}{R} C_{H_{Z(\Delta\theta)}} \tag{21g}$$

where the bars over the stability derivatives indicate the overall or total values of the forces and moments of each specific derivative acting along or about the axes.

From the above notations, it is possible to see that changes in vertical c.g. location will affect the values of $\bar{C}_{m_\mu}$ and $\bar{C}_{m_\alpha}$ because of

changes in z_H, z_D, and x_T. The term $\bar{C}_{m_{d(\Delta\theta)}}$ will not change radically since $C_{H_{d(\Delta\theta)}}$ is a rather small quantity.

Also, the moment of inertia about the Y axis I_Y, is held constant for this dynamic analysis.

Using this notation, Eqs. 17, 18 and 20 take the form:

H-Force Equation:

$$\left[\bar{C}_{H_\mu} + d\right]\Delta\mu + \left[\bar{C}_{H_\alpha}\right]\Delta\alpha + \left[C_W + C_{H_{d(\Delta\theta)}} \cdot d\right]\Delta\theta = 0 \qquad (22a)$$

T-Force Equation

$$\left[\bar{C}_{T_\mu}\right]\Delta\mu + \left[\bar{C}_{T_\alpha} + \mu_o d\right]\Delta\alpha - \left[\mu_o d\right]\Delta\theta = 0 \qquad (22b)$$

Moment Equation

$$\left[\bar{C}_{m_\mu}\right]\Delta\mu + \left[\bar{C}_{m_\alpha}\right]\Delta\alpha + \left[\bar{C}_{m_{d(\Delta\theta)}} \cdot d - h_Y d^2\right]\Delta\theta = 0 \qquad (22c)$$

The equations of motion are three simultaneous differential equations with constant coefficients, the solutions of which may be obtained by assuming a solution in the form:

$$\Delta\mu = \Delta\mu_1 e^{\lambda t/\tau} \qquad \Delta\alpha = \Delta\alpha_1 e^{\lambda t/\tau} \qquad \Delta\theta = \Delta\theta_1 e^{\lambda t/\tau} \qquad (23)$$

and:

$$d(\Delta\theta) = \Delta\theta_1 \lambda e^{\lambda t/\tau} \qquad d^2(\Delta\theta) = \Delta\theta_1 \lambda^2 e^{\lambda t/\tau} \qquad (24)$$

where λ is a real or complex constant of equal value for each variation, and where $\Delta\mu_1$, $\Delta\alpha_1$, and $\Delta\theta_1$, are also real or complex constants.

Substituting Eq. 23 and Eq. 24 into Eq. 22, and dividing out the common term $e^{\lambda t/\tau}$, reduces Eq. 22 to three algebraic equations in the unknown λ and the terms $\Delta\mu_1$, $\Delta\alpha_1$ and $\Delta\theta_1$:

$$\left[\bar{C}_{H_\mu} + \lambda\right]\Delta\mu_1 + \left[\bar{C}_{H_\alpha}\right]\Delta\alpha_1 + \left[C_W + C_{H_{\dot{\alpha}(\Delta\theta)}}\cdot\lambda\right]\Delta\theta_1 = 0 \qquad (25a)$$

$$\left[\bar{C}_{T_\mu}\right]\Delta\mu_1 + \left[\bar{C}_{T_\alpha} + \mu_0\lambda\right]\Delta\alpha_1 - \left[\mu_0\lambda\right]\Delta\theta_1 = 0 \qquad (25b)$$

$$\left[\bar{C}_{m_\mu}\right]\Delta\mu_1 + \left[\bar{C}_{m_\alpha}\right]\Delta\alpha_1 + \left[\bar{C}_{m_{\dot{\alpha}(\Delta\theta)}}\lambda - k_Y\lambda^2\right]\Delta\theta_1 = 0 \qquad (25c)$$

It is a property of this type of equation that there can be non-zero values of the unknowns only when the determinant of the coefficients is equal to zero:

$$\begin{vmatrix} \bar{C}_{H_\mu} + \lambda & \bar{C}_{H_\alpha} & C_W + C_{H_{\dot{\alpha}(\Delta\theta)}}\cdot\lambda \\ \bar{C}_{T_\mu} & \bar{C}_{T_\alpha} + \mu_0\lambda & \mu_0\lambda \\ \bar{C}_{m_\mu} & \bar{C}_{m_\alpha} & \bar{C}_{m_{\dot{\alpha}(\Delta\theta)}}\cdot\lambda - k_Y\lambda^2 \end{vmatrix} = 0 \qquad (26)$$

Expanding this stability determinant; the characteristic equation in λ is of the form:

$$A\lambda^4 + B\lambda^3 + C\lambda^2 + D\lambda + E = 0 \qquad (27)$$

where:

$$A = h_Y \mu_0 \tag{28a}$$

$$B = h_Y(\mu_0 \bar{C}_{H\mu} + \bar{C}_{T\alpha}) - \mu_0 \bar{C}_{m_{\dot{\alpha}}(\Delta\theta)} \tag{28b}$$

$$C = -\bar{C}_{T\alpha} \bar{C}_{m_{\dot{\alpha}}(\Delta\theta)} - \mu_0 \bar{C}_{H\mu} \bar{C}_{m_{\dot{\alpha}}(\Delta\theta)} + h_Y \bar{C}_{T\alpha} \bar{C}_{H\mu} + \mu_0 \bar{C}_{m\mu} C_{H_{\dot{\alpha}}(\Delta\theta)} - \mu_0 \bar{C}_{m\alpha} - h_Y \bar{C}_{T\mu} \bar{C}_{H\alpha} \tag{28c}$$

$$D = -\bar{C}_{T\alpha} \bar{C}_{H\mu} \bar{C}_{m_{\dot{\alpha}}(\Delta\theta)} + \mu_0 \bar{C}_{H\alpha} \bar{C}_{m\mu} - \bar{C}_{T\mu} \bar{C}_{m\alpha} C_{H_{\dot{\alpha}}(\Delta\theta)} + \mu_0 C_W \bar{C}_{m\mu} + \bar{C}_{T\alpha} \bar{C}_{m\mu} C_{H_{\dot{\alpha}}(\Delta\theta)} - \mu_0 \bar{C}_{H\mu} \bar{C}_{m\alpha} + \bar{C}_{T\mu} \bar{C}_{H\alpha} \bar{C}_{m_{\dot{\alpha}}(\Delta\theta)} \tag{28d}$$

$$E = C_W(\bar{C}_{m\mu} \bar{C}_{T\alpha} - \bar{C}_{T\mu} \bar{C}_{m\alpha}) \tag{28e}$$

It is convenient at this point to consider the hovering Flying Platform as a special case of the former development.

The common assumption, in hover analysis, is the exclusion of the vertical degree of freedom since, in hovering, the horizontal motion and tilting do not affect the thrust. The derivatives C_{T_μ} and C_{T_α} are are zero. Hence, the thrust will be essentially constant and there will

be no appreciable vertical motion of the machine. Principal interest is centered on changes of velocity ratio and attitude angle and not on altitude change. This can be accomplished mathematically by altering the original equations of motion so that the thrust force equation is eliminated entirely. The derivatives C_{T_μ} and C_{T_α} are zero and the alpha terms in the H-Force and moment equations are dropped.

The algebraic equations are:

$$\begin{aligned} (\bar{C}_{H_\mu} + \lambda)\Delta\mu_1 \quad &+ (C_W + C_{H_{\alpha(\Delta\theta)}} \cdot \lambda)\Delta\theta_1 = 0 \\ (\bar{C}_{m_\mu})\Delta\mu_1 \quad &+ (\bar{C}_{m_{\alpha(\Delta\theta)}} \cdot \lambda - h_Y \lambda^2)\Delta\theta_1 = 0 \end{aligned} \tag{29}$$

and the determinant of coefficients is:

$$\begin{vmatrix} (\bar{C}_{H_\mu} + \lambda) & (C_W + C_{H_{\alpha(\Delta\theta)}} \cdot \lambda) \\ (\bar{C}_{m_\mu}) & (\bar{C}_{m_{\alpha(\Delta\theta)}} \cdot \lambda - h_Y \cdot \lambda^2) \end{vmatrix} = 0 \tag{30}$$

Expanding this determinant yields the third order characteristic equation:

$$A_H \lambda^3 + B_H \lambda^2 + C_H \lambda + D_H = 0 \tag{31}$$

where:

$$A_H = h_Y \tag{32a}$$

$$B_H = h_I \bar{C}_{H_\mu} - \bar{C}_{m_{\alpha(\Delta\theta)}} \tag{32b}$$

$$C_H = \bar{C}_{m_\mu} C_{H_{\alpha(\Delta\theta)}} - \bar{C}_{H_\mu} \bar{C}_{m_{\alpha(\Delta\theta)}} \tag{32c}$$

$$D_H = \bar{C}_{m_\mu} C_W \tag{32d}$$

The characteristic equations obtained for forward flight and hovering are often referred to as the stability quartic and cubic. The roots of these equations are the values of λ that determine the final solution.

Then, for example, the response of an aircraft in pitch $\Delta\theta$ to a disturbance may be found by a solution of the following form:

$$\Delta\theta = \Delta\theta_1 e^{\lambda_1 t/\tau} + \Delta\theta_2 e^{\lambda_2 t/\tau} + \Delta\theta_3 e^{\lambda_3 t/\tau} + \Delta\theta_4 e^{\lambda_4 t/\tau} \tag{33}$$

Determination of time histories of the variables by actual solutions of this form is quite lengthy and tedious if numerous derivative variations are made.

However, analog computers can be used to solve the equations of motion in order to obtain the time histories associated with arbitrary changes in the stability derivatives. Typical time histories are shown in Figs. 5 and 6.

Investigation of the Roots of the Characteristic Equation

Frequently, the important aspect in the study of a dynamic system is the determination of the characteristic modes of motion of the aircraft, after a disturbance from steady flight, by an investigation of the four roots of the stability quartic.

Methods of predicting the character of the motion from the roots or the coefficients are covered in various texts. (Ref. 5).

It is of interest to know whether the motion is oscillatory or aperiodic. If oscillatory, it is necessary to determine the period and damping. When aperiodic, it is important to determine the rate of divergence or convergence.

This information may be obtained by examining the roots of the stability quartic.

When the roots are positive real numbers, the motion is an aperiodic divergence; negative real numbers, aperiodic convergence; and complex pairs, an oscillatory motion. In the case of a complex pair of roots, the oscillation is undamped if the real part is positive, and damped if the real part is negative.

The roots of the quartic may be obtained by any of the numerous methods outlined in many texts.

In general, if the roots are both real and complex as:

$$\begin{aligned} \lambda_1, \lambda_2 &= a \pm ib \\ \lambda_3 &= c \\ \lambda_4 &= d \end{aligned} \tag{34}$$

the period of the oscillatory pair may be found by:

$$P = \frac{2\pi T}{b} \quad [\text{seconds}] \tag{35}$$

and the damping may be found as the time (T) required for the transient response to grow to double amplitude or to decay or damp to half amplitude:

$$T = \frac{\log_e 2}{a} \tau = \frac{0.693}{a} \tau \quad [\text{seconds}] \tag{36}$$

Taking the center of gravity at the original location, (.42c above the top of the duct) the roots of the quartic for the different ducts at different speeds are computed. The damping and period are shown for each of the roots. See Tables I and II.

Investigation of the Coefficients of the Characteristic Equation

Considerable information concerning the character of the motion of the aircraft can be obtained from the coefficients of the stability quartic without solving for the roots.

If all the coefficients of:

$$A\lambda^4 + B\lambda^3 + C\lambda^2 + D\lambda + E = 0 \tag{37}$$

are positive, there can be no positive real root and there is no possibility of a pure divergence. If one of the coefficients changes sign (becomes negative) there can be either an increasing oscillation or a pure divergence in one of the modes.

The C coefficient is of special importance since it represents approximately the maneuver margin of the aircraft (Ref. 6). If the C coefficient changes sign (becomes negative) it is an indication of a serious instability. There will probably be a rapid divergence or unstable oscillation.

The E coefficient, where:

$$E = C_W \left[\frac{\partial \bar{C}_m}{\partial \mu} \frac{\partial \bar{C}_T}{\partial \alpha} - \frac{\partial \bar{C}_m}{\partial \alpha} \frac{\partial \bar{C}_T}{\partial \mu} \right] \tag{38}$$

is of importance for static stability. The static stability is positive if E is greater than zero. If E is equal to zero, one of the roots is zero and one of the modes can continue unchanged indefinitely. Usually E is the first coefficient to change sign, and therefore the first indicator of a divergence or positive real root. In some instances, it is possible for C to change sign before E, in which case there will be a dynamic instability occurring with a positive static stability.

Regardless of the signs of the coefficients, it is possible to determine the number of roots having positive real parts by using Routh's criterion. This method requires only simple calculations utilizing the coefficients of the stability quartic in setting up the familiar Routh's array. The number of roots having positive real parts is equal to the number of sign changes occurring in the first column of the array.

Also, from Routh's array, it is possible to obtain the combination of coefficients known as Routh's discriminant:

$$R = BCD - AD^2 - B^2E \tag{39}$$

where A, B, C, D and E are the coefficients of the quartic. If all the coefficients are positive, it is possible to make the following statements concerning the stability of the system.

If Routh's discriminant is positive, there is no possibility of the real part of any complex pair being positive. There will be no undamped oscillations.

If Routh's discriminant is negative, there is a complex pair of roots with a positive real part. There is an undamped oscillation.

If Routh's discriminant is equal to zero, there is a neutrally damped oscillation implying a complex pair of roots with a zero real part.

The criterion, (R = 0), then indicates a boundary between stable and unstable oscillations.

This condition, (R = 0), developed from the coefficients of the stability quartic, may be investigated further by assuming a solution of the form for neutral oscillations ($\lambda = i\omega$). Substituting this solution with the zero real part into the characteristic equation gives:

$$A\lambda^4 + B\lambda^3 + C\lambda^2 + D\lambda + E = 0$$

$$Ai^4\omega^4 + Bi^3\omega^3 + Ci^2\omega^2 + Di\omega + E = 0 \qquad (40)$$

$$A\omega^4 - B\omega^3 i - C\omega^2 + D\omega i + E = 0$$

Forming two equations of the real and imaginary parts:

$$A\omega^4 - C\omega^2 + E = 0 \qquad (41)$$

$$-B\omega^3 + D\omega = 0 \qquad (42)$$

and solving Eq. 41 and Eq. 42 for ω^2, yields:

$$\omega^2 = \frac{D}{B} \qquad (43)$$

$$\omega^2 = \frac{C}{2A} \pm \sqrt{\frac{C^2}{4A^2} - \frac{E}{A}} \qquad (44)$$

Substituting Eq. 43 in Eq. 41 results in:

$$\frac{AD^2}{B^2} - \frac{CD}{B} + E = 0 \tag{45}$$

or:

$$BCD - AD^2 - B^2E = 0 = R \tag{46}$$

which is the form of Routh's discriminant.

With this analysis, one can obtain an appreciation of the requirements imposed on the coefficients A, B, C, D, E, so that the solution R = 0 is a stability boundary between stable and unstable oscillations.

Since a solution of the form for neutral oscillations is assumed, ($\lambda = i\omega$), inspection of Eq. 43 reveals that ω will be a real number, e.g., $\omega = a$, if D and B are both positive, and the solution $\lambda = ia$ will indicate a neutral oscillation. However, if D or B changes sign so that $\omega = ia$ in Eq. 43, then the solution will be $\lambda = -a$, or a real root. Therefore, when the D coefficient changes sign, (becomes negative), the solution of Routh's discriminant equal to zero no longer defines an oscillation boundary.

Boundaries of the Stability Quartic

In the analog computer program, it was found that the derivatives $\bar{C}_{m_\mu}$ and $\bar{C}_{m_\alpha}$ had a principal effect on the mode of motion of the Flying Platform.

The Figs. 10A, 11A, 13A and 14A entitled "Boundaries of the Stability Quartic" are drawn with $\bar{C}_{m_\mu}$ and $\bar{C}_{m_\alpha}$ as the ordinate and abscissa.

Included on this diagram are various boundaries of the stability quartic plotted as functions of $\bar{C}_{m_\mu}$ and $\bar{C}_{m_\alpha}$. Values of the total stability derivatives were used as calculated from the wind tunnel data for each speed and duct configuration. The theoretical value of pitch damping was used and kept constant for these diagrams.

The coefficients of the stability quartic, C, D and E are plotted as functions of $\bar{C}_{m_\mu}$ and $\bar{C}_{m_\alpha}$ and appear as the straight lines labeled C = 0, D = 0 and E = 0. The lines so labeled represent the boundaries at which each coefficient changes sign from positive to negative for the appropriate values of $\bar{C}_{m_\mu}$ and $\bar{C}_{m_\alpha}$.

The coefficients are negative on the hatched side of the line. For example, near the origin in the right half plane the vertical line labeled C = 0 is negative on the right side of the line.

The meaning of the traversing of these lines (coefficients changing sign from positive to negative) has been discussed previously and, for this section, can be summarized as:

C < 0 - Serious instability associated with negative maneuver margin.

D < 0 - The solution R = 0 no longer has meaning as an oscillation boundary.

E < 0 - Instability associated with a negative static margin. Aircraft statically unstable. Dynamic instability present in the form of a divergence due to static instability.

The coefficients A and B, not functions of $\bar{C}_{m_\mu}$ and $\bar{C}_{m_\alpha}$ and generally positive, do not appear on these diagrams.

The line R = 0, representing Routh's discriminant, is plotted to denote the boundary between stable and unstable oscillations.

This line represents the loci of the values of $\bar{C}_{m_\mu}$ and $\bar{C}_{m_\alpha}$ for neutral oscillatory motion.

On the left side of the line R is positive and the oscillations will be stable. On the right or hatched side R is negative and the oscillations will be unstable. The line R = 0 does not exist past the line D = 0, since its meaning as an oscillation boundary is ended whenever the D coefficient becomes negative.

In one case, (Fig. 13 A), the line R = 0 has essentially three branches, all representing a neutral oscillation boundary, and all located in the region where the D coefficient is positive. In the top half plane, the two branches of R = 0 form a parabola inside of which there is an unstable oscillation (at least two of the roots must form a complex pair with a positive real part). In the bottom half plane, only one branch of the parabola appears since the other is nonexistent when it crosses the D = 0 line into the region where the D coefficient is negative. Note that the line E = 0 passes through the middle of the R = 0 parabola in the top half plane.

Whenever the values of $\bar{C}_{m_\mu}$ and $\bar{C}_{m_\alpha}$ locate a point on the negative side of the E = 0 line, at least one of the roots of the quartic must be positive and real, and an instability exists which takes the form of a divergence.

Then, in the region between the E = 0 line and the right hand branch of the R = 0 line in the first quadrant (Fig. 13A), at least three of the roots of the quartic are accounted for; a complex pair with a positive real part and a positive real root. The other root in this region is a convergence as seen in the root locus plot Fig. 13-I.

The other two branches of the R = 0 line located in the second and third quadrants represent oscillation boundaries, so that in the region between them, R is greater than zero and the entire area represents a

completely stable region of only convergences and stable oscillations.

In Fig. 14A, the R = 0 line is terminated when it reaches the E = 0 line since it passes into a region where $\bar{C}_{m_\mu}$ and E are always negative, so that the predominating mode of motion is a divergence that strongly masks all other modes of motion.

The line labeled RLBP represents a locus of points obtained from root locus diagrams. The letters RLBP are an abbreviation for "Root Locus Break Points". The break point in this case represents the point in the right half plane of the root locus diagram where a complex pair of roots joins the positive real axis, thereby terminating the unstable oscillation and becoming two aperiodic divergences.

In other words, moving to the right from the stable region, across the R = 0 line, and passing into a region of unstable oscillations, at least two of the roots of the quartic are a complex pair with positive real parts (Figs. 10A, 11A, and 14A). Continuing to move to the right into the first quadrant and crossing the RLBP line, this complex pair becomes two real positive roots, ending the unstable oscillation and now representing two divergent roots. To the immediate right or hatched side of the RLBP line, at least two of the roots of the quartic are positive real roots.

The line RLBP does not appear in Fig. 13A, because the parabola R = 0 already defines a large region where unstable oscillations start and stop.

However, for extremely large values of $\bar{C}_{m_\mu}$ and $\bar{C}_{m_\alpha}$ beyond the values of this diagram (Fig. 13A), there is a region where the complex roots become positive real roots for a time. (See root locus Fig. 13--I-e, points 180 and 181.) The value of $\bar{C}_{m_\alpha}$ is equal to 0.006 and $\bar{C}_{m_\mu}$ is approximately equal to 0.1 at these points, which are beyond the pertinent range of $\bar{C}_{m_\mu}$ and $\bar{C}_{m_\alpha}$ for this particular case.

The various center of gravity locations have been plotted on these diagrams according to their respective values of $\bar{C}_{m_\mu}$ and $\bar{C}_{m_\alpha}$ as listed in Table III . The broken line between these points represents the approximate line of travel for the c.g. at intermediate values.

Explanation of Stability Diagrams

The Figs. 10B, 11B, 13B and 14B entitled "Stability Diagrams" are a greatly simplified form of the previous boundary diagrams. The only portions of the boundaries that have been retained are those which divide the diagram into the pertinent regions of stability.

The unshaded area represents a region of complete dynamic stability . Only roots representing convergences and stable oscillations exist in this region.

The shaded areas represent regions of dynamic instability. Roots existing in this region represent divergences and/or unstable oscillations.

There are always four roots to contend with in every region. In the stable region all four roots must be stable roots. In the unstable region, a minimum of one unstable root must always exist while the others may be stable.

Actually, the unstable roots are the predominant modes of motion in the unstable regions and mask the stable modes present.

One shaded unstable region is labeled "unstable oscillations" and indicates that at least two of the four roots in this region must be a complex pair with a positive real part. The other shaded area indicates the unstable region where a minimum of one unstable root must exist.

Some of the interesting modes of motions which prevail in the various regions are labeled in these diagrams.

Again, the various center of gravity locations have been plotted according to their respective values of $\bar{C}_{m_\mu}$ and $\bar{C}_{m_\alpha}$ as listed in Table III. The broken line represents the approximate line of travel of the center of gravity at intermediate values.

For the case of hovering, μ_o and $\bar{C}_{m_\alpha}$ equal zero. The diagram is plotted only for $\bar{C}_{m_\mu}$ and appears in the form shown in Fig. 8.

The study of these diagrams, together with the associated root locus diagrams, will present quite clearly and concisely the precise modes of motion to be expected at different speeds for different center of gravity locations with the different duct configurations.

Explanation of the Root Locus Diagrams

The stability diagrams were prepared in order to show concisely and clearly the role of C_{m_μ}, C_{m_α}, vertical center of gravity travel, speed changes, and different duct designs, in affecting the modes of motion of the Flying Platform.

The diagrams exhibit rather precisely the mode of motion associated with locations in the various regions.

Although the determination of the stability boundaries is quite lengthy, they may be calculated by various methods.

In the formulation of the stability diagrams for this Report, use was made of the root locus method of displaying dynamic responses.

With this method, it is possible to exhibit the properties of a linear system by plotting the loci of the roots of the characteristic equation in which the values of selected derivatives have been varied.

A complete treatment on the utilization of this method is available in texts by Evans (Ref. 7) or Savant (Ref. 8).

Since primary interest is centered on varying the derivatives $\bar{C}_{m_\mu}$ and $\bar{C}_{m_\alpha}$, the characteristic equation may be written in the form:

$$A\lambda^4 + B\lambda^3 + (C_1 + C_2\bar{C}_{m_\alpha} + C_3\bar{C}_{m_\mu})\lambda^2$$
$$+ (D_1 + D_2\bar{C}_{m_\alpha} + D_3\bar{C}_{m_\mu})\lambda + (E_1\bar{C}_{m_\alpha} + E_2\bar{C}_{m_\mu}) = 0 \qquad (47)$$

where the quantities enclosed in the parenthesis are equal to the coefficients C, D and E. From this expression it is possible to calculate the poles and the zeros. Since vertical center of gravity travel seems to have the primary effect of changing $\bar{C}_{m_\mu}$, the root locus diagrams were plotted so that $\bar{C}_{m_\mu}$ varied from zero to positive or negative infinity. The poles were calculated for specific values of $\bar{C}_{m_\alpha}$ with $\bar{C}_{m_\mu}$ equal to zero.

Solving the characteristic equation in this manner gives the four roots of the quartic p_1, p_2, p_3, p_4. The zeros of the equation are the increments of $\bar{C}_{m_\mu}$, namely:

$$C_3 = \mu_0 C_{N_{\alpha(\Delta\theta)}}$$
$$D_3 = \mu_0(C_W + \bar{C}_{H_\alpha}) + \bar{C}_{T_\alpha} C_{N_{\alpha(\Delta\theta)}}$$
$$E_2 = C_W \bar{C}_{T_\alpha} \qquad (48)$$

Solving the above, the zeros for $\bar{C}_{m_\mu}$ are obtained and denoted by z. Similarly, the zeros for $\bar{C}_{m_\alpha}$ denoted by Z, may be obtained from:

$$C_2 = -\mu_0$$
$$D_2 = -\bar{C}_{T_\mu} C_{N_{\alpha(\Delta\theta)}} - \mu_0 \bar{C}_{H_\mu} \qquad (49)$$
$$E_1 = -C_W \bar{C}_{T_\mu}$$

Using the former expressions, the root locus equation may be written for a specific value of $\bar{C}_{m_\alpha}$ with $\bar{C}_{m_\mu}$ varying from zero to positive or negative infinity as:

$$\mu_0 h_Y (\lambda - p_1)(\lambda - p_2)(\lambda - p_3)(\lambda - p_4) + \bar{C}_{m_\mu}(\mu_0)(C_W + \bar{C}_{H_\alpha})(\lambda - z_1) = 0 \quad (50)$$

where the p's represent the poles and the z's the zeros of $\bar{C}_{m_\mu}$.

For the case where the poles (P) are calculated for $\bar{C}_{m_\mu} = \bar{C}_{m_\alpha} = 0$, and the zeros (Z) for $\bar{C}_{m_\alpha}$ are utilized, the expression takes the form:

$$\mu_0 h_Y (\lambda)(\lambda - P_1)(\lambda - P_2)(\lambda - P_3) - \bar{C}_{m_\alpha}(\mu_0)(\lambda - Z_1)(\lambda - Z_2) = 0 \quad (51)$$

in which $\bar{C}_{m_\alpha}$ varies from positive to negative infinity while $\bar{C}_{m_\mu}$ equals zero.

A group of root locus diagrams are plotted so that essentially all values of $\bar{C}_{m_\mu}$ and $\bar{C}_{m_\alpha}$ are covered for a particular duct at a selected speed.

Associated with each stability diagram there are five root locus sets. The first set investigates the modes of motion encountered when moving along the ordinate or abscissa of the stability diagram. The other four sets, labeled I, II, III and IV, investigate the modes of motion present in the four quadrants of the stability diagram. The value of $\bar{C}_{m_\mu}$ (Eq. 50) in these diagrams varies from zero to positive or negative infinity.

The root locus sets are plotted for both ducts at μ equal to 0.05 and 0.10.

Included in each figure used to investigate the modes of motion in each quadrant (I, II, III, IV), one root locus is plotted with the zeros of $\bar{C}_{m_\alpha}$ instead of $\bar{C}_{m_\mu}$. This plot is divided from the rest by a double line border as in Fig. 10-I-f. In each of these particular double border diagrams, $\bar{C}_{m_\mu}$ is equal to zero and $\bar{C}_{m_\alpha}$ varies from zero to infinity. This then shows the movement of the initial positions of the poles for each quadrant as the value of $\bar{C}_{m_\alpha}$ is increased from zero to infinity. In this way it is possible to sketch the root loci for all higher values of $\bar{C}_{m_\alpha}$ beyond those calculated for each quadrant. In this respect, the values of $\bar{C}_{m_\alpha}$ in each quadrant are usually large enough so that the basic appearance of the root loci will not change for values beyond the highest shown in each set.

All root loci drawn in this report were accurately calculated and plotted to the scale shown in each figure.

The root locus set for $\mu = 0$ is also plotted in Fig. 7. For both ducts in the hovering case $\bar{C}_{m_\alpha}$ equals zero. The stability cubics are written as:

$$A_H \lambda^3 + B_H \lambda^2 + C_H \lambda + D_H = 0 \tag{31}$$

or:

$$A_H \lambda^3 + B_H \lambda^2 + (C_{H_1} + C_{H_2} \bar{C}_{m_\mu})\lambda + D_{H_1} \bar{C}_{m_\mu} = 0 \tag{52}$$

The root locus equation, after dropping a negligible "zero" due to the small value of $C_{H_{d\ (\Delta\theta)}}$, is:

$$(h_Y)(\lambda)(\lambda - p_1)(\lambda - p_2) + \bar{C}_{m_\mu}(C_W) = 0 \tag{53}$$

where C_W is known and $\bar{C}_{m_\mu}$ is varied from zero to positive or negative infinity. The poles are calculated for $\bar{C}_{m_\mu}$ equal to zero. The diagrams for the hovering case have three poles and no zeros.

The root locus method may also be utilized conveniently for the investigation of the effects of artificial stabilization on the transient response of the Flying Platform. Artificial stabilization may be provided by a rate sensitive device such as the gyro-bar with aerodynamic or mechanical damping.

The addition of this type of device to the dynamic system may be accomplished mathematically by including a rate sensitive transfer function with a phase lag of the type $\frac{Kd}{1 + T\,d}$ — to the pitch damping term in the moment equation.

For hovering, the determinant of coefficients in algebraic form becomes:

$$\begin{vmatrix} (\bar{C}_{H_\mu} + \lambda) & (C_W) \\ (\bar{C}_{m_\mu}) & \left(\bar{C}_{m_{\alpha(\Delta\theta)}} \cdot \lambda - h_Y \lambda^2 - \frac{K\lambda}{1+T\lambda}\right) \end{vmatrix} = 0 \qquad (54)$$

Expanding this determinant:

$$0 = h_Y \lambda^3 + \left(h_Y \bar{C}_{H_\mu} - \bar{C}_{m_{\alpha(\Delta\theta)}}\right)\lambda^2 - \bar{C}_{H_\mu} \bar{C}_{m_{\alpha(\Delta\theta)}} \cdot \lambda + C_W \bar{C}_{m_\mu} + \frac{K\lambda}{1+T\lambda}\left(\lambda + \bar{C}_{H_\mu}\right) \qquad (55)$$

and arranging the poles and zeros as:

$$0 = [1+T\lambda]\left[h_Y \lambda^3 + \left(h_Y \bar{C}_{H_\mu} - \bar{C}_{m_{\alpha(\Delta\theta)}}\right)\lambda^2 - \bar{C}_{H_\mu} \bar{C}_{m_{\alpha(\Delta\theta)}} \lambda + C_W \bar{C}_{m_\mu}\right] + K\lambda\left(\lambda + \bar{C}_{H_\mu}\right) \qquad (56)$$

where T is the time constant for the phase lag , the root locus equation for the hovering case may be written as:

$$h_Y(\lambda-\rho_1)(\lambda-\rho_2)(\lambda-\rho_3)(\lambda-\rho_4)+K(\lambda)(\lambda+\bar{C}_{H_\mu})=0 \tag{57}$$

where the gain of the feedback loop, K, of the stabilizing device varies from zero to infinity.

The determinant of coefficients for the addition of artificial stabilization in forward flight is:

$$\begin{vmatrix} \bar{C}_{H_\mu}+\lambda & \bar{C}_{H_\alpha} & C_W+C_{H_{\dot\alpha(\Delta\theta)}}\cdot\lambda \\ \bar{C}_{T_\mu} & \bar{C}_{T_\alpha}+\mu_0\lambda & -\mu_0\lambda \\ \bar{C}_{m_\mu} & \bar{C}_{m_\alpha} & \bar{C}_{m_{\dot\alpha(\Delta\theta)}}\cdot\lambda-h_Y\lambda^2-\dfrac{K\lambda}{1+T\lambda} \end{vmatrix}=0 \tag{58}$$

and expanding the determinant:

$$0=A\lambda^4+B\lambda^3+C\lambda^2+D\lambda+E+\frac{K\lambda}{1+T\lambda}\left[\mu_0\lambda^2+(\mu_0\bar{C}_{H_\alpha}+\bar{C}_{T_\alpha})\lambda+(\bar{C}_{H_\mu}\bar{C}_{T_\alpha}-\bar{C}_{H_\alpha}\bar{C}_{T_\mu})\right] \tag{59}$$

where the first five terms represent the original characteristic equation and T is again the time constant for the phase lag. Separating the poles and zeros in root locus form gives:

$$\mu_0 h_Y(\lambda-\rho_1)(\lambda-\rho_2)(\lambda-\rho_3)(\lambda-\rho_4)(\lambda-\rho_5)+K(\lambda)(\lambda-z_1)(\lambda-z_2)=0 \tag{60}$$

where K, the gain, varies from zero to infinity.

The root locus diagrams for the artificially stabilized machine in hovering and high forward speed are plotted in Figs. 9, 12 and 15.

These diagrams, together with all other pertinent root locus diagrams, are fully explained in the DISCUSSION.

Effect of Vertical Center of Gravity Movement on the Overall Stability Derivatives

The overall stability derivatives are expressed by Eq. 21 as:

$$\bar{C}_{m_\alpha} = C_{m_\alpha} + \frac{x_T}{R} C_{T_\alpha} - \frac{z_H}{R} C_{H_\alpha} \tag{21f}$$

$$\bar{C}_{m_\mu} = C_{m_\mu} + \frac{x_T}{R} C_{T_\mu} - \frac{z_H}{R} C_{H_\mu} + \frac{z_D}{R} \mu_o C_D' \tag{21e}$$

The distances x_T, z_H and z_D represent the moment arms from the total center of gravity to the respective forces. C_{m_μ} and C_{m_α} represent the stability derivatives about the quarter chord, whereas, $\bar{C}_{m_\mu}$ and $\bar{C}_{m_\alpha}$ are functions of the distances x_T, z_H and z_D. When the total center of gravity of the aircraft is moved vertically these distances will vary so that considerable changes in the overall value of the derivatives, especially $\bar{C}_{m_\mu}$, can be obtained.

In the original c.g. location, the total center of gravity is 0.42 of the chord length (0.42c) above the top edge of the duct. For the case of the long chord duct, the total center of gravity of the aircraft is located approximately nine inches above the top edge of the duct. Similarly, the center of gravity of the short chord duct is also assumed to be at the 0.42c location so that it is approximately five inches above the top of the duct. These positions are designated as the original center of gravity positions from which the vertical variations of c.g. are measured. The pilot's

stand-on platform always remains at this original position, i.e., 0.42c above the top of the long and short chord duct.

The actual scale profiles of the long and short chord duct models are shown in Fig. 2.

The values of the stability derivatives $\bar{C}_{m_\mu}$ and $\bar{C}_{m_\alpha}$ for the different center of gravity locations shown in Fig. 16 are presented in Table III.

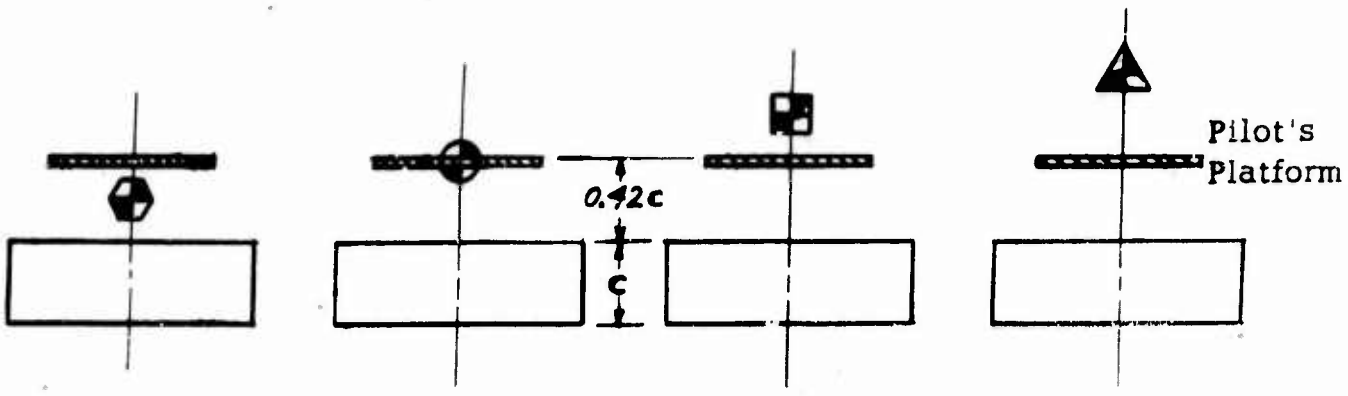

c.g. 0.5 ft. down from original	original location of c.g.	c.g. 0.5 ft. up from original location	c.g. 1.0 ft. up from original location

Fig. 16 CENTER OF GRAVITY LOCATIONS

DISCUSSION

General

1. Similarity of Stability Derivatives

From the information contained in Table III, concerning the overall value of the stability derivatives, it is apparent that there is some similarity or overlapping of values for the two ducts for different speeds at different c.g. locations. For example, the values of $\bar{C}_{m_\mu}$ for the long chord duct at μ equal to 0.05 with the c.g. raised 0.5 feet is equal to 0.0136 while $\bar{C}_{m_\mu}$ for the short chord duct at μ equal to 0.05 with the c.g. at the original location is approximately the same or equal to 0.0121. A small adjustment in c.g. location of one duct configuration would make the derivative equal that of the other configuration. Similarly, the value of $\bar{C}_{m_\alpha}$ equal to 0.0032 also matches up for both ducts when μ equals 0.10 at the highest c.g. location.

Therefore, at a specific speed in a certain speed range, similar values of either stability derivative may be obtained for both duct configurations by adjusting the vertical center of gravity location.

2. Attitude Angle for Steady Forward Flight

As seen in Fig. 18, the attitude angle for steady-state equilibrium in forward flight is plotted versus μ. For convenience, Fig. 17 is plotted directly above Fig. 18 so that conversions may be easily accomplished between μ and V in feet per second or miles per hour.

From Fig. 18, it is evident that the long chord duct requires larger tilt angles than the short chord duct. This can be explained by the fact that the parasite and momentum drag of the long chord vehicle is probably greater than that of the short chord duct.

For a long chord duct, the flow tends to align itself more axially than for a shorter length duct, and therefore, the momentum drag is greater.

In order to overcome the larger total drag, the thrust vector of the vehicle must be tilted sufficiently so that the component of thrust in the

horizontal direction exactly cancels the total drag in steady-state flight. Although the short chord duct yields the more desirable smaller tilt angles, other characteristics such as the performance of the long chord duct would also be considered in any design (Ref. 2).

Static Stability

1. The E Coefficient

As mentioned previously in the DEVELOPMENT, the fundamental mathematical condition for static stability is that the E coefficient (the term independent of λ in the stability quartic) be positive.

The E coefficient:

$$E = C_W \left(\bar{C}_{m_\mu} \bar{C}_{T_\alpha} - \bar{C}_{T_\mu} \bar{C}_{m_\alpha} \right) \tag{38}$$

is a function of the two static stability partial derivatives $\bar{C}_{m_\mu}$ and $\bar{C}_{m_\alpha}$.

The term $\bar{C}_{m_\mu}$ is referred to as the static velocity stability and $\bar{C}_{m_\alpha}$ the static angle of attack stability.

An aircraft is statically stable with velocity, if, when acted upon by a pure velocity disturbance, it creates a moment about the center of gravity tending to restore the aircraft to the initial velocity. Similarly, an aircraft is statically stable with angle of attack, if, when acted upon by a pure angle of attack disturbance, it creates a moment about the center of gravity tending to restore the aircraft to the initial angle of attack. The criterion for static velocity stability requires that $\bar{C}_{m_\mu}$ be greater than zero while static angle of attack stability requires that $\bar{C}_{m_\alpha}$ be less than zero.

Generally, the Flying Platform has too much velocity stability in hovering and forward flight. However, the velocity stability does decrease as flight speed increases and, depending on c.g. location, may even become unstable by changing sign.

With respect to the angle of attack stability, in hovering $\bar{C}_{m_\alpha}$ is equal to zero and the Flying Platform is neutrally stable with angle of attack. In forward flight, $\bar{C}_{m_\alpha}$ has the wrong sign, that is, $\bar{C}_{m_\alpha}$ increases positively as flight speed increases so that the platform is statically unstable with angle of attack. Neither of these criteria, taken by itself, is adequate to predict the static stability of the Flying Platform. The commonly used static stability criterion of $C_{m_\alpha} < 0$ for airplanes, is not sufficient for this case since it assumes C_{m_μ} is equal to zero.

For an aircraft operating in a flight regime or configuration where C_{m_μ} is not equal to zero, the general criterion for static stability must include the effects of both C_{m_μ} and C_{m_α} as exemplified by the E coefficient. Static instability results in a dynamic divergence whenever this coefficient becomes negative. In the speed regime considered for this Flying Platform, all the terms in the E coefficient are always positive except $\bar{C}_{m_\mu}$ and $\bar{C}_{T_\mu}$.

For the long chord duct, the term $\bar{C}_{m_\mu}$ is generally positive and large, but can be reduced and even made negative in certain forward flight speeds by raising the center of gravity. The term $\bar{C}_{T_\mu}$ becomes negative rather quickly and since $\bar{C}_{m_\alpha}$ is always positive the quantity $-\bar{C}_{T_\mu}\bar{C}_{m_\alpha}$ is usually a positive increment to the E coefficient. From this it is evident that the E coefficient of the long chord duct, in the region of speeds considered, will probably not change sign unless the center of gravity is raised sufficiently so that $\bar{C}_{m_\mu}$ can become a negative value.

Also, it is interesting to note for this case that the larger the positive (unstable) value of $\bar{C}_{m_\alpha}$ the larger the value of the quantity $-\bar{C}_{T_\mu}\bar{C}_{m_\alpha}$. This becomes a larger positive increment to the E coefficient and therefore enhances the static stability. However, large positive $\bar{C}_{m_\alpha}$ has a simultaneous adverse effect on the other coefficients of the stability quartic. For example, for large $\bar{C}_{m_\alpha}$, positive static stability may exist while in all probablility the C coefficient will have already changed sign, indicating a serious instability. See Table I.

For the short chord duct, the values of $\bar{C}_{m_\mu}$ are considerably smaller and become negative more quickly than the long chord duct as forward flight speed is increased. Also, $\bar{C}_{T_\mu}$ remains positive for the speeds considered. The first term in the E coefficient becomes a negative increment as soon as $\bar{C}_{m_\mu}$ becomes negative. The second term is always positive so that E changes sign as soon as the value of $\bar{C}_{m_\mu}$ has reduced to a small positive number where $\bar{C}_{T_\mu}\bar{C}_{m_\alpha} > \bar{C}_{m_\mu}\bar{C}_{T_\alpha}$. Whenever $\bar{C}_{m_\mu}$ becomes negative, E has already become negative for this case.

Although it is desirable to have a positive static stability, instabilities due to E changing sign are associated with velocity changes and are probably not as serious as the instabilities associated with angle of attack changes which are indicated by other coefficients of the stability quartic changing sign.

2. The Moment to Trim Versus Velocity Diagram

The static-trim curve, in which the moment produced by the machine in trim equilibrium is plotted versus forward speed, can also be used to investigate the static stability of the Flying Platform.

In Fig. 19, the M-V curves are plotted for both ducts for the various center of gravity locations by using the moment equation:

$$\Sigma M_{Y_{c.g.}} = M_{c/4} + T \cdot x_T - H \cdot z_H + D \cdot z_D = 0 \qquad (4c)$$

where $T \cdot x_T$ is the control input of the pilot, and the moment produced by the vehicle including the drag of the pilot is:

$$M = M_{c/4} - H \cdot z_H + D \cdot z_D \tag{61}$$

Inspection of the curves of this moment plotted versus velocity indicates that the value of the moment required to trim can be reduced by raising the center of gravity position.

The static stability, or slope of the M-V trim curve, is the total derivative $\frac{dM}{dV}$. In all cases presented, the slope starts as positive, reaches a zero value, and then becomes negative. The criterion for static stability is $\frac{dM}{dV} > 0$.

Also plotted on the M-V diagram is the horizontal line drawn at 200 foot-pounds representing the approximate maximum control moment attainable by the pilot for trim. Presuming that a typical 200-pound pilot, with his c.g. located at $3\frac{1}{3}$ feet, can lean forward 20 degrees relative to the platform, the maximum control moment he can apply would be approximately:

$$M_{P_{MAX.}} = (200)(3.33)(\sin 20^\circ)$$

$$M_{P_{MAX.}} \approx 200 \text{ ft.-lbs.} \tag{62}$$

By convention, the distance x_T is taken as minus when the c.g. is moved forward in forward flight. The scale for x_T plotted opposite M_{μ} then, in effect, represents control position for trim.

In forward flight, the maximum forward displacement x_T is equal to approximately -0.36 feet for 200 foot-pounds. The intersections of the curves and the horizontal line, (denoted by circles), represent the

maximum forward speed for which the pilot is able to trim the moment produced by the Platform.

The short vertical dashes on each curve represent the points where $\frac{dM}{dV}$ equals zero and beyond which $\frac{dM}{dV}$ becomes negative. These points are exactly the speeds at which the E coefficient changes sign and becomes negative. Actually the speeds beyond the vertical dash location $\left(\frac{dM}{dV} = 0\right)$, represent flight in a speed regime where the Platform is statically unstable.

For a statically stable aircraft, the control position for trim always moves forward (pilot must be positioned further forward to trim the Platform) as higher trim flight speeds are achieved.

Notice on the diagram that the control position <u>for trim</u>, starts to reduce beyond these vertical dash points. In this region, the control position x_T, for trim (pilot position) is located at successively smaller negative values for greater trim speeds after having reached the maximum negative value at $\frac{dM}{dV}$ equal to zero. This should not be thought of as a region of so called "control reversal", in the normal sense of the words, even though the control moves aft to trim each successively higher flight speed. Usually the term "control reversal" implies quite a different meaning with different effects and is most frequently associated with the reversed control effectiveness due to aeroelastic phenomena., when the control derivative, $\frac{\partial C_m}{\partial \delta_c}$, changes sign (δ_c is the control deflection). With this meaning, for example, whenever a pilot attempts to pull the nose of an airplane up in order to reduce speed, (control moved aft), the aircraft actually noses down and tends to gain speed. Fortunately, this is not what occurs for the Flying Platform if it is operated in a statically unstable configuration, or, for that matter, to any airplane which happens to be operating in a statically unstable configuration. In order to go faster or

move the nose down, it is still initially necessary to move the control forward (lean forward) to obtain the desired increase in speed. What is different is that once the desired higher speed is achieved, and the vehicle is again in trim, the pilot will find the control positioned forward less than it was for the slower trim position (pilot leaning forward less than previous trim position). In order to accelerate an aircraft in a given direction, the control will always be initially moved in the same sense regardless of whether the aircraft is statically stable or unstable.

To slow down, the pilot initially leans back, but when the aircraft is again trimmed at the desired slower flight speed, in the region where $\frac{dM}{dV}$ is negative, he will find he is leaning further forward than before.

As seen by the curves in the M-V diagram, raising the c.g. does reduce the control moment required for trim but, unfortunately, also moves this point ($E = \frac{dM}{dV} = 0$) to successively lower forward speeds, thereby reducing the statically stable flight envelope.

The asterisks on the diagram indicate the maximum points where $\frac{dM}{dV}$ is equal to zero, for each duct, commensurate with the 200 foot-pound control moment. The difference between the two radically different duct designs appears to be on the order of only six feet per second:

Short Chord Duct $V_{max} \approx$ 38 feet per second

Long Chord Duct $V_{max} \approx$ 32 feet per second

Other flying qualities of a machine similar in nature to the subject vehicle are discussed in Ref. 3.

Dynamic Stability

The fundamental requirement for stable dynamic response is that all the coefficients of the stability quartic and Routh's discriminant be positive.

If all the coefficients are initially positive, the first indication of an instability will normally be a divergence when E changes sign, or an unstable oscillation when Routh's discriminant becomes negative.

The roots of the characteristic equations evaluated for the original c.g. location of each duct at μ equal to 0.05 and 0.10 are shown in Tables I and II.

It should be remembered that the following analysis investigates the control-fixed or open-loop response of the Flying Platform configurations.

The open-loop response is the resulting mode of motion of the Flying Platform when the pilot remains rigid and applies no control inputs throughout the transient response. The closed-loop response is the resulting mode of motion of the Platform when the pilot acts as a feedback by providing controlling inputs to the transient response. Although the Flying Platform is unstable in the open-loop it will be stable closed-loop if the pilot can correctly control the machine as he desires.

The open-loop response of the Flying Platform is investigated to determine the effects on the dynamic stability of vertical center of gravity location, duct design changes and artificial stabilization.

In this Report this may be thoroughly accomplished by referring to the various figures of the stability diagrams, boundaries of the quartic and the associated root locus plots.

On the figures labeled "Boundaries of the Stability Quartic" and "Stability Diagram", the symbols represent the values of $\bar{C}_{m_\mu}$ and $\bar{C}_{m_\alpha}$ for each particular center of gravity location. The dashed line connecting these circles represents the movement of these points on the diagram, as the center of gravity location is varied.

For the different cases:

1. Long and Short Chord Duct Hovering $\mu = V = 0$

The dynamic analysis of the hovering case of the subject Flying Platform can best be obtained by referring to the root locus diagram Fig. 7 a and b.

The case is somewhat simplified by the fact that we deal with a cubic equation and $\bar{C}_{m_\alpha}$ is equal to zero.

For the hovering long chord duct (Fig. 7b), when $\bar{C}_{m_\mu}$ is equal to zero, the three poles represent two convergences (point 80 and point 81) and a zero root (point 82). As the gain of $\bar{C}_{m_\mu}$ is increased positively, the pole at point 80 moves toward point 86 and continues as a convergence for all values of positive $\bar{C}_{m_\mu}$.

Also, as $\bar{C}_{m_\mu}$ is increased positively, the two poles at point 81 and point 82 move toward each other on the negative real axis until they become equal roots at the break point (point 83). Further increases in $\bar{C}_{m_\mu}$ cause the equal roots to break away from the negative real axis and become a complex pair, indicating a stable oscillation of increasing frequency and decreasing stability. At point 84, $\bar{C}_{m_\mu}$ has increased to the value at which the oscillation becomes neutrally damped. Increasing $\bar{C}_{m_\mu}$ further makes the oscillation unstable (point 85). The oscillation continues to increase in instability and frequency as $\bar{C}_{m_\mu}$ is varied to positive infinity.

The short chord duct in hovering (Fig. 7a) has a similar analysis and is numbered accordingly, the only difference being the respective gains for the particular modes of motion.

In order to complete the set of stability diagrams, Fig. 8 is presented showing the various gains of $\bar{C}_{m_\mu}$ for the different center of gravity locations together with the various modes of motion. This diagram is considerably different from the other stability diagrams since only the values of $\bar{C}_{m_\mu}$ need to be shown.

For the long chord duct, $\bar{C}_{m_\mu}$ changes approximately 0.0028 per inch of c.g. movement. Stable oscillations start when $\bar{C}_{m_\mu}$ is equal to 0.0003, which is the value of $\bar{C}_{m_\mu}$ at the root locus break point (point 83). Unstable oscillations start when $\bar{C}_{m_\mu}$ is equal to 0.0056, which is the value of $\bar{C}_{m_\mu}$ at point 84 on the root locus diagram. All the center of gravity locations are well inside the unstable region.

For the short chord duct, $\bar{C}_{m_\mu}$ changes approximately 0.001 per inch of c.g. movement. Stable oscillations start when $\bar{C}_{m_\mu}$ is equal to 0.000075, which is the value of $\bar{C}_{m_\mu}$ at the root locus break point (point 93). Unstable oscillations start when $\bar{C}_{m_\mu}$ is equal to 0.0024, the value of $\bar{C}_{m_\mu}$ at point 94 on the root locus diagram. Again, all the c.g. locations are well inside the unstable region.

For the specific case of the long chord duct in hovering, the roots of the characteristic equation (Table I) for the c.g. in the original location indicate a convergent mode and an unstable oscillation. The period of this oscillation is approximately four seconds with a time to double amplitude of about one second.

For the short chord duct in hovering, the roots of the characteristic equation (Table II) for the c.g. in the original location indicate a convergent mode and an unstable oscillation. The period of this oscillation is approximately six seconds with a time to double amplitude of 2.23 seconds.

Both ducts are rather unstable with regard to the open-loop response, however, the short chord duct is noticeably the better of the two.

As mentioned in the DEVELOPMENT, it is interesting to investigate the effects of artificial stabilization on the transient response of these vehicles.

The effect of such devices on the behavior of the system is shown by root locus plots for several different cases.

2. Long and Short Chord Duct Artificial Stabilization Added

Hovering $\mu = 0$

For the short chord duct (c.g. in the original location) when K varies from zero to positive infinity reference is made to Fig. 9a.

The artificial stabilization adds two zeros to the hovering root locus diagram, one at the origin and the other close by in the left half plane. Arbitrarily selecting T equal to 3.333, an additional pole is located at -0.3.

When K is equal to zero, the poles located at point 100 indicate an unstable, lightly damped oscillation, while the poles at point 101 and point 102 represent two convergences. As K is increased, the poles (points 101 and 102) come together on the real axis at the break point 103 and then break away from the real axis to become a stable oscillation of increasing frequency. Meanwhile the unstable oscillation becomes stable with no appreciable change in frequency (point 104). However, when K is increased further, the oscillation remains stable but decreases in frequency (point 105) until the complex pair become real roots which have limiting values at the zeros on the real axis (point 106).

If we make T larger, for example equal to 50, so that the pole is located between the zeros on the real axis, the root locus appears as in Fig. 9b.

When K is equal to zero, the poles (point 112 and point 109) represent convergences and the complex pair (point 110) an unstable oscillation. As K is increased, the poles representing the convergences (point 112 and point 109) move toward and terminate at the zeros (point 108 and point 107). The pole at point 109 becomes a zero root when K reaches infinity, whereas the other pole (112) always represents a convergence.

The unstable oscillation (point 110) increases in frequency and becomes neutrally stable at point 111. As K is increased, the oscillation remains stable but the frequency continues to increase.

As suspected, depending on the value of the time lag, the addition of a lagged rate feedback device is able to stabilize the hovering platform to various degrees.

For pure rate feedback, when T in $\frac{K d}{1 + Td}$ is selected equal to zero ($T = \frac{1}{a} = \frac{1}{-\infty} = 0$), the extra pole is located at negative infinity ($a = -\infty$). As K is increased positively, the poles representing the unstable oscillation (point 100) move directly to the break point 106 in the left half plane instead of looping around (points 104 and 105) as in Fig. 9a. For this case the pole representing the convergence at point 102 stays in the left half plane and moves to the left as K is increased.

For pure attitude feedback, when T is selected as infinitely large ($T = \frac{1}{a} = \frac{1}{0} = \infty$), the extra pole (point 109) is located at the origin ($a = 0$) and cancels the zero (point 107) located there. The root locus for this case appears very similar to Fig. 9b.

Thus, the hovering Flying Platform may also be stabilized by either pure rate or attitude feedback or a combination of both.

The analysis of adding artificial stabilization to the hovering long chord duct is qualitatively the same as that of the short chord duct.

3. Long Chord Duct $\mu = 0.05$ V = 16 mph.

Referring to the boundaries of the quartic (Fig. 10A); it is seen that center of gravity movement has a primary effect on the value of $\bar{C}_{m_\mu}$ but only changes $\bar{C}_{m_\alpha}$ slightly. Actually, on this diagram, each inch of c.g. movement accounts for approximately 0.0031 change in $\bar{C}_{m_\mu}$ and 0.000014 change in $\bar{C}_{m_\alpha}$. It is evident that all c.g. locations are on the right side of the C = 0 line and therefore the C coefficient is always negative. If the c.g. is raised more than six inches above the original position, the D coefficient changes sign (point 1), and if raised by 12 inches (point 2), the E coefficient changes sign.

Referring to the stability diagram (Fig. 10B); it is noted that most of the c.g. locations fall within the region of unstable oscillations. If the c.g. is raised about nine inches (point 3) the unstable oscillations cease and divergences occur. Continuing to raise the c.g. (point 4) causes E to change sign so that even the static stability is now negative.

A better appreciation of the modes of motion can be obtained from the associated root locus plots. Note that the value of $\bar{C}_{m_\alpha}$ on the stability diagram is approximately equal to 0.002 and corresponds approximately to the value investigated in Fig. 10-I-c.

When $\bar{C}_{m_\mu}$ is equal to zero, the poles are located at point 5 and indicate the presence of two convergent and two divergent modes. The value or gain of $\bar{C}_{m_\mu}$ increases from zero, at the poles, to infinity along the direction of the arrows. As $\bar{C}_{m_\mu}$ is increased to the value at point 3 (the break point on the root locus and corresponding to point 3 in Fig. 10B), an unstable oscillation starts while the two other roots move along the arrows and remain convergent modes. Continuing to increase the gain of $\bar{C}_{m_\mu}$ to larger positive values along point 6, the oscillation increases in frequency and instability. The two other poles remain convergences regardless of the positive gain of $\bar{C}_{m_\mu}$.

The portion of the c.g. travel at which $\bar{C}_{m_\mu}$ is negative may be investigated by referring to Fig. 10-IV-c. Again at zero $\bar{C}_{m_\mu}$, there are the aperiodic modes, two convergences and two divergences (point 5). As the gain of $\bar{C}_{m_\mu}$ is increased negatively, it is seen that a stable oscillation starts (point 8) and one divergent mode becomes convergent. However, the predominating mode is the ever-increasing divergence (point 7), as $\bar{C}_{m_\mu}$ is increased negatively so that the overall mode of motion for $\bar{C}_{m_\mu}$ increasing negatively is an ever-increasing divergence.

The open-loop response in this case is a serious instability. If the roots calculated for the case with the original c.g. location are considered (Table I), it is seen that at $\mu = .05$ and V = 16 mph, there is an unstable oscillation with a period of 8.57 seconds and a time to double amplitude of only a little over two seconds. In other words, the oscillation would double amplitude in about one-quarter of the cycle.

4. Long Chord Duct $\mu = 0.10$ V = 34 mph

Referring to the boundaries of the quartic (Fig. 11A); it is seen that $\bar{C}_{m_\mu}$ changes approximately 0.0043 per inch of c.g. movement while $\bar{C}_{m_\alpha}$ changes 0.00014 per inch.

Starting with the center of gravity lowered six inches from the original location, it is noted that the c.g. is on the positive side (point 11) of the **C** = 0 line. As the c.g. is raised toward the original location, the **C** coefficient changes sign (point 12) and $\bar{C}_{m_\mu}$ decreases while $\bar{C}_{m_\alpha}$ increases. Continuing to raise the c.g. further, the **D** coefficient changes sign (point 13). When the center of gravity is raised six inches (point 14), the line **RLBP** has been crossed and $\bar{C}_{m_\mu}$ is negative. If the c.g. is raised a few more inches (point 15) the E coefficient changes sign.

Referring to the stability diagram (Fig. 11B); the points again are located principally in the region of unstable oscillations. The unstable oscillations cease if the c.g. is raised approximately six inches to point 14 at which location the **RLBP** line has been crossed and the dynamic instability takes the form of a divergence. If the c.g. is raised a few more inches, $\bar{C}_{m_\mu}$ continues to increase negatively and at point 15, E changes sign, so that now the configuration is even statically unstable.

For a closer look at the characteristic modes of motion reference is again made to the appropriate root locus plots. From the stability diagram note that $\bar{C}_{m_\alpha}$ ranges in value from approximately 0.001 to 0.004. The root locus plots for both these values are shown in Figs. 11-I-d and 11-I-e.

Fig. 11-I-d represents the locus when moving vertically up the line $\bar{C}_{m_\alpha}$ equal to 0.001 in the stability diagram (Fig. 11B) when $\bar{C}_{m_\mu}$ varies from zero to positive infinity. The initial position of the poles, when $\bar{C}_{m_\alpha}$ equals 0.001 and $\bar{C}_{m_\mu}$ equals zero, indicates that two convergences (point 16) and an unstable oscillation (point 17) exist. As

the gain of $\bar{C}_{m_\mu}$ is increased, (equivalent to moving upward along $\bar{C}_{m_\alpha}$ equal to 0.001 in the stability diagram) by moving in the direction of the arrows in the root locus diagram, two poles always remain convergences, one with ever-increasing value (point 18) and the other with decreasing value and a limit at the zero (point 19). The other two poles (point 17) continue as unstable oscillations with ever-increasing frequency and instability (point 20) as $\bar{C}_{m_\mu}$ is increased.

For C_{m_α} equal to 0.004 (Fig. 11-I-e), the picture is much the same, except that for $\bar{C}_{m_\mu}$ equal to zero, the four poles represent two convergences (point 21) and two divergences (point 22). As the gain of $\bar{C}_{m_\mu}$ is increased the convergences behave as before. However, the two poles representing the divergences (point 22) move toward each other and become equal roots at point 23, the root locus break point. This point (point 23) is also shown on the stability diagram. As the gain of C_{m_μ} is increased further, the two roots split as shown (point 24) and become unstable oscillations of increasing frequency and instability.

In order to cover the remaining center of gravity locations, (point 14 and point 15 in Fig. 11B), the root locus plots for $\bar{C}_{m_\alpha}$ equal to the same values, but $\bar{C}_{m_\mu}$ varying from zero to negative infinity, are analyzed (Fig. 11-IV-d and Fig. 11-IV-e).

In Fig. 11-IV-d, the four poles at $\bar{C}_{m_\mu}$ equal to zero represent two convergences (point 25) and an unstable oscillation (point 26). As the gain of $\bar{C}_{m_\mu}$ is increased negatively, the two convergent modes (point 25) move toward each other in the left half plane to the break point (point 27). As $\bar{C}_{m_\mu}$ is increased more negatively, they break away from the real axis and become a complex pair representing a stable oscillation of increasing frequency and decreasing damping ratio. In the meantime, as $\bar{C}_{m_\mu}$ is being increased from zero to negative infinity, the unstable

oscillation (point 26) is reducing frequency to the point where the complex pair of roots (point 26) become divergences, or equal real roots by joining on the real axis, (point 28). One divergent pole formerly at point 28 moves across the origin and becomes a convergence with a limiting value at the zero (point 29) in the left half plane. The other divergent pole, formerly at point 28, moves to the right, continuing as a divergence of ever-increasing instability (point 30).

For $\bar{C}_{m_\alpha}$ equal to 0.004 (Fig. 11-IV-e), the poles behave in much the same fashion with the exception that the unstable oscillation at point 26 becomes two unequal, positive, real roots, representing divergences when $\bar{C}_{m_\mu}$ equals zero. These poles move in much the same way as the positive real roots (point 28) move as $\bar{C}_{m_\mu}$ increases negatively. Note that in both cases there is always an instability present, either in the form of a divergence or an unstable oscillation for the range of C_{m_μ} from zero to negative infinity.

Again, the open-loop response for this case is a serious instability. Considering the roots calculated for the case of the original c.g. location (Table III), for $\mu = 0.10$ and V = 34 mph, two convergences and an unstable oscillation exist. The predominating mode of motion for this case is the unstable oscillation with a ten second period and a two second time to double amplitude. Therefore, the aircraft doubles amplitude in approximately 1/5 of a cycle.

5. Long Chord Duct Artificial Stabilization Added $\mu = 0.10$ V= 34mph

Arbitrarily choosing to investigate the effects of artificial stabilization on the dynamic stability associated with the vertical center of gravity located at the original location, an instability exists in the form of an unstable oscillation (Fig. 12, points 140 and 150). Taking the case of pure attitude feedback (Fig. 12a); one pole cancels with a zero at the

origin (T equals infinity), the remaining poles represent two convergences (point 141 and point 142) and the unstable oscillation (point 140). As K is increased, the unstable oscillation (point 140) becomes neutral (point 146) and finally stable, with the oscillation reaching a limiting value at the zeros (point 143). The two poles at point 141 and point 142 join at point 144 and break away from the negative real axis to become a stable oscillation of increasing frequency (point 145) as K is increased.

For the case of pure rate feedback (Fig. 12b), a zero is located at the origin (T equals zero), and the other poles and zeros are located in the same position as in Fig. 12a. The unstable oscillation (point 150) and the two convergent poles (points 151 and 152) still exist as before.

However, as the gain K is increased, the poles of the unstable oscillation (point 150) move into the left half plane (point 156) and become a stable oscillation with a limiting value at the zeros (point 154). Notice that they move in a more direct line contrasted to the former case where the loci loop around (point 146) when moving toward the zero (143).

To investigate intermediate values of T (pure rate feedback with various degrees of lag), refer to Fig. 12a. Locating a zero at the origin with a pole very close to it but in the left half plane, the loci are essentially unchanged. As this pole moves to the left or away from origin (T decreasing), the loci between point 140 and point 143 tend to describe paths that become more and more direct until they appear exactly like the loci between point 150 and 154 when the moving pole reaches negative infinity. The other loci for point 141 and 142 remain similar except that the break point (point 144) continues to move to the left as the moving pole passes the position point 142. The pole at point 142, in this case, always moves to the right and terminates at the zero located at the origin.

From this analysis, it is evident that a pure rate feedback with various degrees of lag can be used to stabilize the system and exert some control on the frequency and damping ratio of this particular configuration.

6. Short Chord Duct $\mu = 0.05$ V = 18 mph

Referring to the boundaries of the quartic (Fig. 13A); $\bar{C}_{m_\mu}$ changes approximately 0.002 per inch of vertical c.g. movement while $\bar{C}_{m_\alpha}$ changes very slightly, say 0.00001 per inch movement. All center of gravity locations have positive $\bar{C}_{m_\alpha}$ and are located to the left (positive side) of the C = 0 line so that the C coefficient in the stability quartic is always positive for this case. However, if the c.g. is raised almost six inches above the original location (point 34), the E coefficient changes sign so that a dynamic instability appears in the form of a divergence, due to the static instability. Raising the c.g. slightly further (point 35), $\bar{C}_{m_\mu}$ becomes negative and an additional increment of upward travel causes the D coefficient to change sign as well (point 35).

Referring to the stability diagram (Fig. 13B); the center of gravity located six inches below the original location lies in a region of unstable oscillations (point 31). As the center of gravity is raised past the original c.g. location (point 32) ($\bar{C}_{m_\mu}$ decreasing) it crosses the line R = 0 (point 33), thereby ending the unstable oscillation, and passes through a small portion of the stable region before crossing the E = 0 line (point 34) into the divergent region. If the c.g. is raised further, $\bar{C}_{m_\mu}$ changes sign (point 35).

To detefmine the characteristic modes of motion for this case, reference is again made to the appropriate root locus plot. From the stability diagram, $\bar{C}_{m_\alpha}$ is in the range of approximately 0.0002. The closest value in the root locus plots is $\bar{C}_{m_\alpha}$ equal to 0.0005. Analyzing the plot (Fig. 13-I-b), which closely resembles the character of the motion for the exact value of $\bar{C}_{m_\alpha}$, the following statements can be made:

When $\bar{C}_{m_\alpha}$ equals 0.0005 and $\bar{C}_{m_\mu}$ equals zero, one pole (point 36) indicates a convergence, the second (point 37) a divergence and the

remaining two (point 38) a stable oscillation. This is approximately the situation existing at point 35 on the stability diagram (Fig. 13B) for the c.g. location six inches above the original. As $\bar{C}_{m_\mu}$ is increased from zero to positive infinity, the pole at point 36 continues as an increasing convergence (point 48), i.e., this transient mode tends to die out faster. The divergent pole at point 37 moves from the right half plane, across the origin (point 34), becoming a convergence in the left half plane and reaching a limiting value at the zero (point 49) when $\bar{C}_{m_\mu}$ is increased to positive infinity.

With respect to the two poles at point 38; they increase in frequency and move from the stable left half plane across the imaginary axis of neutral oscillations (point 33) into the region of unstable oscillations in the right half plane of the root locus diagram.

It is interesting to compare the appropriate root locus plot to the equivalent locations on the stability diagram (Fig. 13B). Notice in the root locus diagram (Fig. 13-I-b) the divergent pole at point 37 becomes a zero root at point 34 which means that the E coefficient must equal zero at that point.

On the stability diagram, point 34 is located by the intersection of the value of $\bar{C}_{m_\alpha} = 0.0002$ and the E = 0 line. By closely inspecting the stability diagram, it is evident that further increases in $\bar{C}_{m_\mu}$ result in moving upward across the E = 0 line (point 34) into a region of stable oscillations, between point 34 and point 33, on the stability diagram. Additional increase of $\bar{C}_{m_\mu}$ results in moving across the R = 0 line (point 33) into the region of unstable oscillations.

On the root locus diagram this means that the pole at point 37 becomes a convergence (point 34) before the stable oscillation (point 38) becomes unstable at point 33. Further increases in $\bar{C}_{m_\mu}$ on the root locus diagram cause the unstable oscillation to become more severe.

To cover the remaining c.g. locations which are raised sufficiently to make $\bar{C}_{m_\mu}$ negative (Fig. 13B), the root locus diagram Fig. 13-IV-b may be investigated. The value of $\bar{C}_{m_\alpha}$ is still 0.0005, but $\bar{C}_{m_\mu}$ varies from zero to negative infinity on this diagram. The poles located for $\bar{C}_{m_\mu}$ equal to zero represent a convergence (point 39), a divergence (point 45) and a stable oscillation (point 40 and point 41). As the gain of $\bar{C}_{m_\mu}$ is increased negatively, the poles at point 40 and point 41 start decreasing frequency as they approach the negative real axis along the direction of the arrows. Upon reaching the entry point (point 47) the complex pair becomes two equal, real, negative roots. As $\bar{C}_{m_\mu}$ continues to be increased negatively, the two equal roots at point 47 split and move along the negative real axis in opposite directions with one terminating at the zero (point 43) when $\bar{C}_{m_\mu}$ is equal to negative infinity. Meanwhile, the other pole moves from 47 to the left on the real axis, where it joins with the original convergent pole (formerly at point 39) at the root locus break point (point 42). At point 42 they become real, equal, negative roots and as $\bar{C}_{m_\mu}$ continues to increase negatively they break away from the real axis at point 42 to become a complex pair, indicating an oscillation of increasing frequency (point 44).

In the meantime, there is always a divergent pole (point 45) which becomes increasingly unstable (point 46) as $\bar{C}_{m_\mu}$ is increased negatively.

Again, reference is made to Table II for the roots of the quartic for the short chord duct at $\mu = 0.05$, V = 18 mph and the c.g. located in the original position. The modes of motion are two convergences and an unstable oscillation with approximately a ten second period and a seven second time to double amplitude. This open-loop response, though unstable, seems to be more reasonable than the others. In fact, if $\bar{C}_{m_\mu}$ is decreased by raising the c.g., the configuration is located in the small stable region shown on the stability diagram between point 33 and point 34 in Fig. 13B. Actually, this stable region is so small that it is probably insignificant.

7. Short Chord Duct $\mu = 0.10$ V = 36 mph

Referring to the boundaries of the stability quartic (Fig. 14A); $\bar{C}_{m_\mu}$ changes approximately 0.003 per inch of vertical c.g. movement while $\bar{C}_{m_\alpha}$ changes 0.0001 per inch of movement. All the center of gravity locations appear in the divergent region where the coefficients C, D and E are negative, except for the lowest location (point 54) where only C and E are negative. The highest c.g. location has such a large negative value of $\bar{C}_{m_\mu}$ that it is not on the figure.

Starting in the region labeled 'unstable oscillations' and decreasing $\bar{C}_{m_\mu}$ along the line of centers of gravity, the E coefficient changes sign at point 52. Slightly below point 52 the axis is crossed and $\bar{C}_{m_\mu}$ becomes negative. By increasing $\bar{C}_{m_\mu}$ negatively the C coefficient changes sign at point 53 and the location of $\bar{C}_{m_\mu}$ and $\bar{C}_{m_\alpha}$, for the c.g. located six inches below the original, is finally reached (point 54). Raising the c.g. still further, the D coefficient changes sign at point 55 and $\bar{C}_{m_\mu}$ continues to increase negatively as the higher c.g. locations are approached (point 56).

Referring to the stability diagram (Fig. 14B); all the c.g. locations fall in the region of dynamic instability. The points are below, or on the negative side of, the E = 0 line.

The characteristic modes of motion for these center of gravity locations can be obtained from the root locus diagram.

Varying $\bar{C}_{m_\mu}$ negatively at $\bar{C}_{m_\alpha}$ equal to 0.001 approximately covers the region in which the centers of gravity are located. In Fig. 14-IV-c when $\bar{C}_{m_\mu}$ equals zero, one pole is located slightly to the right of the origin and represents a divergence (point 60). Another pole is located in the left half plane and represents a convergence (point 61). The other two poles (point 62) are a complex pair located in the right half plane and

represent an unstable oscillation. As the gain of $\bar{C}_{m_\mu}$ is increased negatively, the pole at point 61 moves to the right, and has a limiting value at the zero (point 63) when $\bar{C}_{m_\mu}$ is infinite. This pole (point 61) remains in the stable region or left half plane and always represents a convergence which takes place with decreasing rapidity as $\bar{C}_{m_\mu}$ is increased negatively.

The two poles at point 62 move along the direction of the arrows (point 65) as $\bar{C}_{m_\mu}$ is increased negatively. The lightly damped unstable oscillation (point 62) increases frequency and becomes a neutral oscillation (point 64) and then an unstable oscillation with ever-increasing frequency (point 65).

The predominating mode of motion for this quadrant is the divergent pole (point 60) located in the right half plane, or unstable region, when $\bar{C}_{m_\mu}$ equals zero. This pole moves to the right (point 66) and causes the transient motion of the machine to become more unstable as $\bar{C}_{m_\mu}$ is increased negatively.

If the center of gravity is lowered considerably more than six inches, through some design change, $\bar{C}_{m_\mu}$ becomes positive. Investigating the root locus using the extrapolated value of $\bar{C}_{m_\alpha} \approx 0.001$ and $\bar{C}_{m_\mu}$ varying from zero to positive infinity, the root locus appears as Fig. 14-I-c. The poles for $\bar{C}_{m_\mu}$ equal to zero, indicate a convergent mode at point 67, an unstable oscillation at point 69, and the fourth pole (point 68) close to the origin is actually in the right half plane (shown by close analysis of Fig. 14-I-h or Fig. 14C-b for $\bar{C}_{m_\alpha}$ increased positively to 0.001 while $\bar{C}_{m_\mu}$ equals zero) and represents a divergence. As the gain of $\bar{C}_{m_\mu}$ is increased positively from zero, the pole representing a divergence (point 68) moves to the left toward the origin and into the left half plane to become a convergence (point 71). The pole at point 67 always moves to the left (point 70) and remains in the left half plane as a convergence.

The complex pair (point 69) remains unstable and represents an oscillatory mode of increasing frequency and instability (point 72).

For the case of the actual c.g. locations, $\bar{C}_{m_\alpha}$ positive and $\bar{C}_{m_\mu}$ negative, as shown on the stability diagram, the open loop response is a serious instability.

Taking the specific case of the values of $\bar{C}_{m_\mu}$ and $\bar{C}_{m_\alpha}$ <u>at the original c.g. location</u> (where $\bar{C}_{m_\mu}$ is admittedly very unstable), the roots of the characteristic equation (Table II) for $\mu = 0.10$ V = 36 mph clearly define the modes of motion. The convergence and stable oscillation are strongly masked by an instability in the form of a divergence that doubles in amplitude in less than a second (T = 0.8068 seconds).

8. Short Chord Duct Artificial Stabilization Added $\mu = 0.10$ V = 36

For the short chord duct at $\mu = 0.10$, there is a dynamic instability in the form of a divergence.

Analyzing the limit cases of pure rate feedback (T = 0) and pure attitude feedback (T = ∞), the root loci appear as in Fig. 15. The pole at point 120 represents the instability due to the divergence and the zeros are located for increasing K from zero to infinity. When T is equal to infinity, the pole and the zero located at the origin cancel each other. When T is equal to zero, the pole is located at negative infinity and the zero remains fixed at the origin.

In the case of pure attitude feedback (Fig. 15a), where the pole cancels the zero at the origin (T equal to infinity) the remaining poles represent a stable oscillation (point 115), a convergence (point 117), and the divergence (point 120). As K is increased the stable oscillation (point 115) continues, but increases in frequency (point 116). The poles at point 117 and point 120 move toward each other until they become equal roots at the root locus break point (point 119) in the right half plane. As K is increased further, the poles break away from the positive

real axis (point 119) and become an unstable oscillation, a neutral oscillation (point 121), and finally a stable oscillation with a limiting value at the zeros (point 118) in the left half plane.

For the case of pure rate feedback (Fig. 15b), in which a zero (point 135) is located at the origin (T equal to zero), the same modes of motion prevail as before when K is equal to zero. However, in this case, as K is increased, the poles at point 130 move toward the break point (point 131) and split so that one moves toward point 132 and the other toward point 133. The pole reaching point 133 joins the pole formerly at point 135 to break away from the real axis into the stable oscillation which reaches a limiting value at the zeros (point 134). Meanwhile, the pole (point 137) representing the divergence can only become a zero root at point 136 when K is increased to infinity.

In order to study the effects of various degrees of lag, an extra pole is situated in the left half plane, very close to the zero (point 136). As K is increased, it will join with the pole at point 135 and break away as a stable oscillation terminating at the zeros (point 134). The poles at point 130 remain as stable oscillations which move away from the real axis and continue as stable oscillations of ever-increasing frequency.

As this extra pole is moved to the left, away from the zero (point 136), the former description of the loci remains much the same except as it moves past the vicinity of point 131 toward point 132. When the extra pole moves in this direction it pulls the loci of point 130 closer and closer to the real axis until, at some large negative location, the poles (point 130) join on the real axis similarly to that shown at point 131.

The pole located at point 137 always moves to the zero (point 136) and the basic path is not influenced by the extra pole moving in the left half plane.

From this analysis it is possible to note that pure attitude feedback can stabilize this system (point 121 and point 118) for some value of gain, K, whereas pure rate feedback can only yield a zero root (point 136).

The gyro-bar with either aerodynamic or mechanical damping represented by the transfer function for a lagged rate feedback, $\frac{Kd}{1 + Td}$, should not be referred to as a method of providing rate and attitude feedback. These devices do not sense attitude and therefore provide only rate feedback with a phase lag. While it may be true that a lagged rate feedback provides a frequency and phase characteristic similar to that of combined rate and attitude feedback, this is only true within a certain frequency range so that, strictly speaking, there really is no direct equivalence.

For this reason the gyro-bar devices may be able to diminish the degree of dynamic instability of an aircraft in forward flight associated with a divergence due to a static instability, ($E < 0$), but they can never completely stabilize the system. This is exactly the case for the short chord duct at μ equal to 0.10 and the c.g. in the original location. Even at infinite gain, K, the divergent pole (point 137) can only be made a zero root (point 136).

An understanding of the characteristic modes of motion for configurations of the Flying Platform with other combinations of values for $\bar{C}_{m_\mu}$ and $\bar{C}_{m_\alpha}$ not discussed is possible by reference to the other root loci provided for all the quadrants of each stability diagram.

CONCLUSIONS

Generally, the unstabilized, seven-foot diameter, ducted rotor Flying Platform exhibits a degree of control-fixed dynamic instability with either the long or short chord duct for all vertical center of gravity locations.

In hovering, both duct configurations are dynamically unstable due to the large positive values of $\bar{C}_{m_\mu}$. This instability is characterized by an unstable oscillation for all center of gravity locations considered.

In forward flight, both duct configurations exhibit dynamic instability characterized by unstable oscillations for the lower c.g. locations and divergences for the higher c.g. locations.

For any of the configurations, artificial stabilization, using a rate feedback with a phase lag as provided by a gyro-bar, is able to correct a dynamic instability when it is of the form of an unstable oscillation. When the instability is characterized by a divergence the lagged rate feedback device cannot completely overcome the instability. However, a combination of rate and attitude or pure attitude feedback can stabilize this divergence.

The commonly used gyro-bars with aerodynamic or mechanical damping can only provide rate feedback with a phase lag and never provide any of the attitude feedback required to completely correct the instability associated with a positive real root of a characteristic equation. However, lagged rate feedback may certainly help to minimize this type of an instability even though it can never completely overcome it.

The large tilt angles predicted for the faster trimmed flight speeds will become a problem for either duct configuration. For the ducted rotors studied, these excessive tilt angles cannot be attained because the pilot has insufficient control moment input to trim the large moments generated by the aircraft for the higher speeds.

In general, for given c.g. locations the moments produced by the short chord duct were less than the long chord duct, but the moment could be reduced for either duct by raising the center of gravity.

Any attempt to increase the attainable forward speed by compromising between these duct designs or center of gravity locations does not produce significant or desirable results. Reducing the moment by raising the c.g. causes the divergent mode to appear (point where the duct becomes statically unstable or $\frac{dM}{dV} = E = 0$) at successively lower flight speeds.

REFERENCES

1. Zimmerman, C.H.; Hill, Paul R.; and Kennedy, T.L. "Preliminary Experimental Investigation of the Flight of a Person Supported by a Jet Thrust Device Attached to his Feet." N.A.C.A. RM L52D10, January 15, 1953.

2. Gill, W.J. "Wind Tunnel Tests of Several Ducted Propellers in Non-Axial Flow." Report No. ARD-224, Hiller Aircraft Corporation, April 20, 1959.

3. Townsend, M. William, and Seckel, Edward. "Stability and Control of Unducted Stand-On Helicopters." Proceedings of the Fourteenth Annual National Forum, American Helicopter Society, April 16-19, 1958.

4. Townsend, M. William "Stability and Control of Unducted Stand-On Helicopters: Preliminary Theoretical and Flight Test Results." Princeton University, Department of Aeronautical Engineering, Report No. 404, November 1957.

5. Perkins, Courtland D., and Hage, Robert E. "Airplane Performance Stability and Control." John Wiley & Sons, Inc. 1949.

6. O'Hara, F. "An Analysis of the Longitudinal Stability and Control of a Single-Rotor Helicopter." Ministry of Supply, Aeronautical Research Council, R. & M. No. 2958. July 1954.

7. Evans, Walter R. "Control-System Dynamics" McGraw-Hill Book Company, Inc. 1954.

8. Savant, C.J., Jr. "Basic Feedback Control System Design." McGraw-Hill Book Company, Inc. 1958.

9. Schmitt, Thomas J. "Wind Tunnel Investigations of Air Loads on Human Beings." Report No. 892. Aero 858. David Taylor Model Basin Aerodynamics Laboratory, January 1954.

TABLE I

CHARACTERISTIC EQUATIONS OF THE LONG CHORD DUCT

Center of gravity located in the original position (0.42c)

T - Time to double or half amplitude P - Period of oscillation

Stability Cubic $\lambda^3 + 0.31272\,\lambda^2$	Hovering $\mu = V = 0$ $+ 0.046425\,\lambda$	$\tau = 0.3864$ $+ 0.37872 = 0$
Roots $\lambda_1 = -0.81973$		$T = 0.32666$ seconds
Roots $\lambda_2 = 0.2535 + 0.630691i$ $\lambda_3 = 0.2535 - 0.630691i$		$T = 1.0563$ seconds. $P = 3.8495$ seconds

Stability Quartic $\lambda^4 + 0.53207\,\lambda^3$	$\mu = 0.05$ $- 0.00007544\,\lambda^2$	V = 16 mph $+ 0.055276\,\lambda$	$\tau = 0.3944$ $+ 0.00868 = 0$
Roots $\lambda_1 = -0.13976$			$T = 1.956$ seconds
Roots $\lambda_2 = -0.63364$			$T = 0.43135$ seconds
Roots $\lambda_3 = 0.12066 + 0.288871i$ $\lambda_4 = 0.12066 - 0.288871i$			$T = 2.265$ seconds $P = 8.5786$ seconds

Stability Quartic $\lambda^4 + 0.62572\,\lambda^3$	$\mu = 0.10$ $- 0.0031\,\lambda^2$	V = 34 mph $+ 0.0282\,\lambda$	$\tau = 0.3809$ $+ 0.010023 = 0$
Roots $\lambda_1 = -0.21140$			$T = 1.2486$ seconds
Roots $\lambda_2 = -0.66036$			$T = 0.39973$ seconds
Roots $\lambda_3 = 0.12302 + 0.238051i$ $\lambda_4 = 0.12302 - 0.238051i$			$T = 2.1457$ seconds $P = 10.054$ seconds

TABLE II

CHARACTERISTIC EQUATIONS OF THE SHORT CHORD DUCT

Center of gravity located in the original position (0.42c)

T - Time to double or half amplitude P - Period of oscillation

Stability Cubic $\lambda^3 + 0.34493\lambda^2$	Hovering $\mu = V = 0$ $+ 0.014260\lambda$	$\tau = 0.33926$ $+ 0.073105 = 0$
Roots $\lambda_1 = -0.55575$		$T = 0.42304$ seconds
Roots $\lambda_2 = 0.1054 + 0.346841$ $\lambda_3 = 0.1054 - 0.346841$		$T = 2.2306$ seconds $P = 6.1459$ seconds

Stability Quartic $\lambda^4 + 0.45072\lambda^3$	$\mu = 0.05$ $+ 0.04044\lambda^2$	V = 18 mph $+ 0.02577\lambda$	$\tau = 0.351$ $+ 0.0013625 = 0$
Roots $\lambda_1 = -0.05511$		$T = 4.414$ seconds	
Roots $\lambda_2 = -0.46847$		$T = 0.5192$ seconds	
Roots $\lambda_3 = + 0.03643 + 0.226821$ $\lambda_4 = + 0.03643 - 0.226821$		$T = 6.677$ seconds $P = 9.7231$ seconds	

Stability Quartic $\lambda^4 + 0.54622\lambda^3$	$\mu = 0.10$ $+ 0.00029\lambda^2$	V = 36 mph $- 0.058851\lambda$	$\tau = 0.359$ $- 0.006944 = 0$
Roots $\lambda_1 = + 0.30838$		$T = 0.8068$ seconds	
Roots $\lambda_2 = - 0.13518$		$T = 1.8484$ seconds	
Roots $\lambda_3 = - 0.35971 + 0.192851$ $\lambda_4 = - 0.35971 - 0.192851$		$T = 0.69163$ seconds $P = 11.6964$ seconds	

TABLE III

OVERALL VALUE OF STABILITY DERIVATIVES

FOR VARIOUS C. G. LOCATIONS

LONG CHORD DUCT								
μ	C.G. LOCATION 0.5 FEET DOWN		C.G. LOCATION ORIGINAL		C.G. LOCATION 0.5 FEET UP		C.G. LOCATION 1.0 FEET UP	
	$\overline{C}_{m_\alpha}$	$\overline{C}_{m_\mu}$	$\overline{C}_{m_\alpha}$	$\overline{C}_{m_\mu}$	$\overline{C}_{m_\alpha}$	$\overline{C}_{m_\mu}$	$\overline{C}_{m_\alpha}$	$\overline{C}_{m_\mu}$
μ=0	0	0.1772	0	0.1604	0	0.1435	0	0.1266
μ=.05	0.0021	0.0510	0.0022	0.0324	0.0023	0.0136	0.0024	- 0.0051
μ=.10	0.0005	0.0506	0.0014	0.0250	0.0022	- 0.0005	0.0032	- 0.0266

SHORT CHORD DUCT								
μ	C.G. LOCATION 0.5 FEET DOWN		C.G. LOCATION ORIGINAL		C.G. LOCATION 0.5 FEET UP		C.G. LOCATION 1.0 FEET UP	
	$\overline{C}_{m_\alpha}$	$\overline{C}_{m_\mu}$	$\overline{C}_{m_\alpha}$	$\overline{C}_{m_\mu}$	$\overline{C}_{m_\alpha}$	$\overline{C}_{m_\mu}$	$\overline{C}_{m_\alpha}$	$\overline{C}_{m_\mu}$
μ=0	0	0.0465	0	0.0402	0	0.0339	0	0.0276
μ=.05	0.00005	0.0239	0.0001	0.0121	0.0002	0.00013	0.00025	- 0.0119
μ=.10	0.0011	-0.0099	0.0017	-0.0272	0.0025	-0.0446	0.0032	- 0.0621

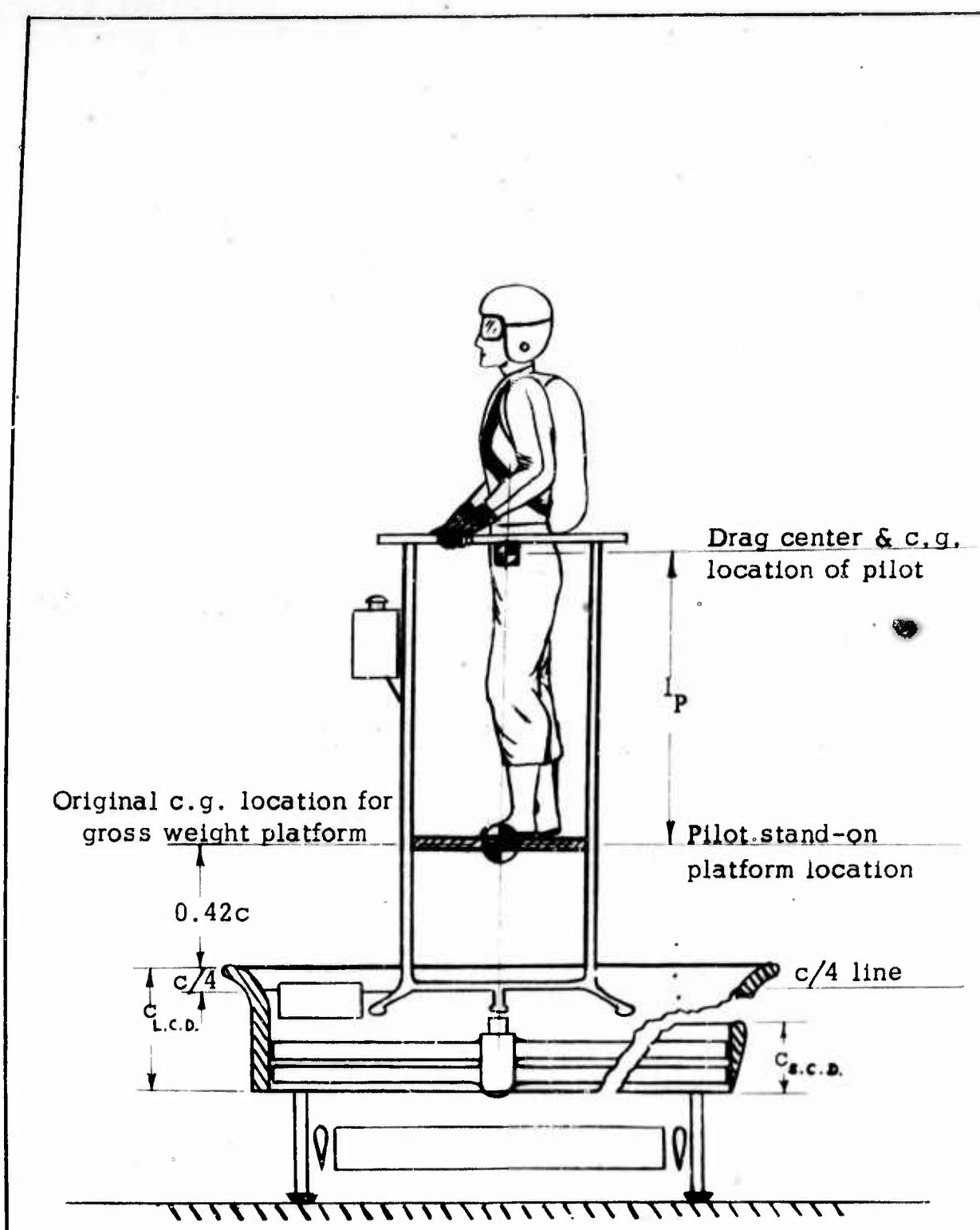

FIGURE 1 FLYING PLATFORM

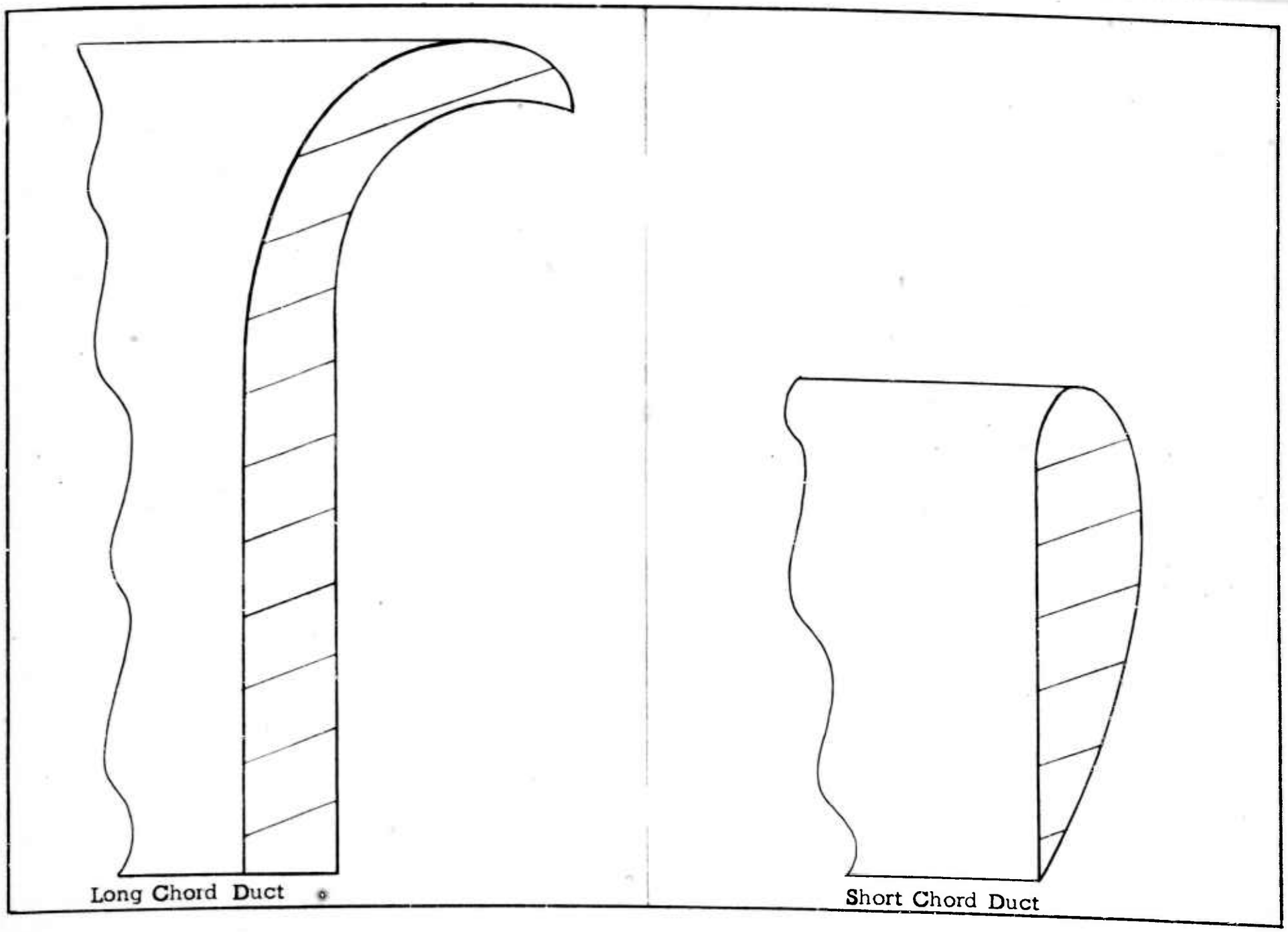

FIGURE 2 FULL SIZE DUCT PROFILES FOR WIND TUNNEL MODEL TESTS

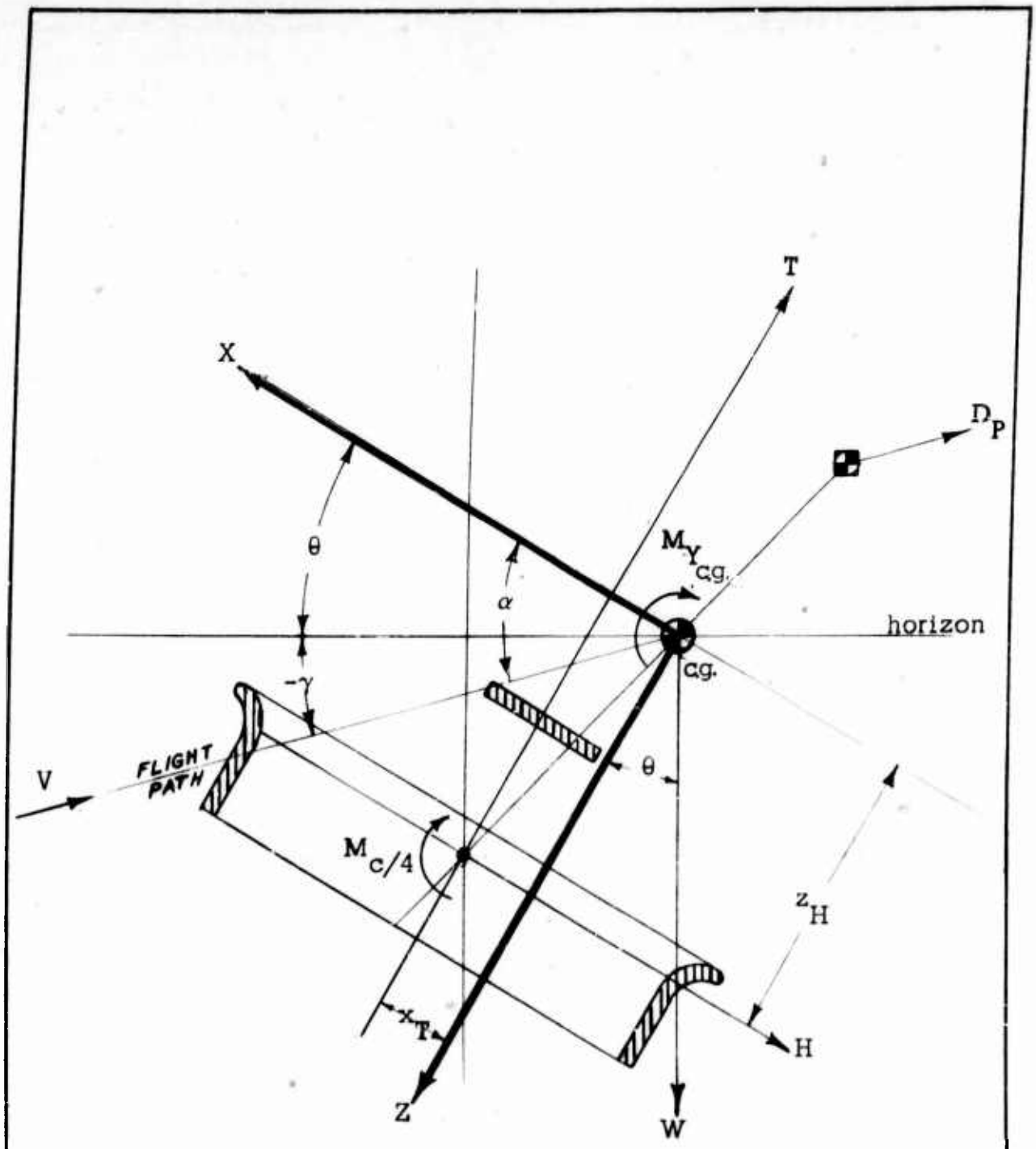

All notation shown is positive except flight path angle to horizon , γ .

FIGURE 3 BODY AXIS SYSTEM

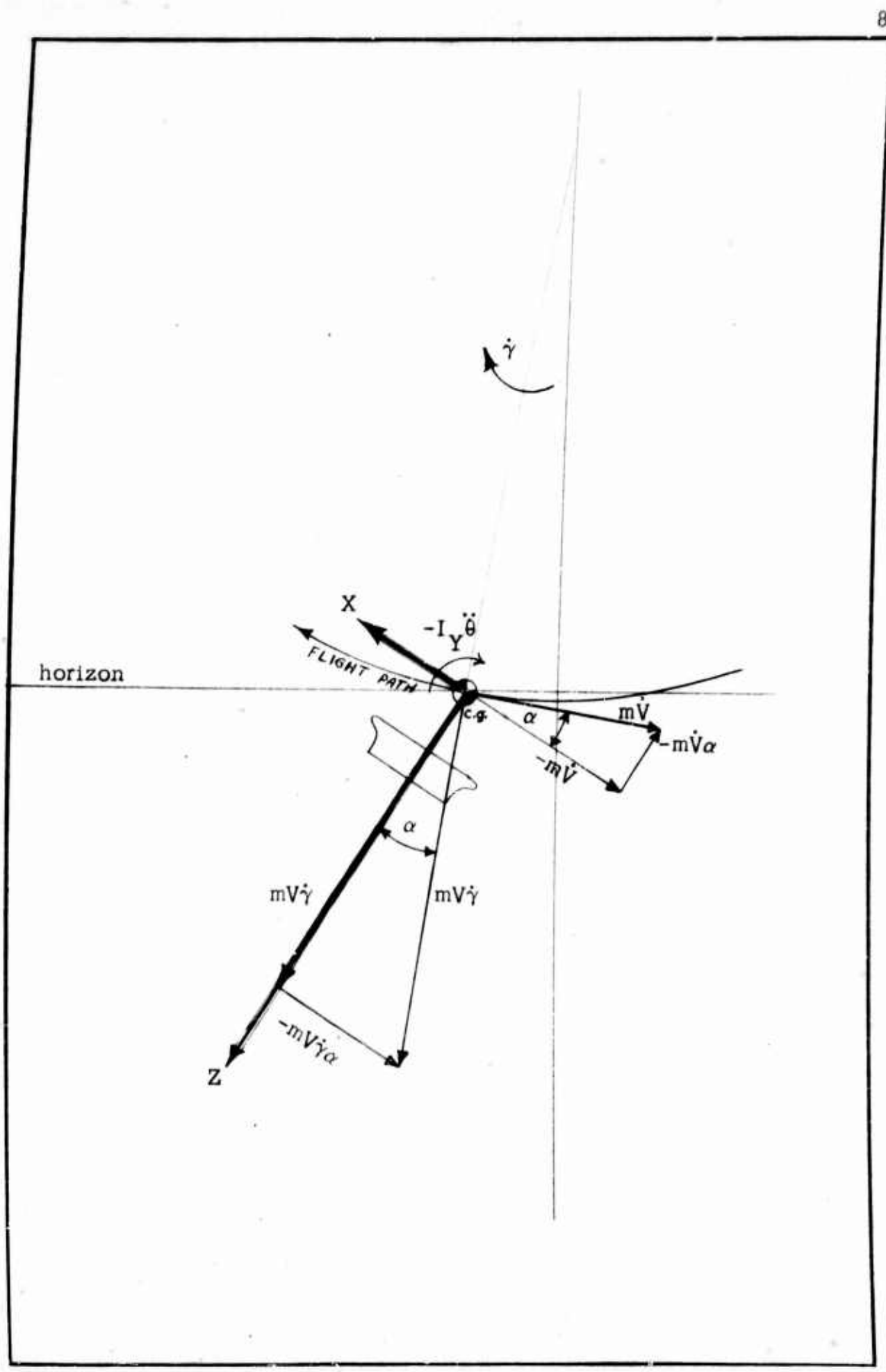

FIGURE 4 BODY AXIS INERTIA TERMS - CURVED FLIGHT PATH

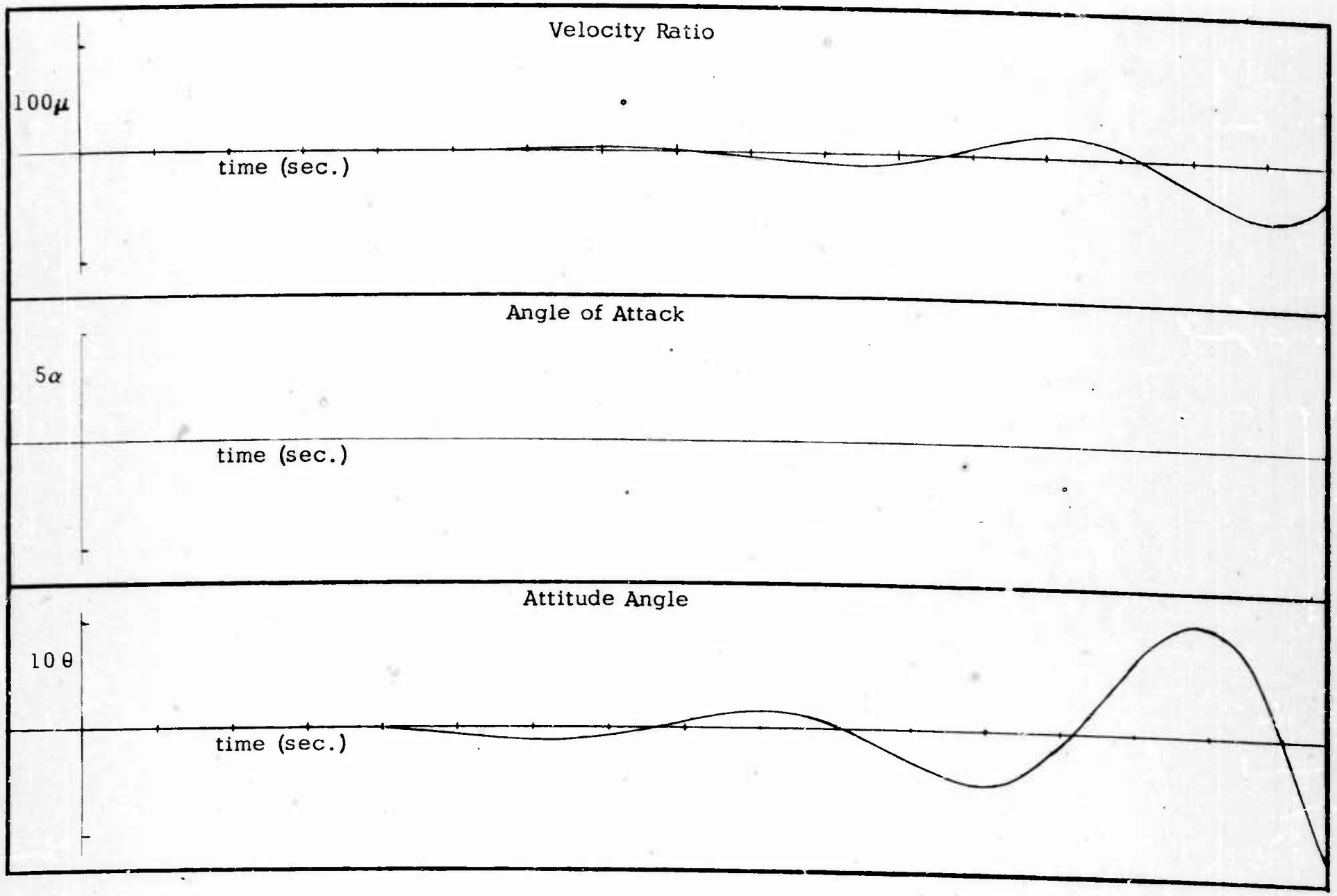

FIGURE 5 TYPICAL TIME RESPONSE TO A SMALL INPUT IN HOVERING

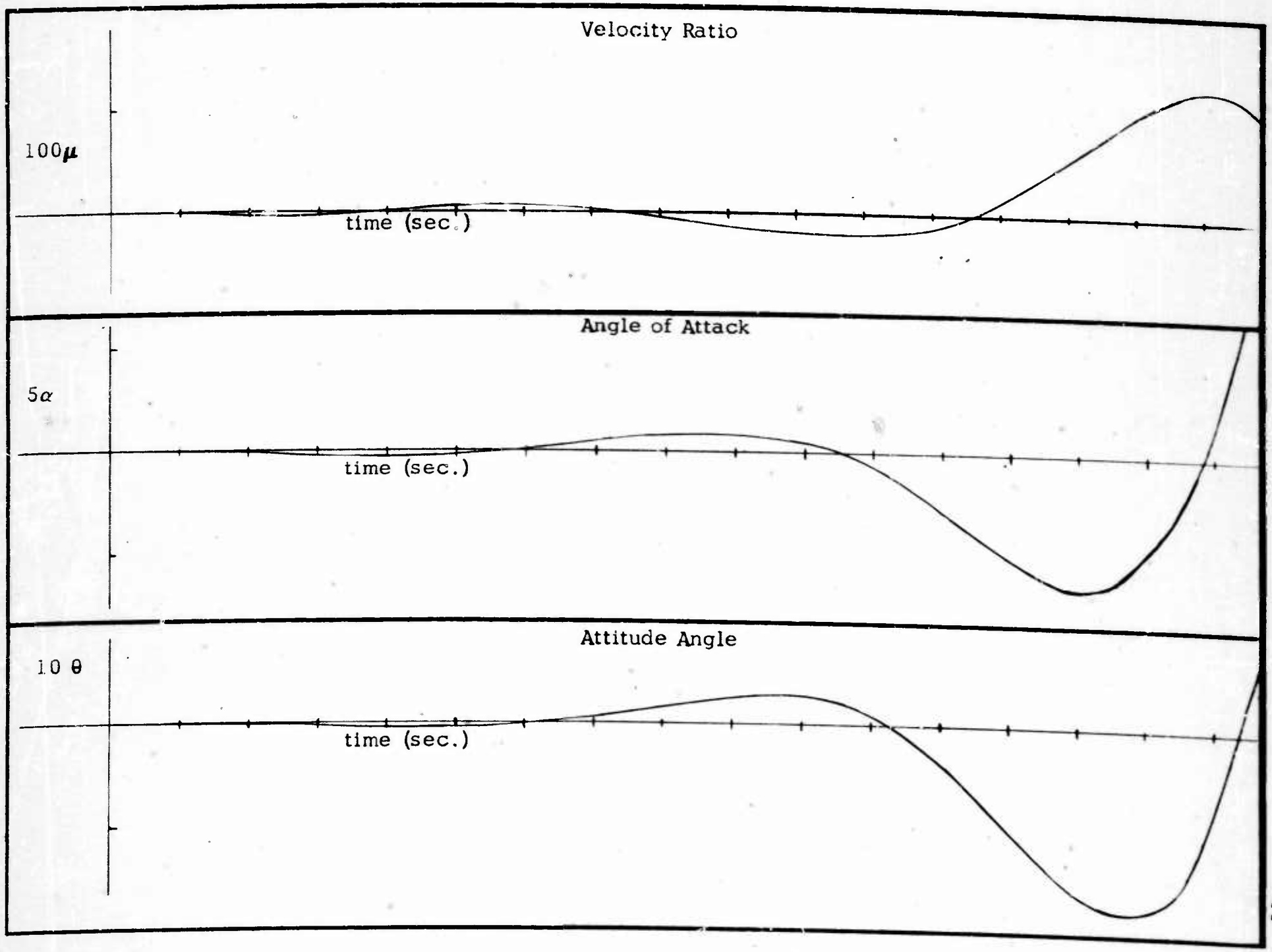

FIGURE 6 TYPICAL TIME RESPONSE TO A SMALL INPUT IN FORWARD FLIGHT

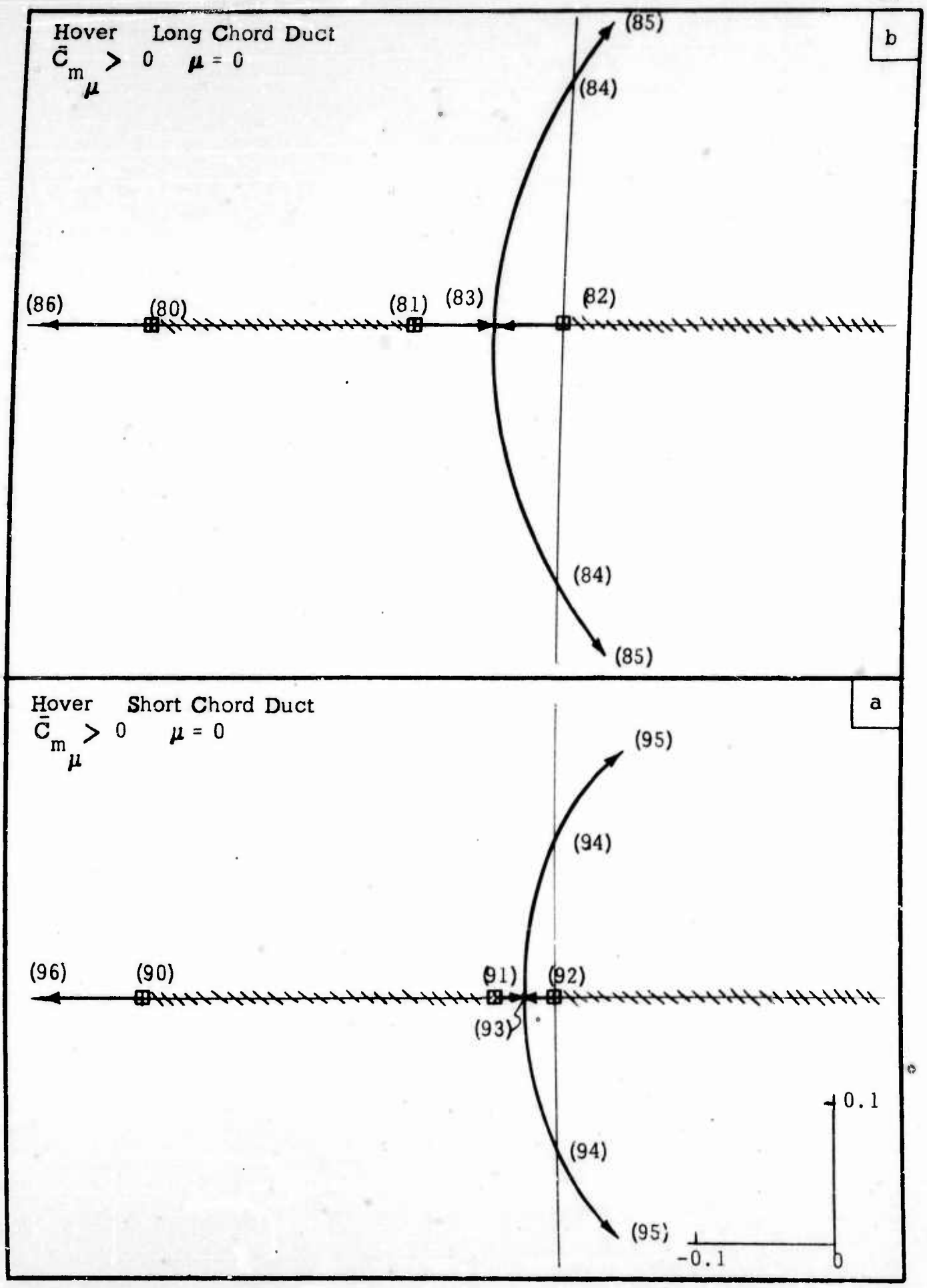

FIGURE 7 ROOT LOCUS S.C.D. AND L.C.D. HOVER

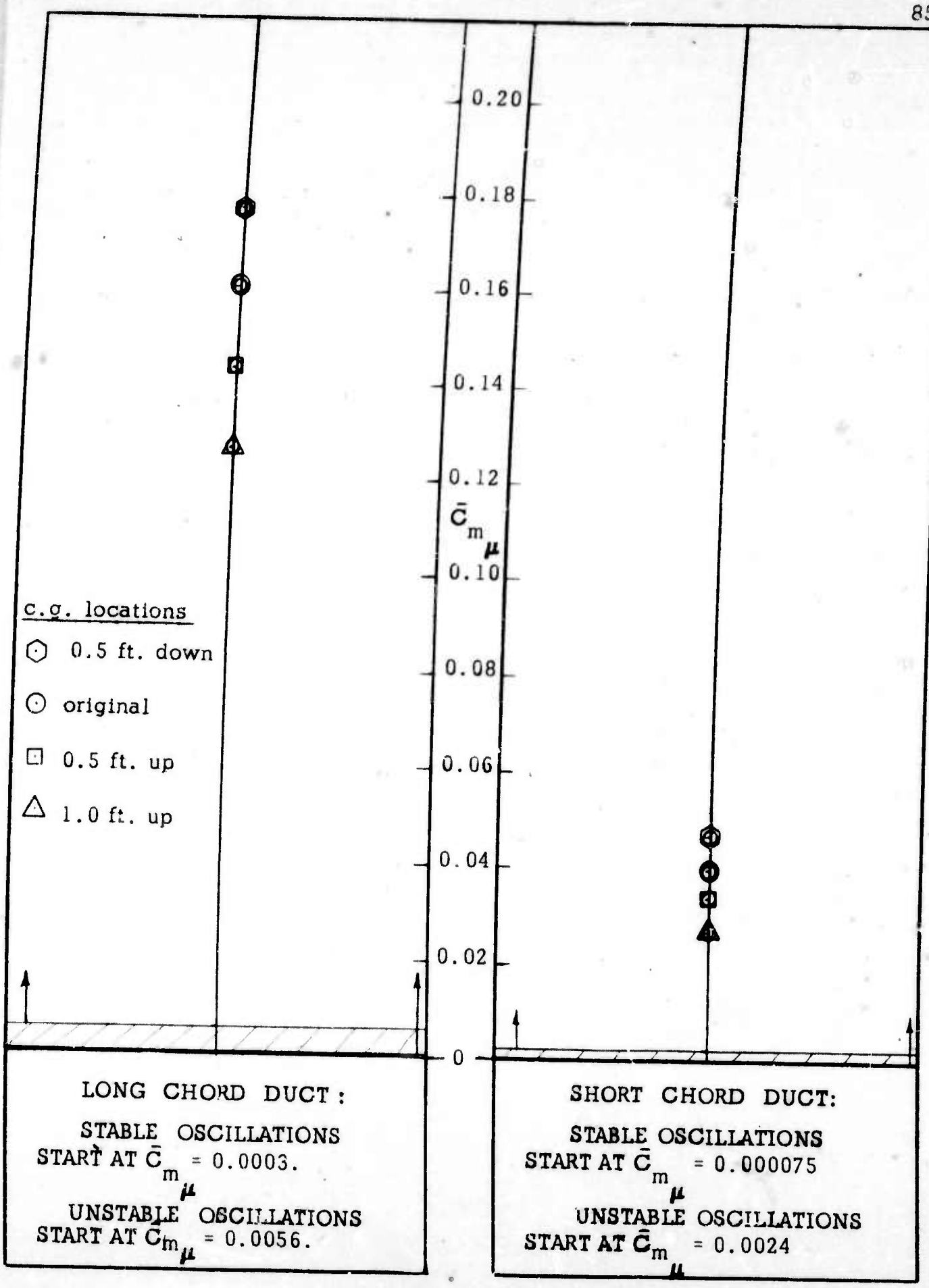

FIGURE 8 STABILITY DIAGRAM FOR HOVER $\bar{C}_{m_\mu} > 0$.

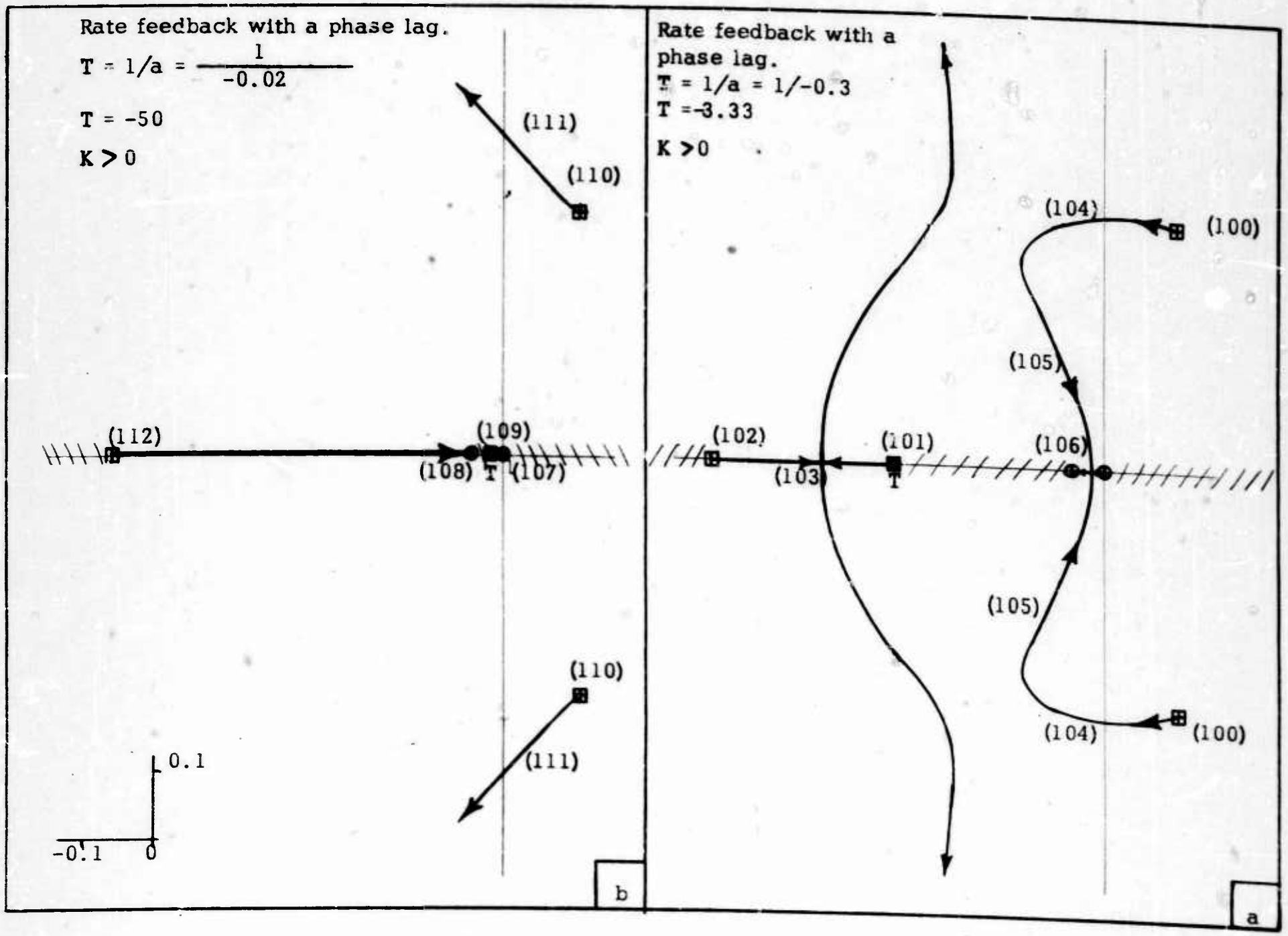

FIGURE 9 ROOT LOCUS S.C.D. HOVER-ARTIFICIAL STABILIZATION ADDED

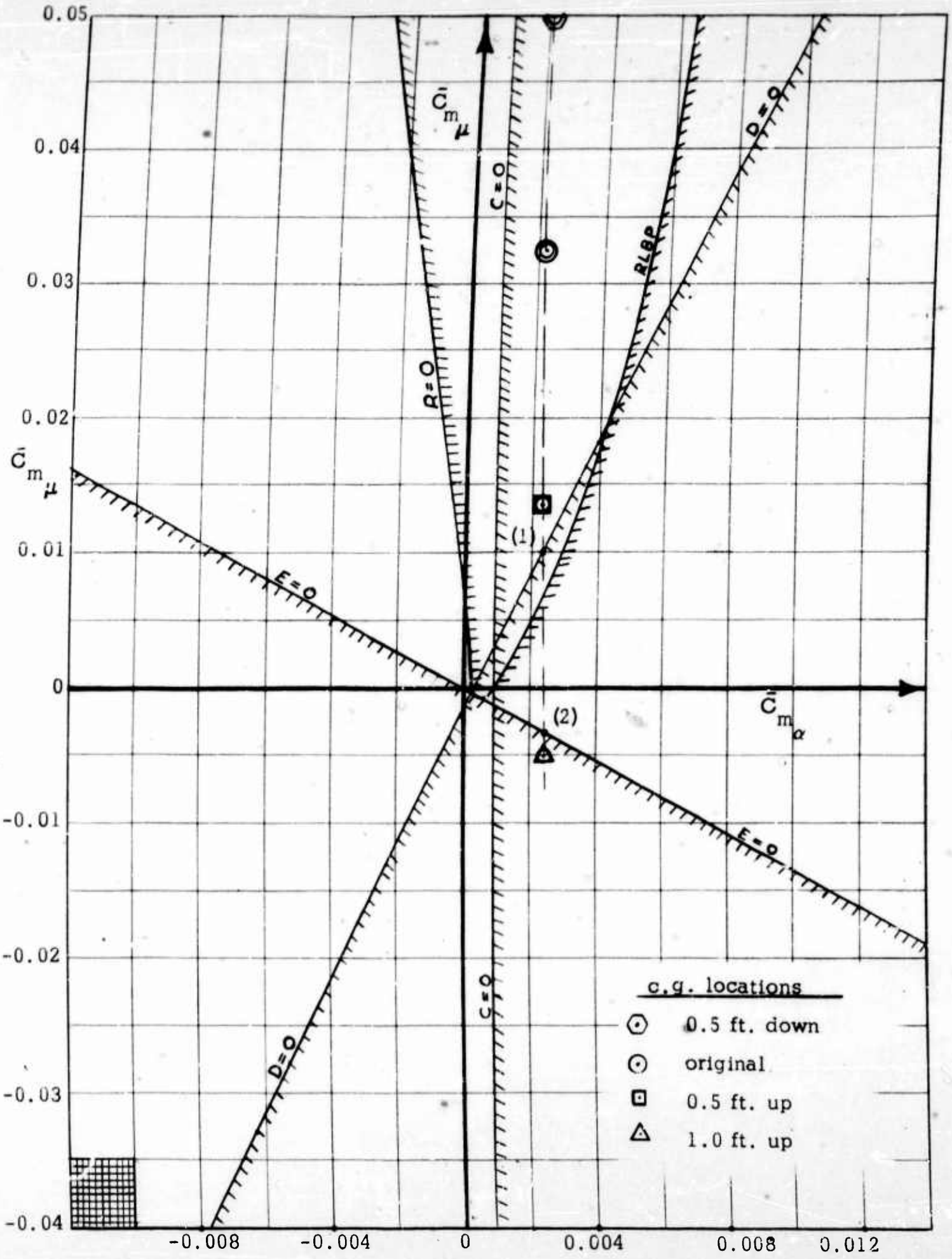

BOUNDARIES OF THE STABILITY QUARTIC L.C.D. μ = 0.05 V = 16MPH

FIGURE 10A

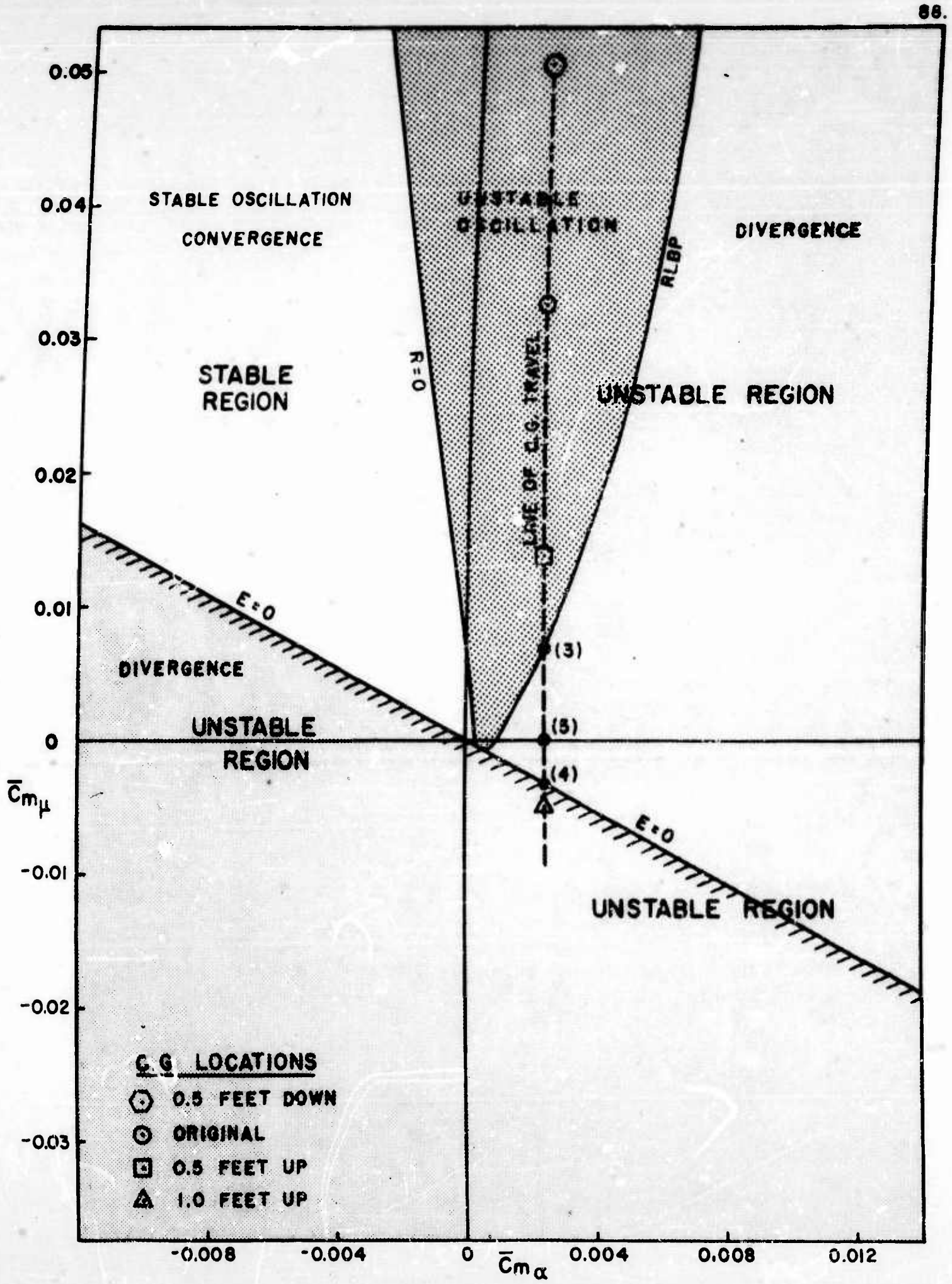

STABILITY DIAGRAM L.C.D. $\mu = 0.05$ V = 16 MPH

FIGURE 10B

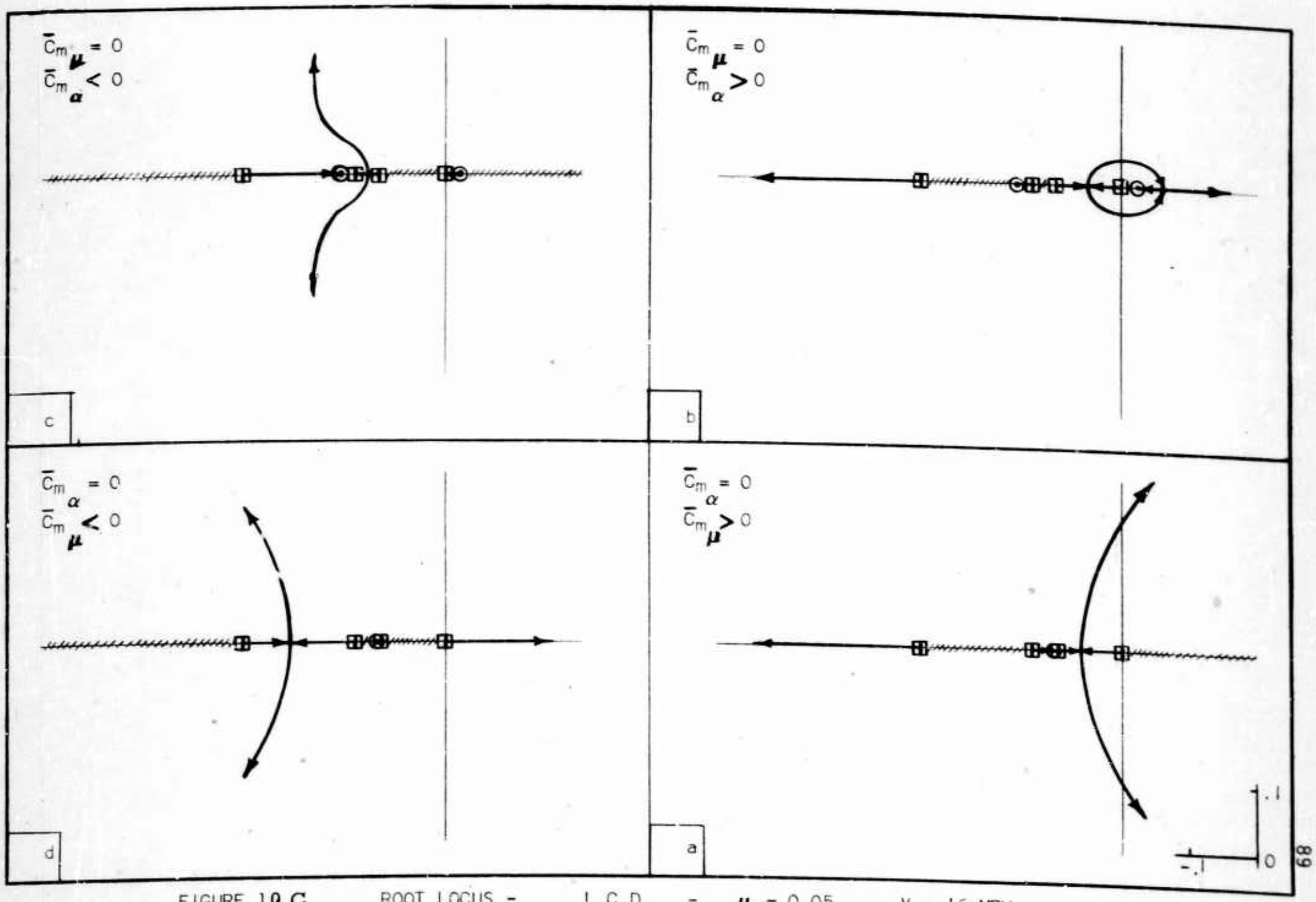

FIGURE 10 C ROOT LOCUS - L.C.D. - μ = 0.05 V = 16 MPH

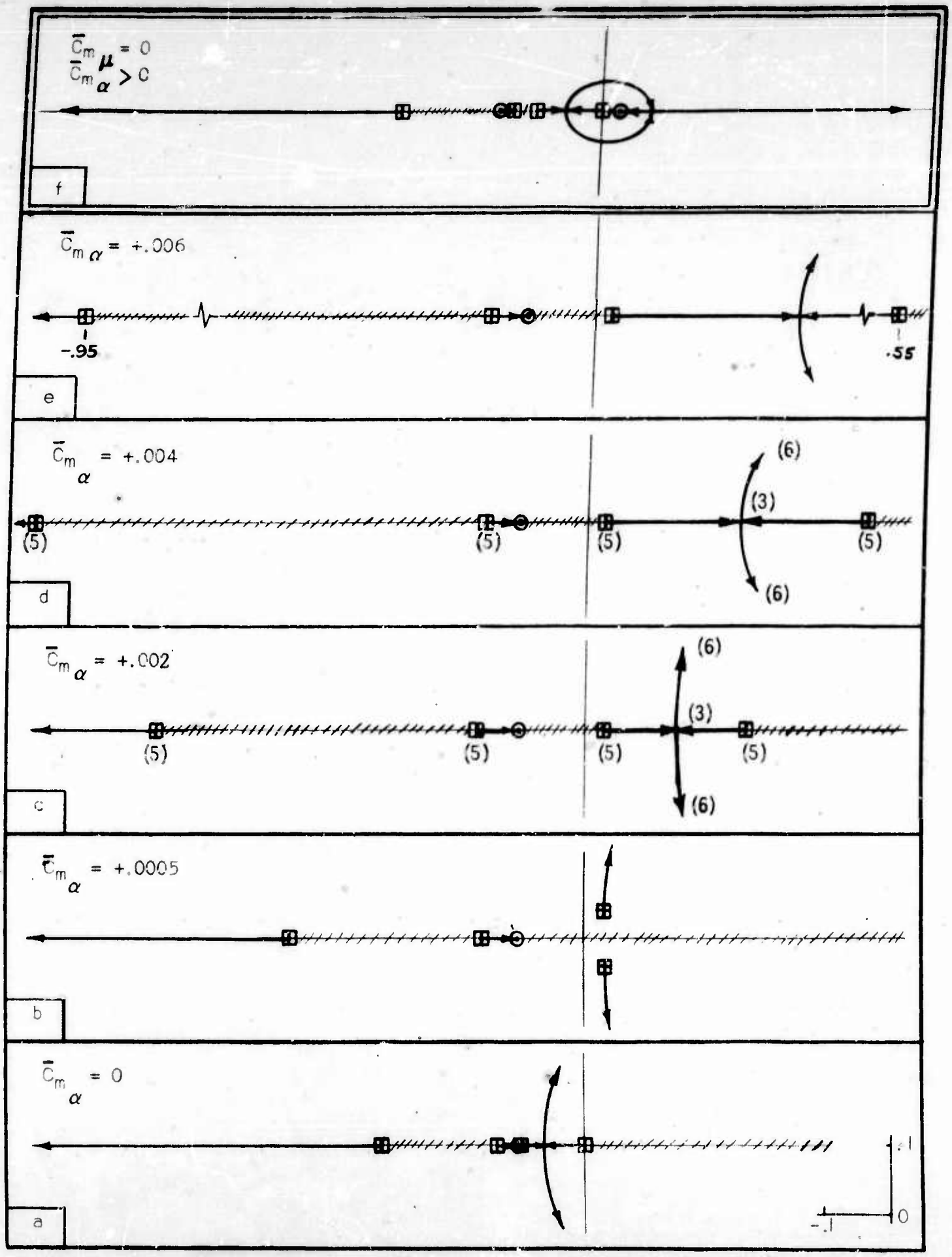

FIGURE 10 - I ROOT LOCUS L.C.D. $\mu = 0.05$ V = 16 MPH $\bar{C}_{m_\mu} > 0$

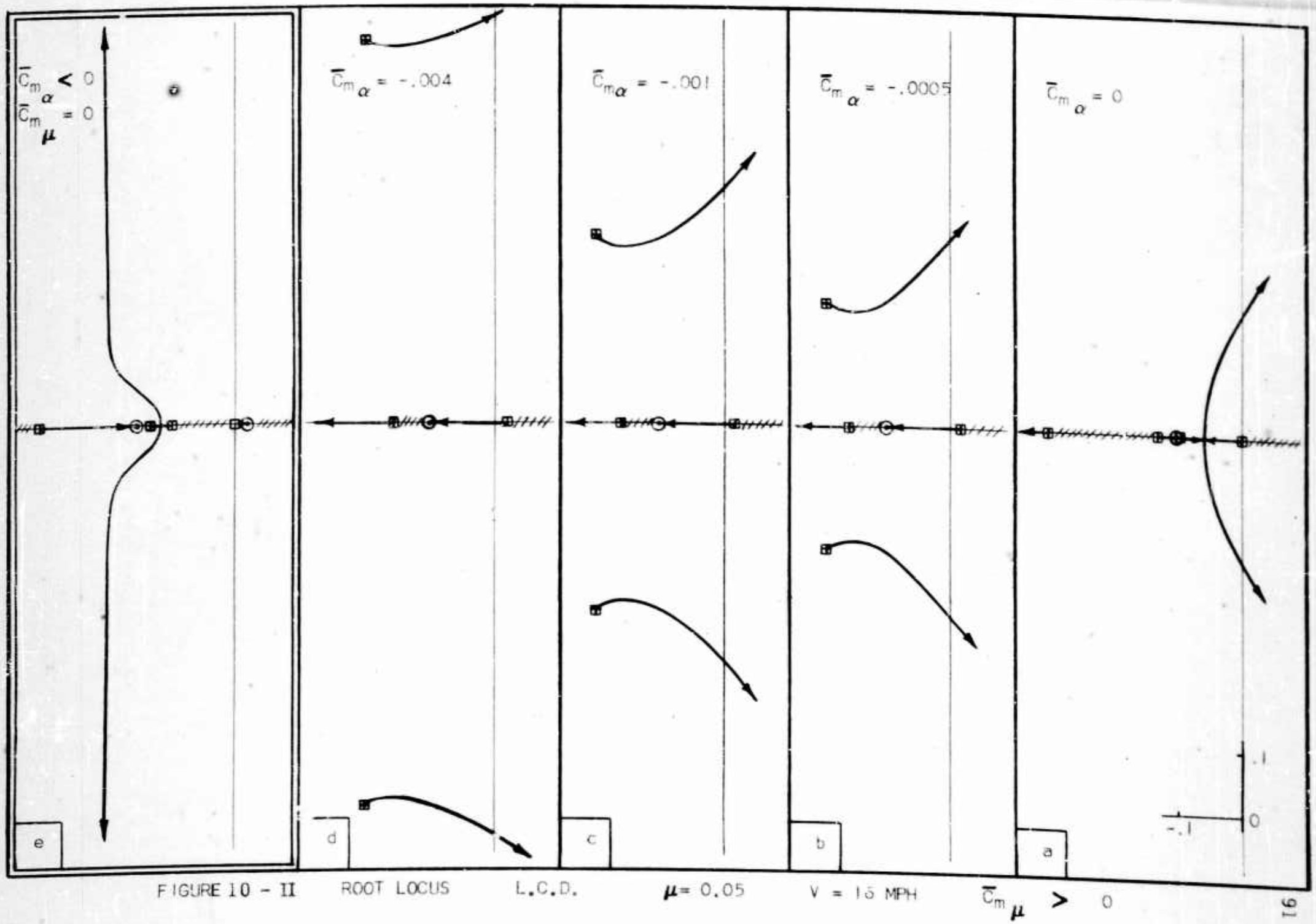

FIGURE 10 - II ROOT LOCUS L.C.D. $\mu = 0.05$ V = 15 MPH $\bar{C}_{m_\mu} > 0$

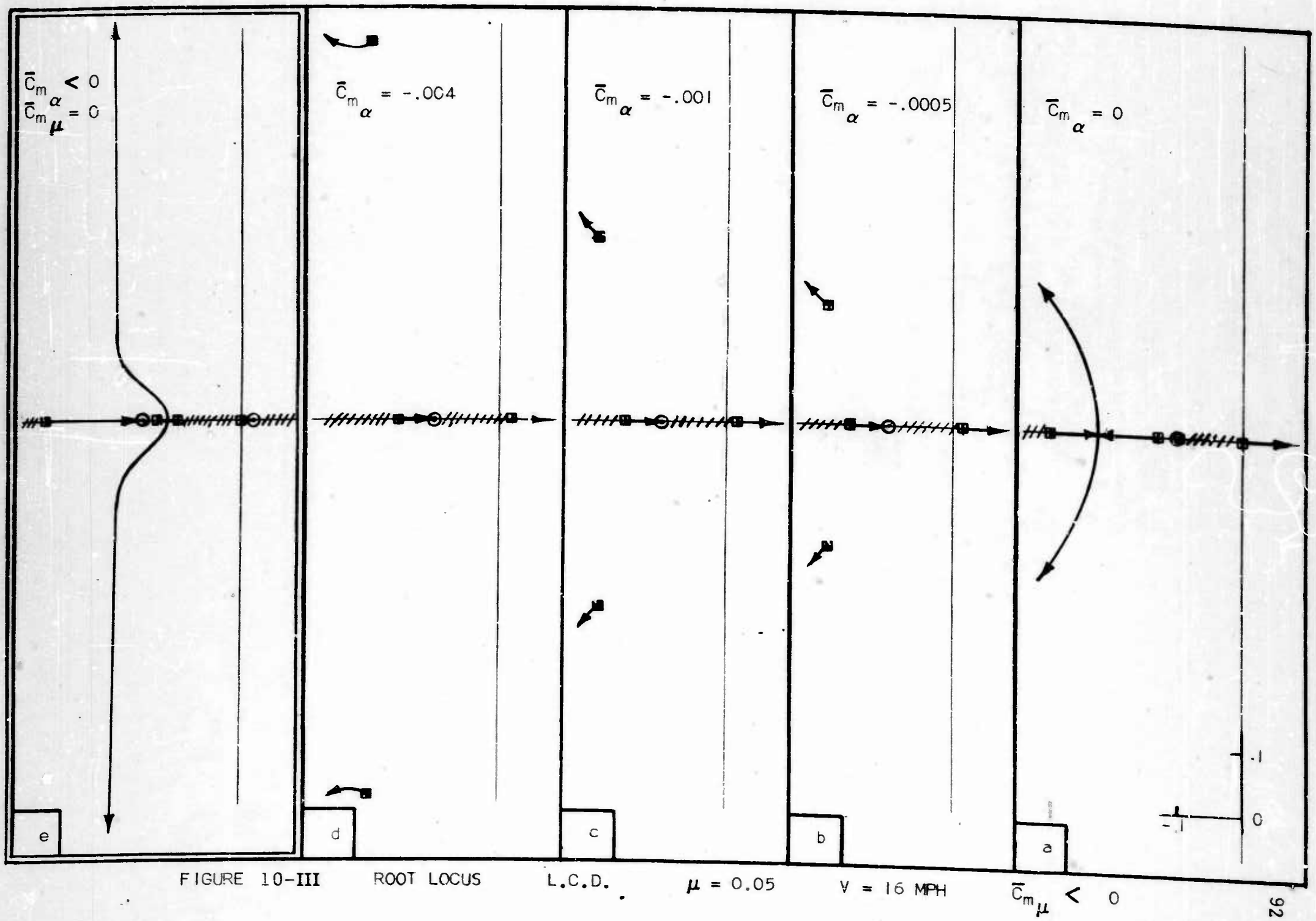

FIGURE 10-III ROOT LOCUS L.C.D. $\mu = 0.05$ V = 16 MPH $\bar{C}_{m_\mu} < 0$

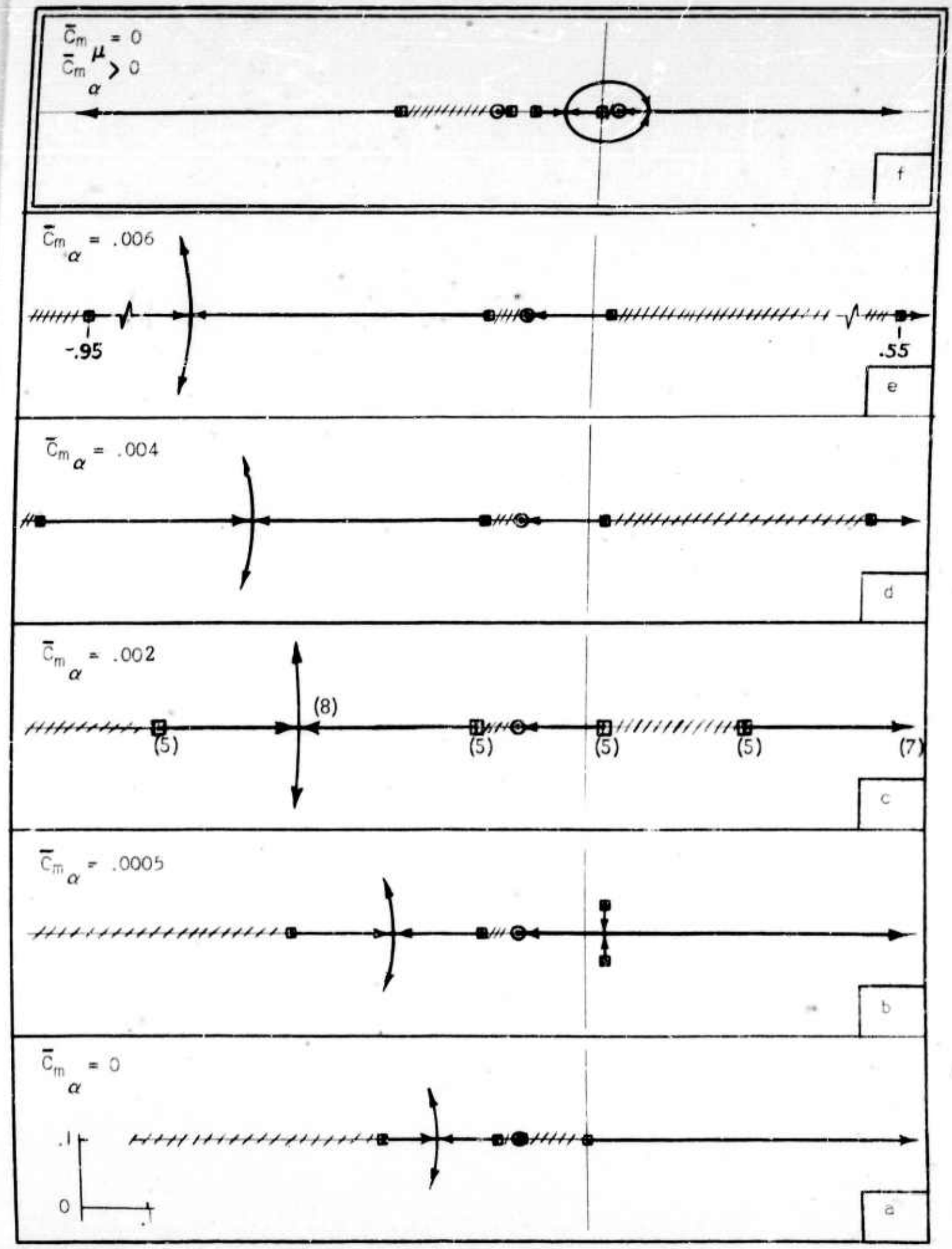

FIGURE 10 - IV ROOT LOCUS L.C.D. $\mu = 0.05$ V = 16 MPH $\bar{C}_{m_\mu} < 0$

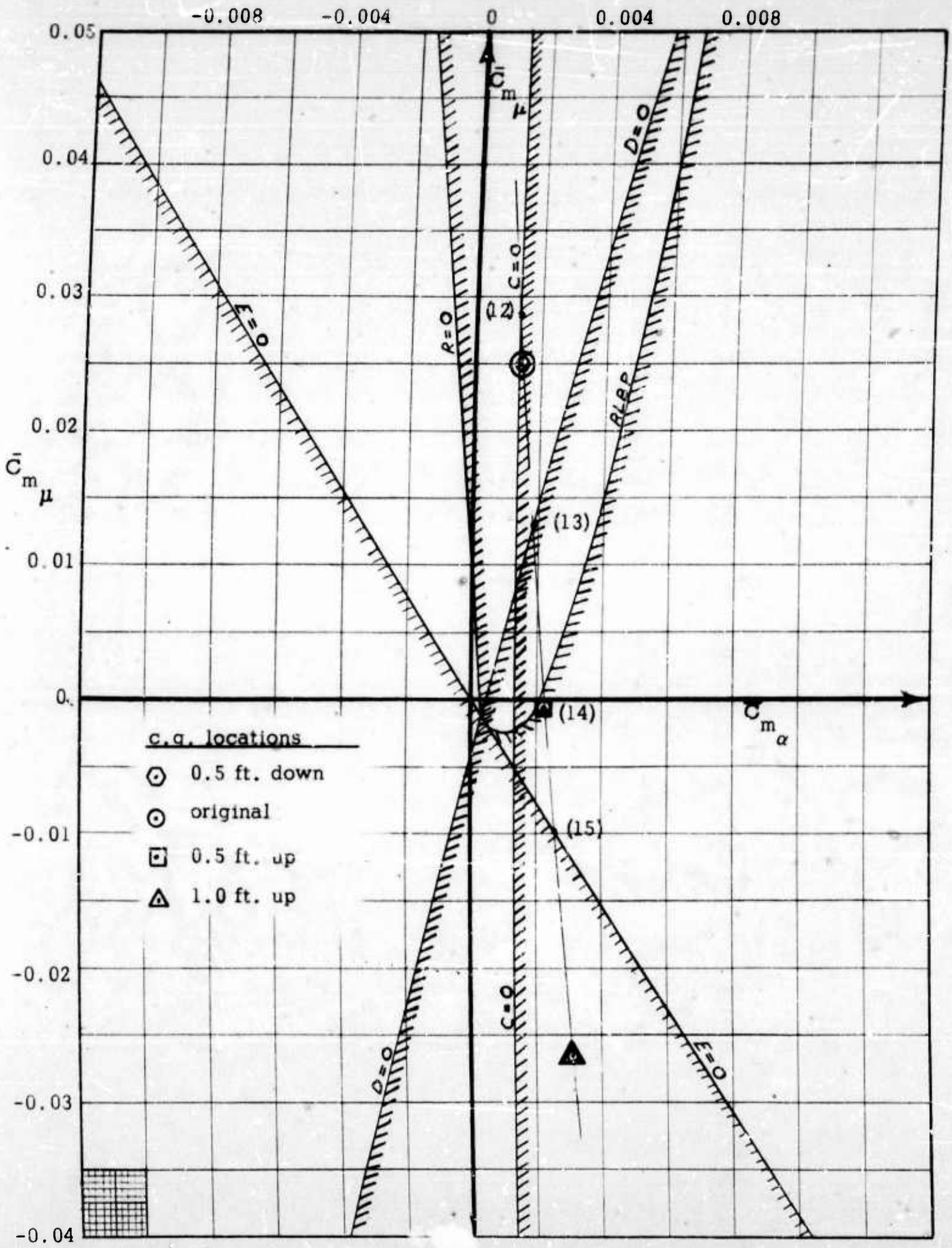

BOUNDARIES OF THE STABILITY CHARTIC L.C.D. $\mu = 0.10$ V = 34 MPH

FIGURE 11A

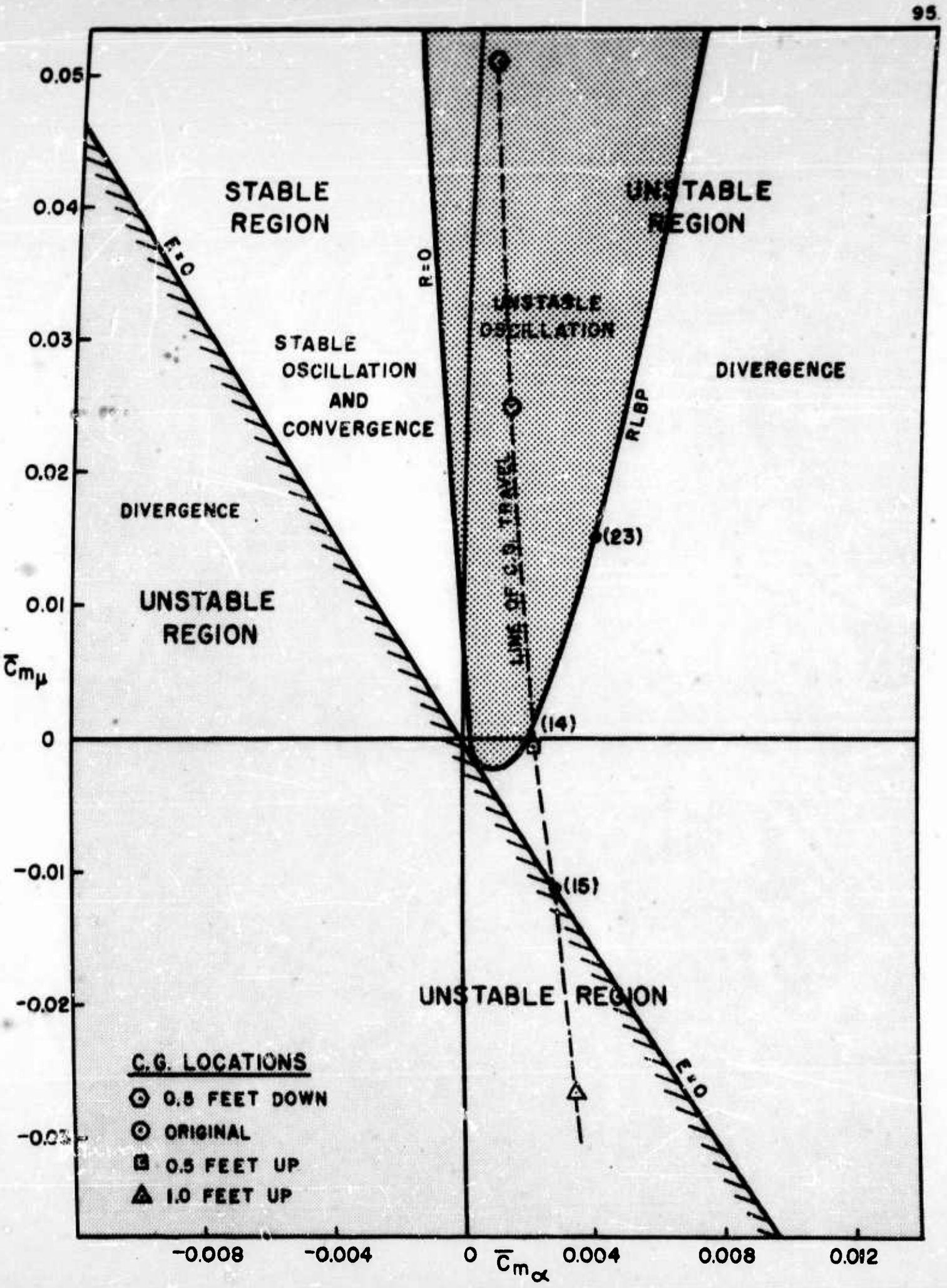

STABILITY DIAGRAM L.C.D. $\mu = 0.10$ V = 34 MPH

FIGURE 11B

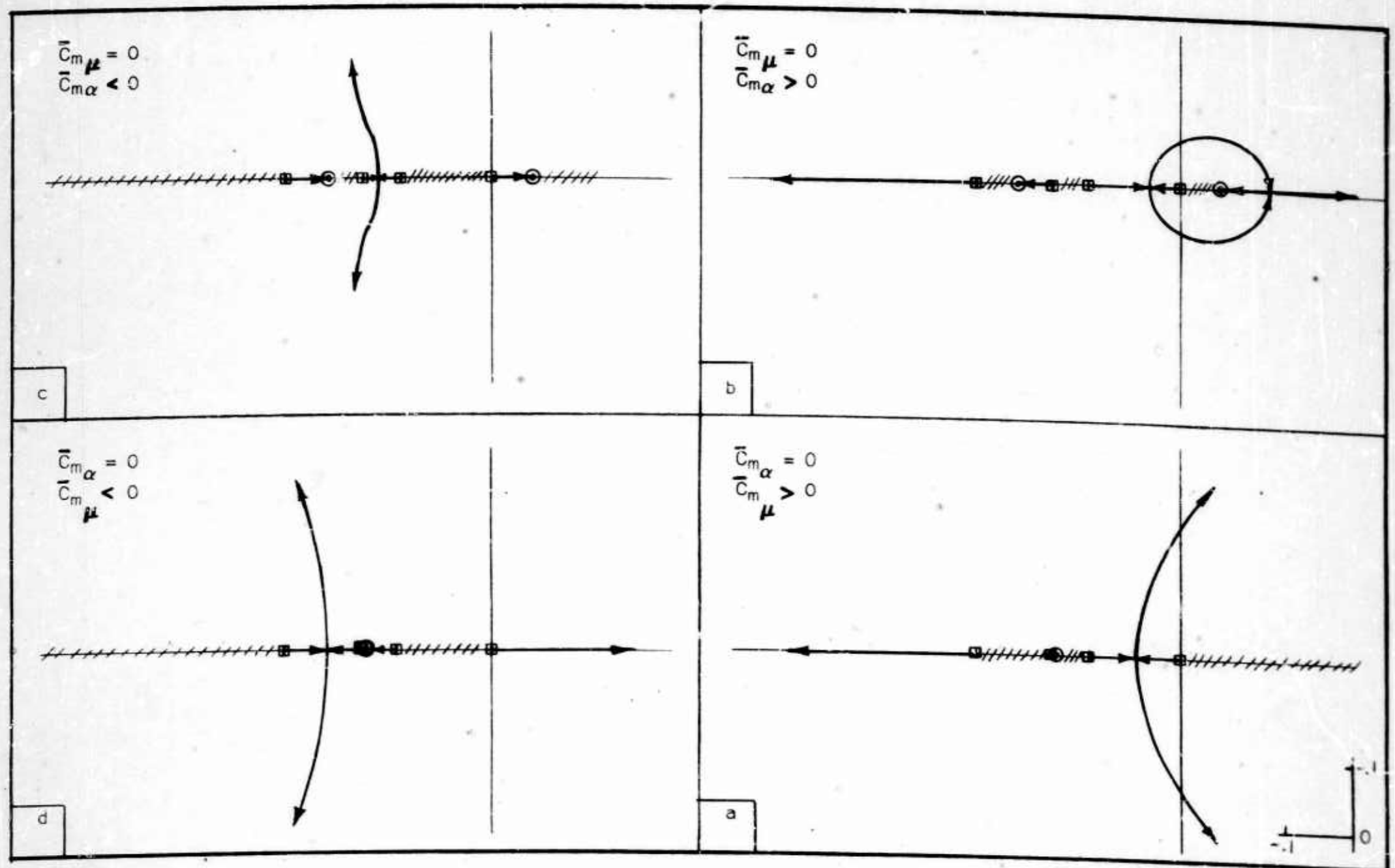

FIGURE 11C ROOT LOCUS L.C.D. $\mu = 0.10$ V = 34 MPH

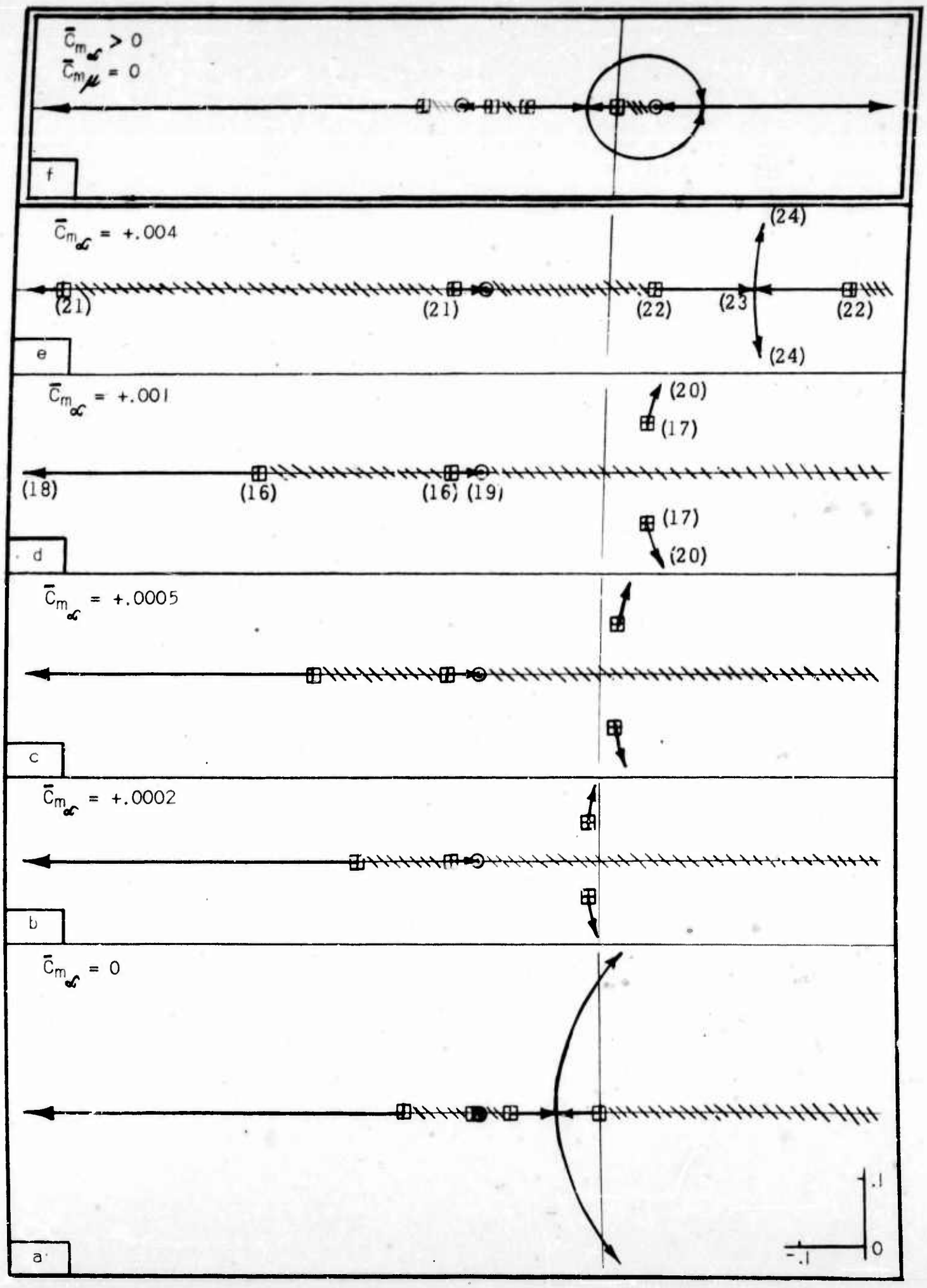

FIGURE 11 - I ROOT LOCUS L.C.D. $\mu = 0.10$ V = 34 MPH $\bar{C}_{m_\mu} > 0$

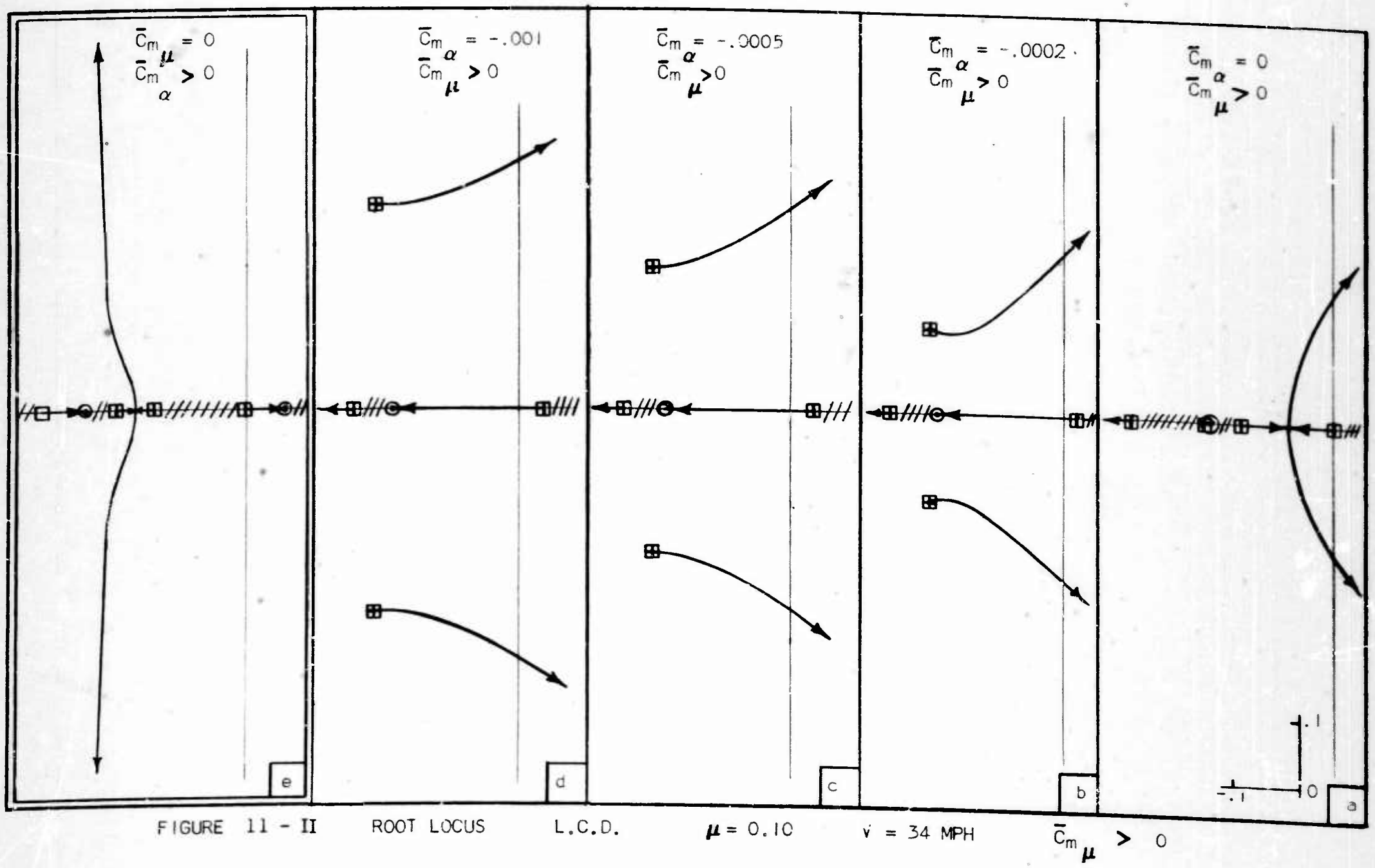

FIGURE 11 - II ROOT LOCUS L.C.D. $\mu = 0.10$ V = 34 MPH $\bar{C}_{m_\mu} > 0$

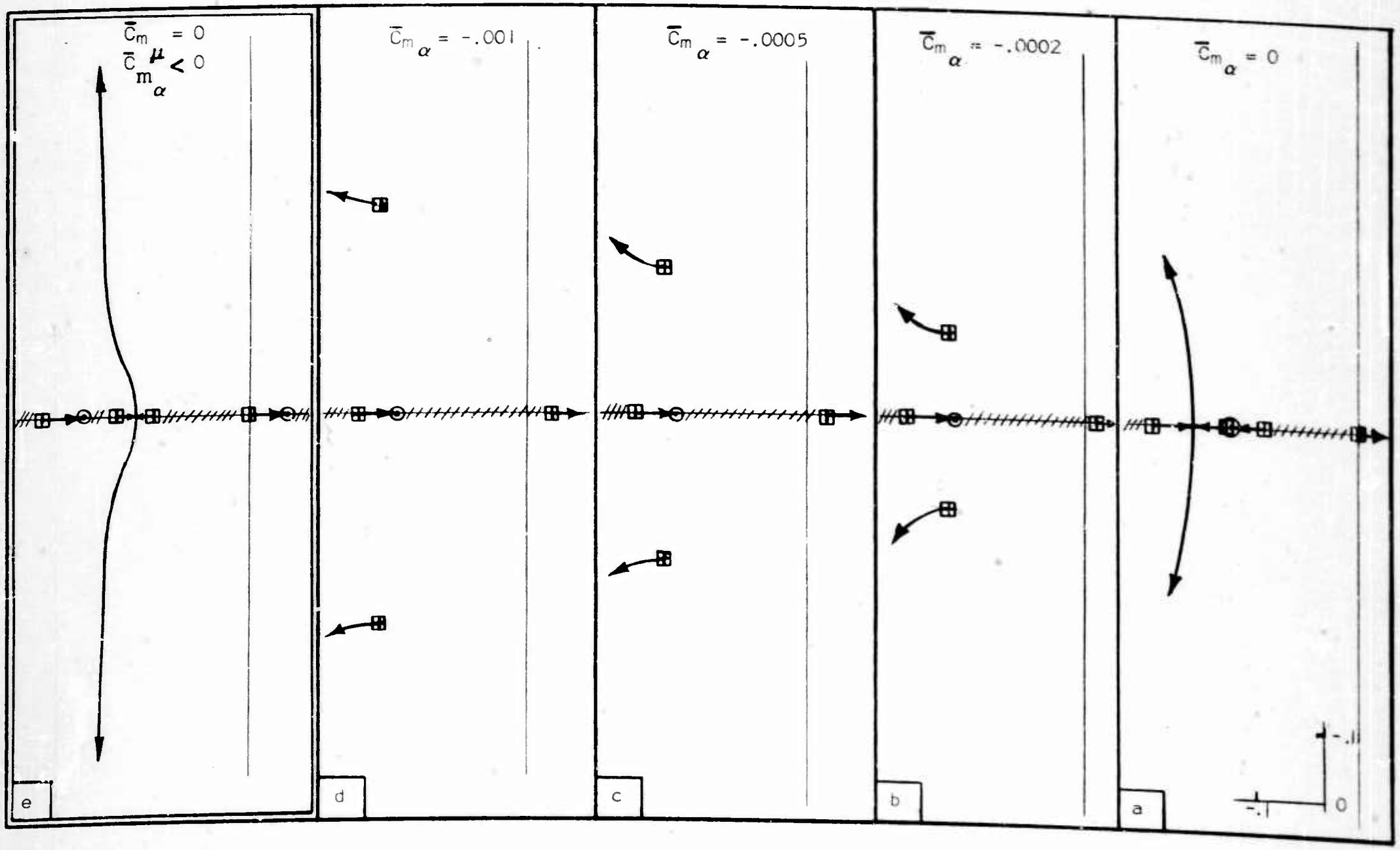

FIGURE 11 - III ROOT LOCUS L.C.D. $\mu = 0.10$ V = 34 MPH $\bar{C}_{m_\mu} < 0$

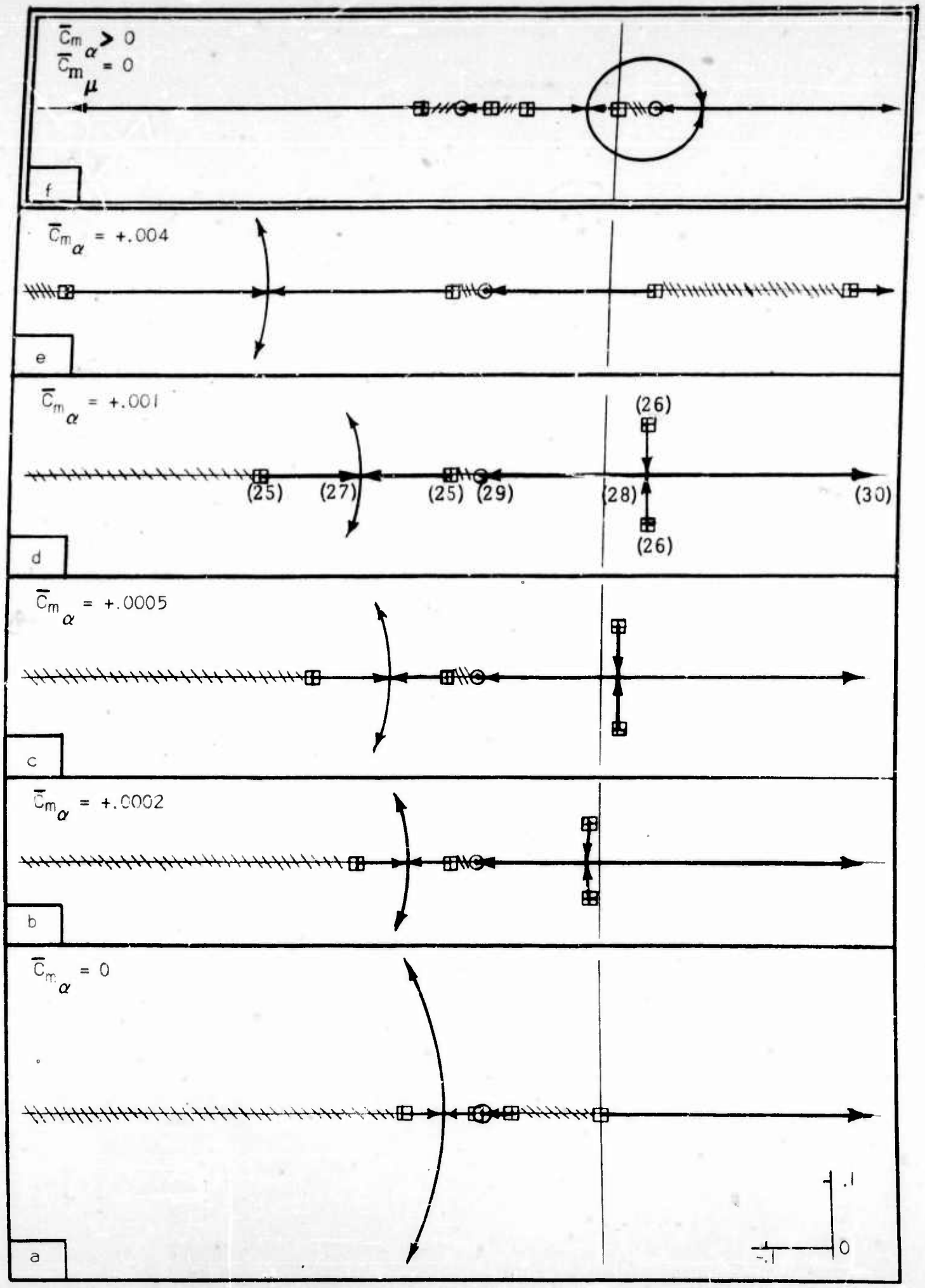

FIGURE 11 - IV ROOT LOCUS L.C.D. $\mu = 0.10$ V = 34 MPH $\bar{C}_{m_\mu} < 0$

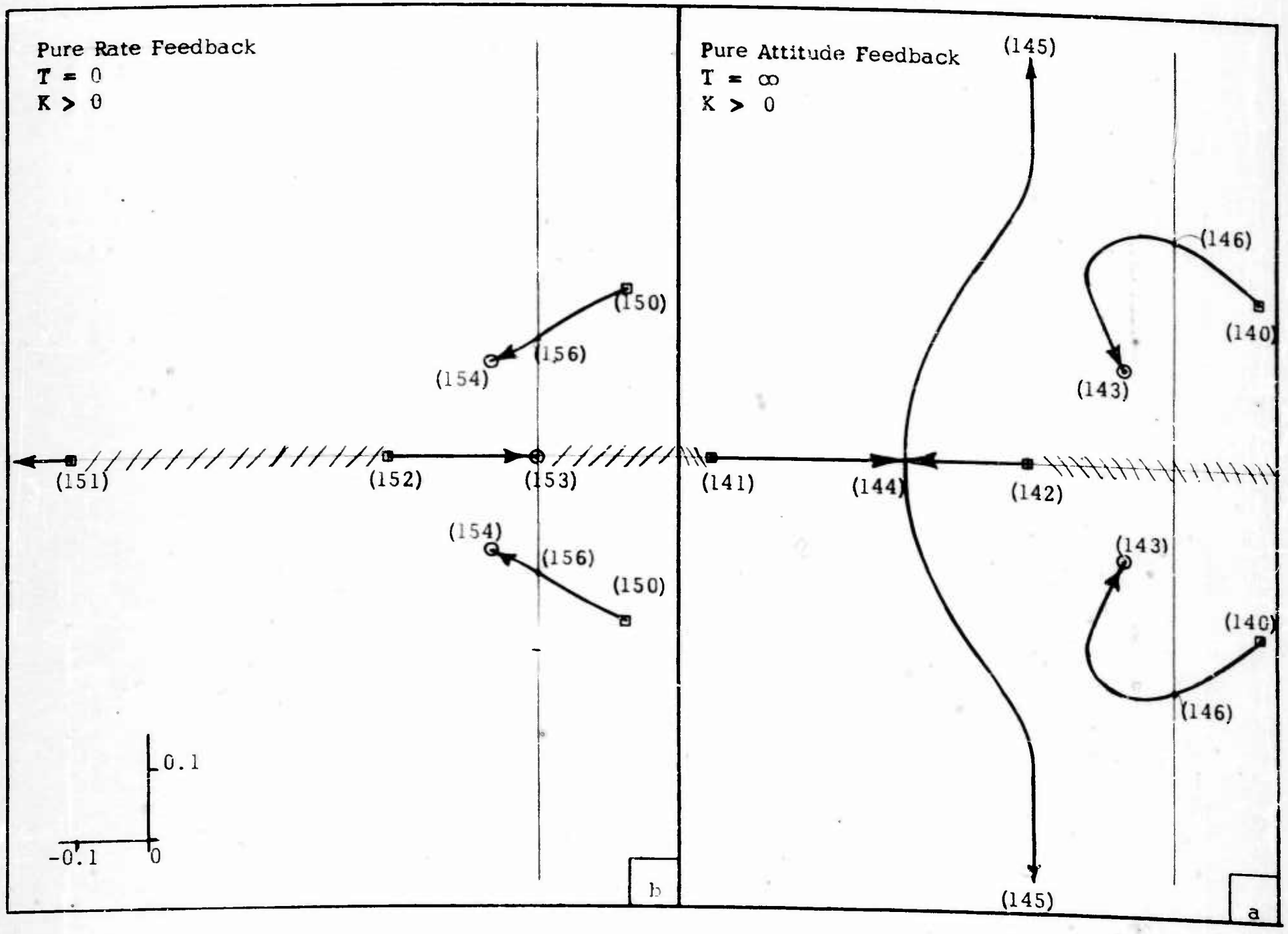

FIGURE 12 ROOT LOCUS L.C.D. μ = 0.10 V = 34 MPH ARTIFICIAL STABILIZATION ADDED

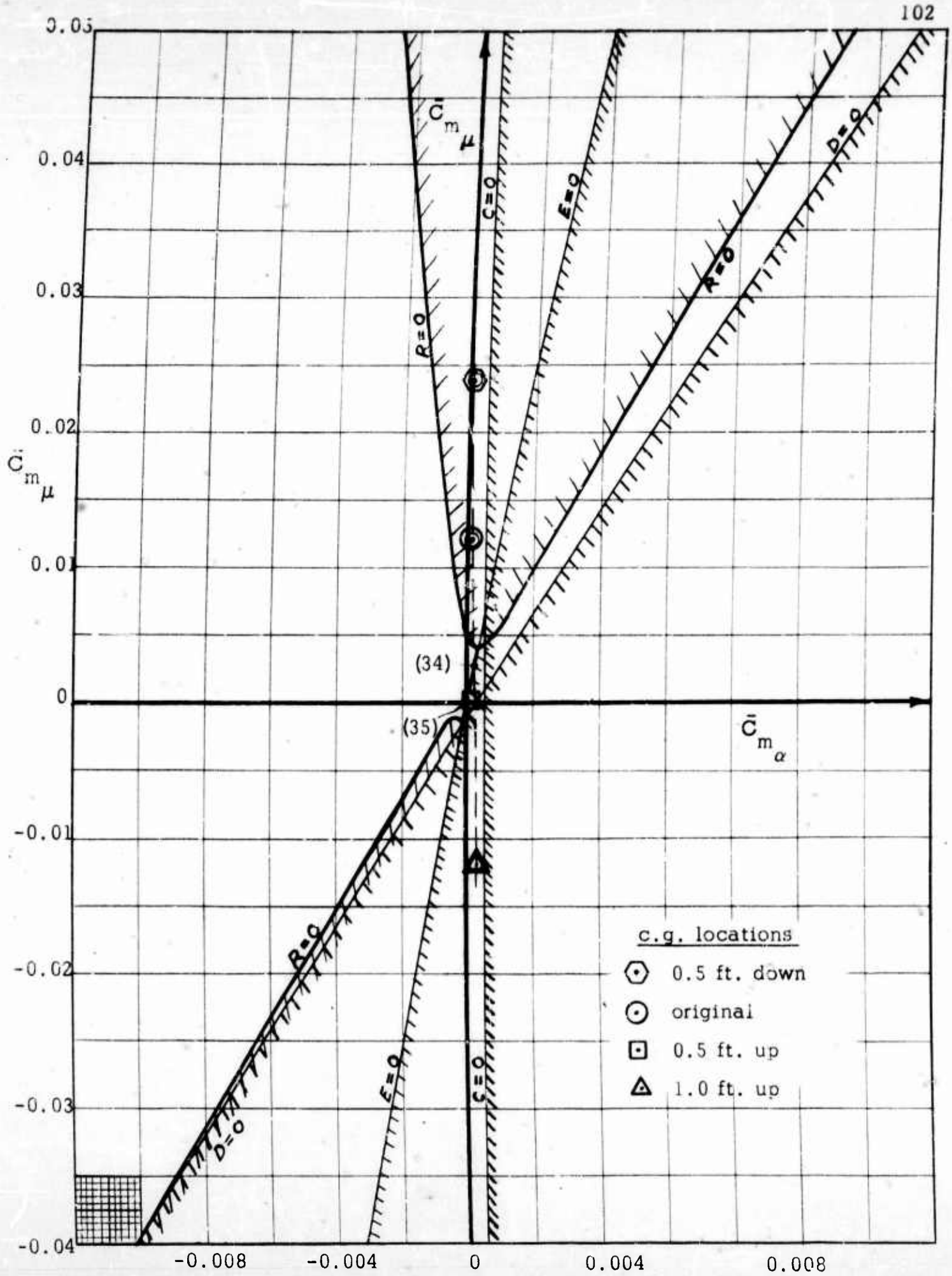

BOUNDARIES OF THE STABILITY QUARTIC S.C.D. $\mu = 0.05$ V = 18 MPH

FIGURE 13A

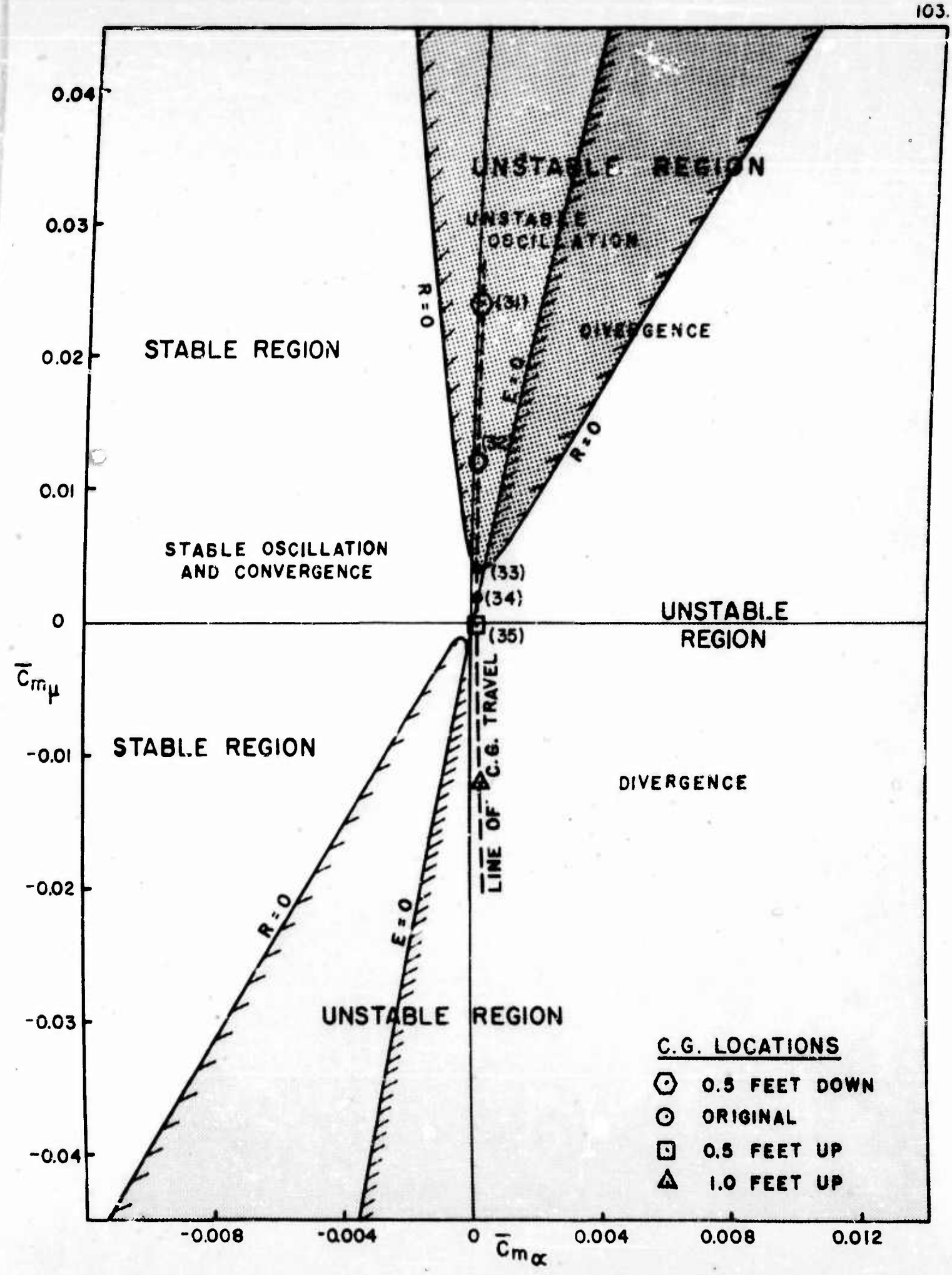

STABILITY DIAGRAM S.C.D. $\mu = 0.05$ V = 18 MPH

FIGURE 13B

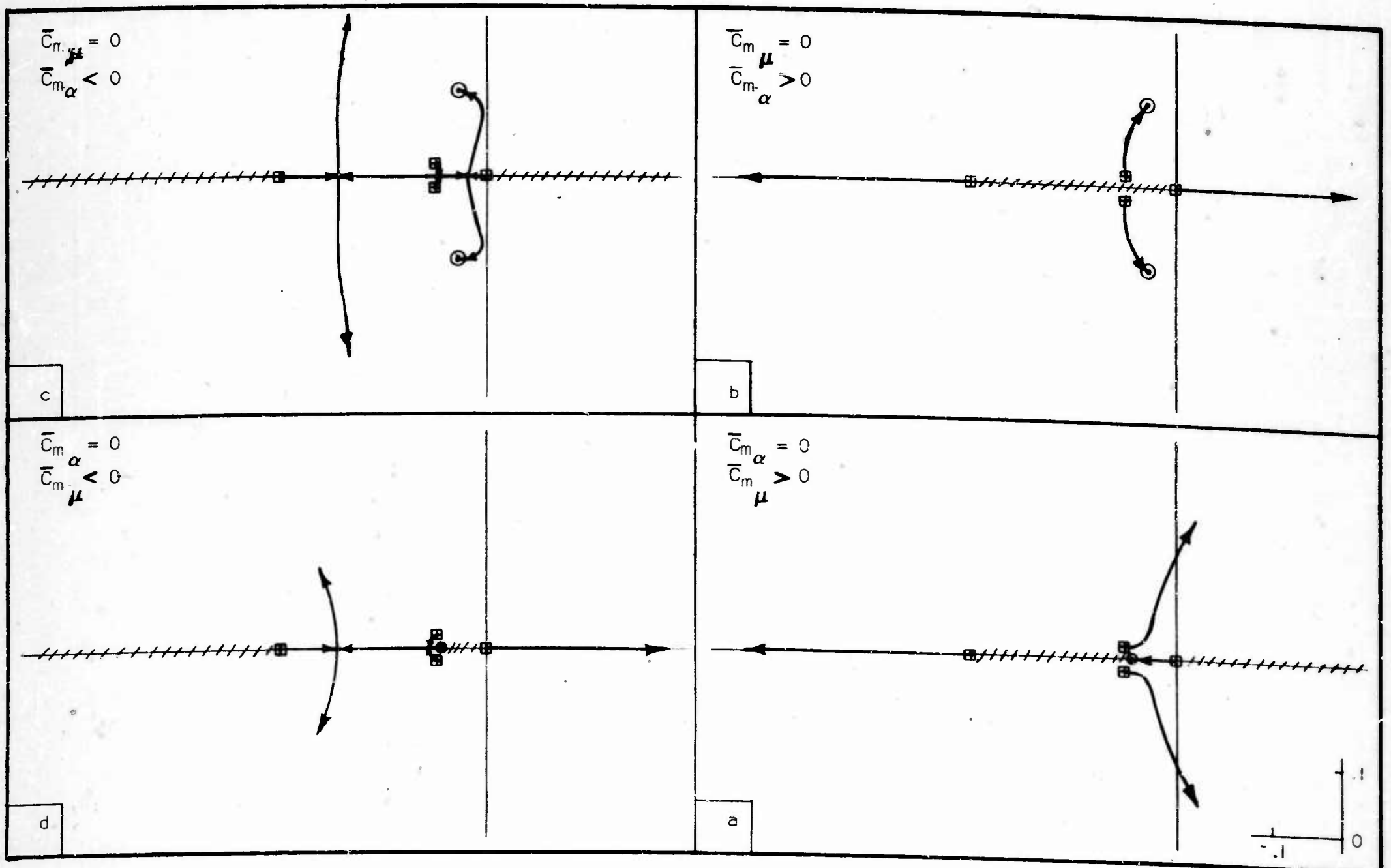

FIGURE 13 C ROOT LOCUS S.C.D. $\mu = 0.05$ V = 18 MPH

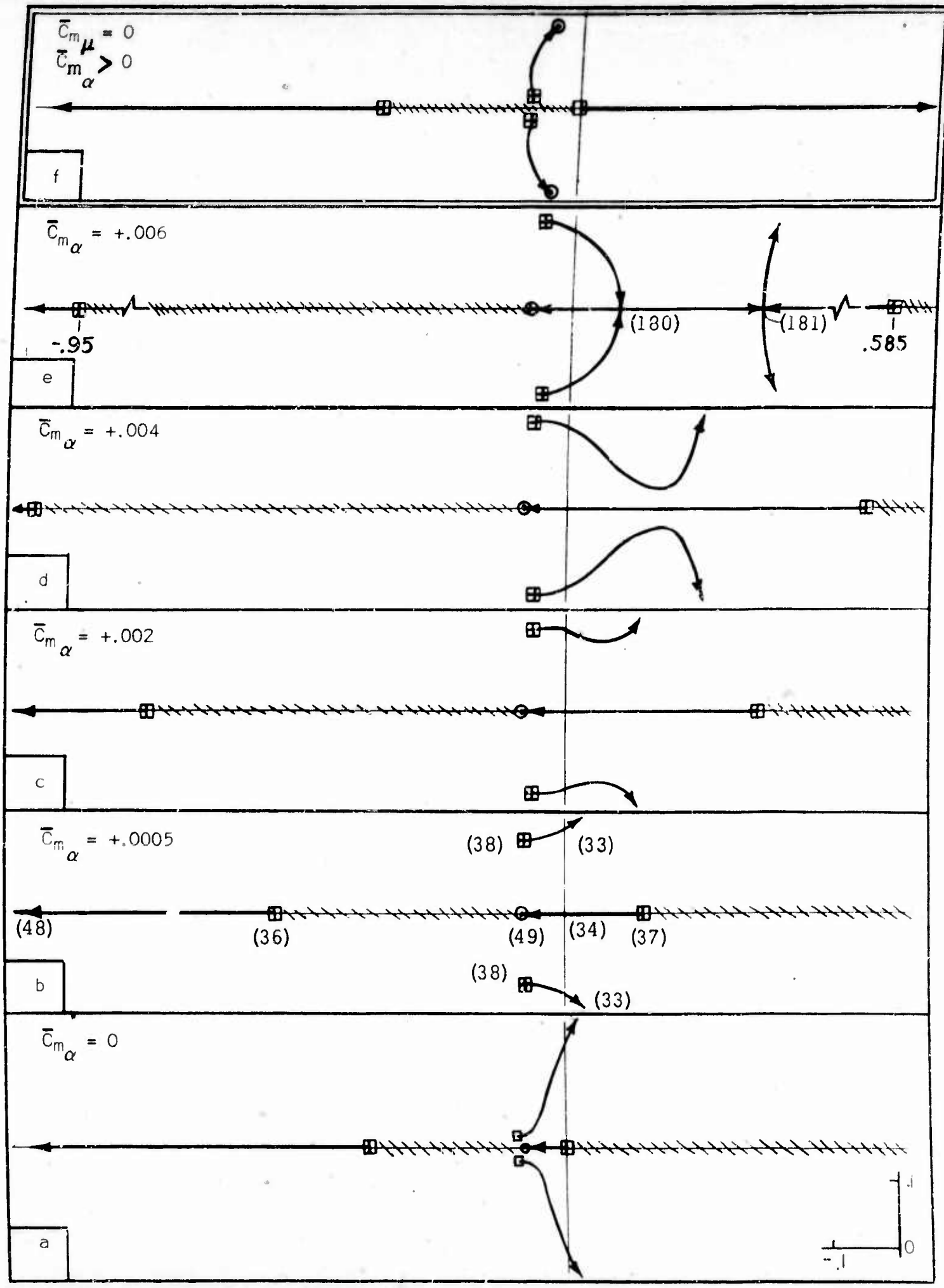

FIGURE 13 - I ROOT LOCUS S.C.D. $\mu_1 = 0.05$ V = 18MPH $\bar{C}_{m_\mu} > 0$

AD

227158

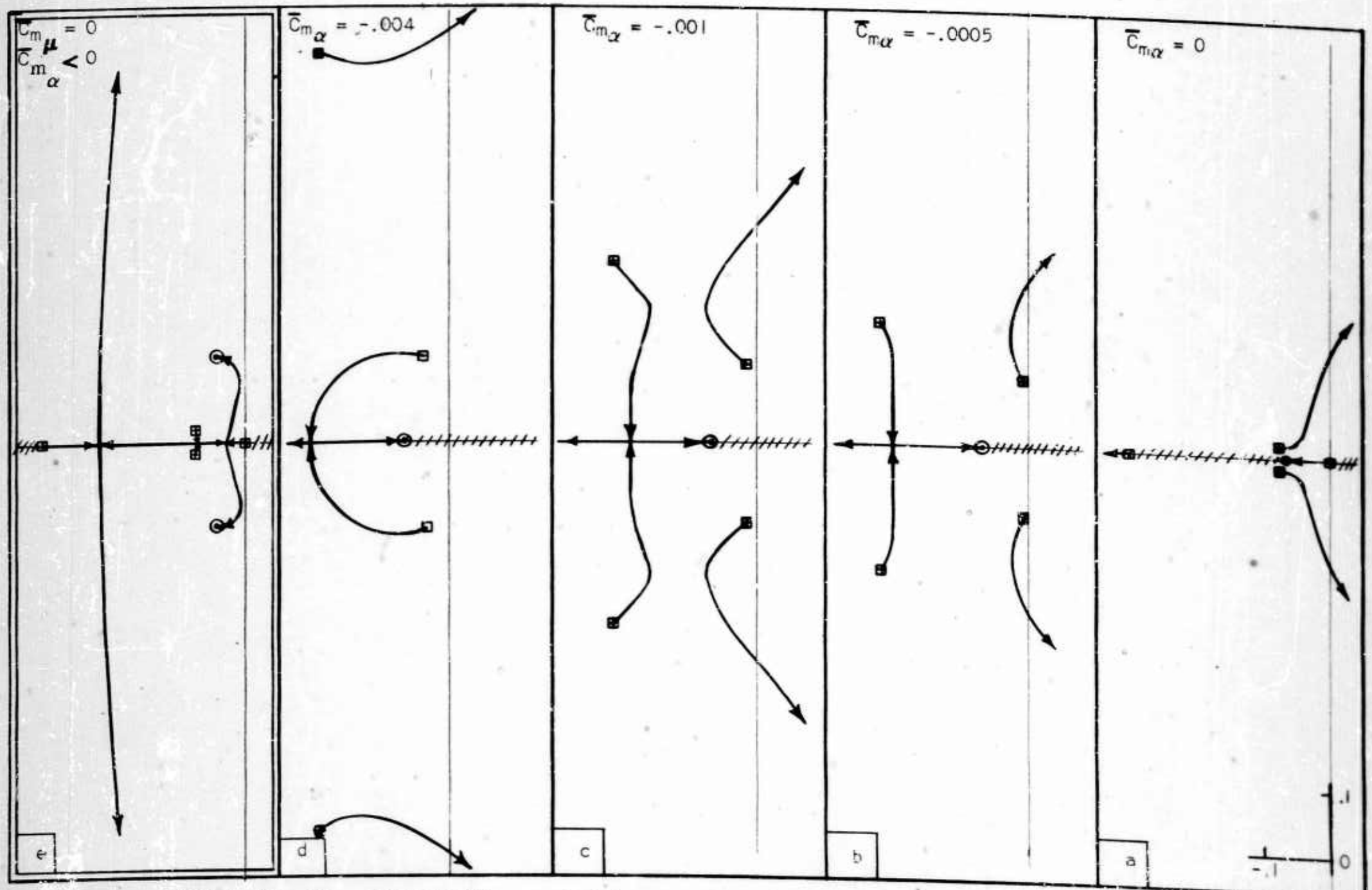

FIGURE 13 - II ROOT LOCUS S.C.D. $\mu = 0.05$ V = 18 MPH $\bar{C}_{m_\mu} > 0$

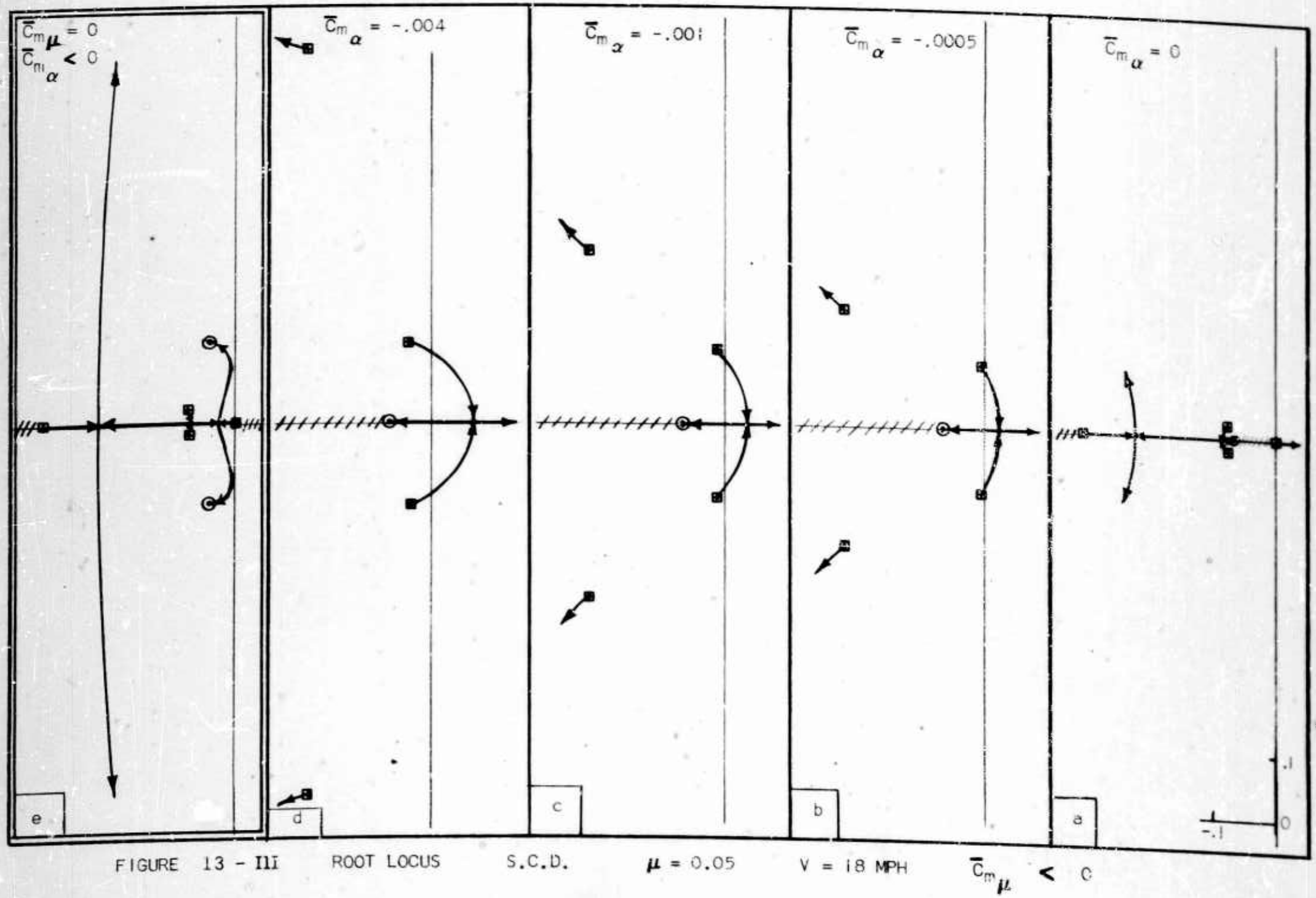

FIGURE 13 - III ROOT LOCUS S.C.D. $\mu = 0.05$ V = 18 MPH $\overline{C}_{m_\mu} < 0$

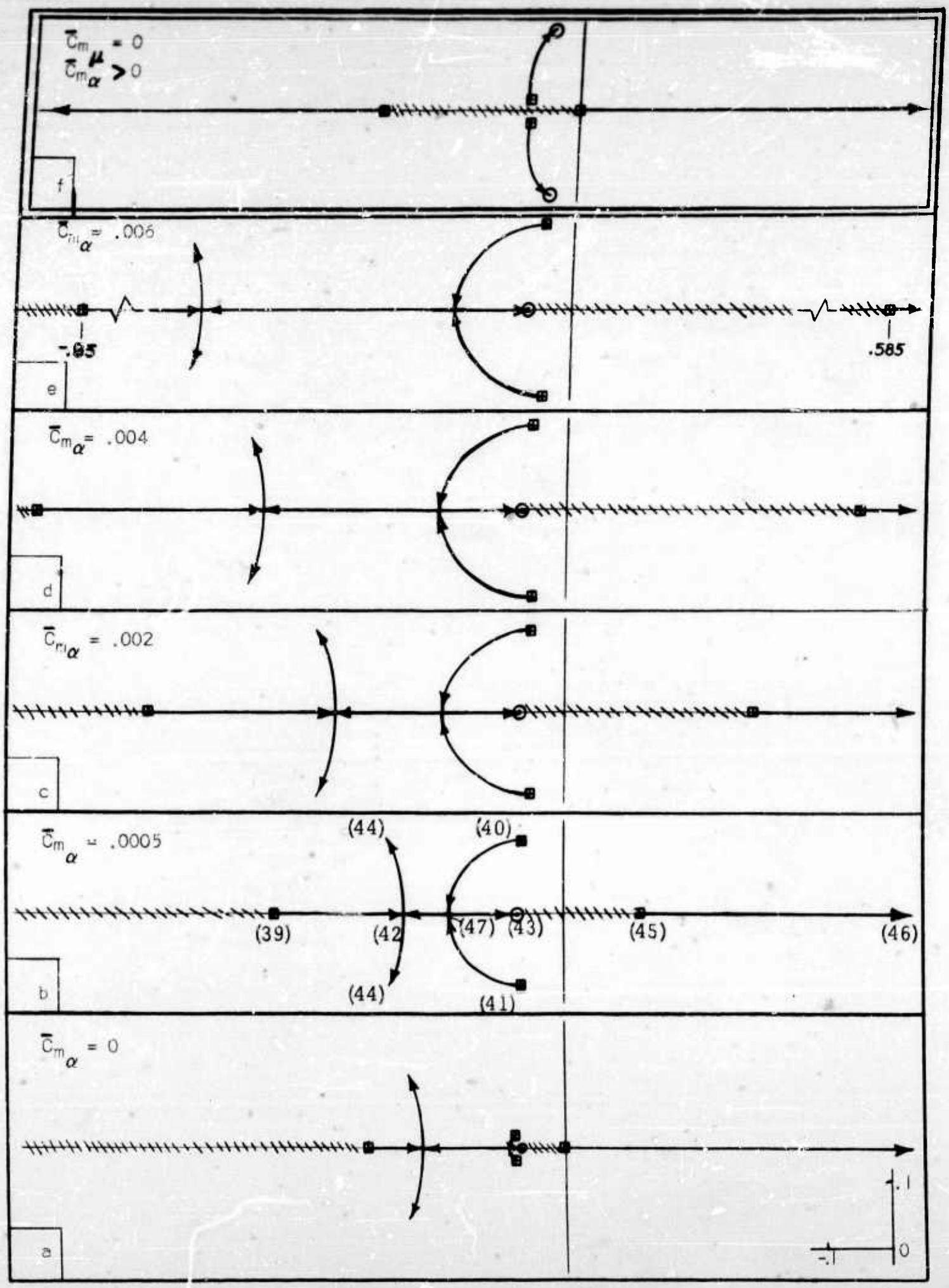

FIGURE 13 - IV ROOT LOCUS S.C.D. $\mu = 0.05$ V = 18 MPH $\bar{C}_{m_\mu} < 0$

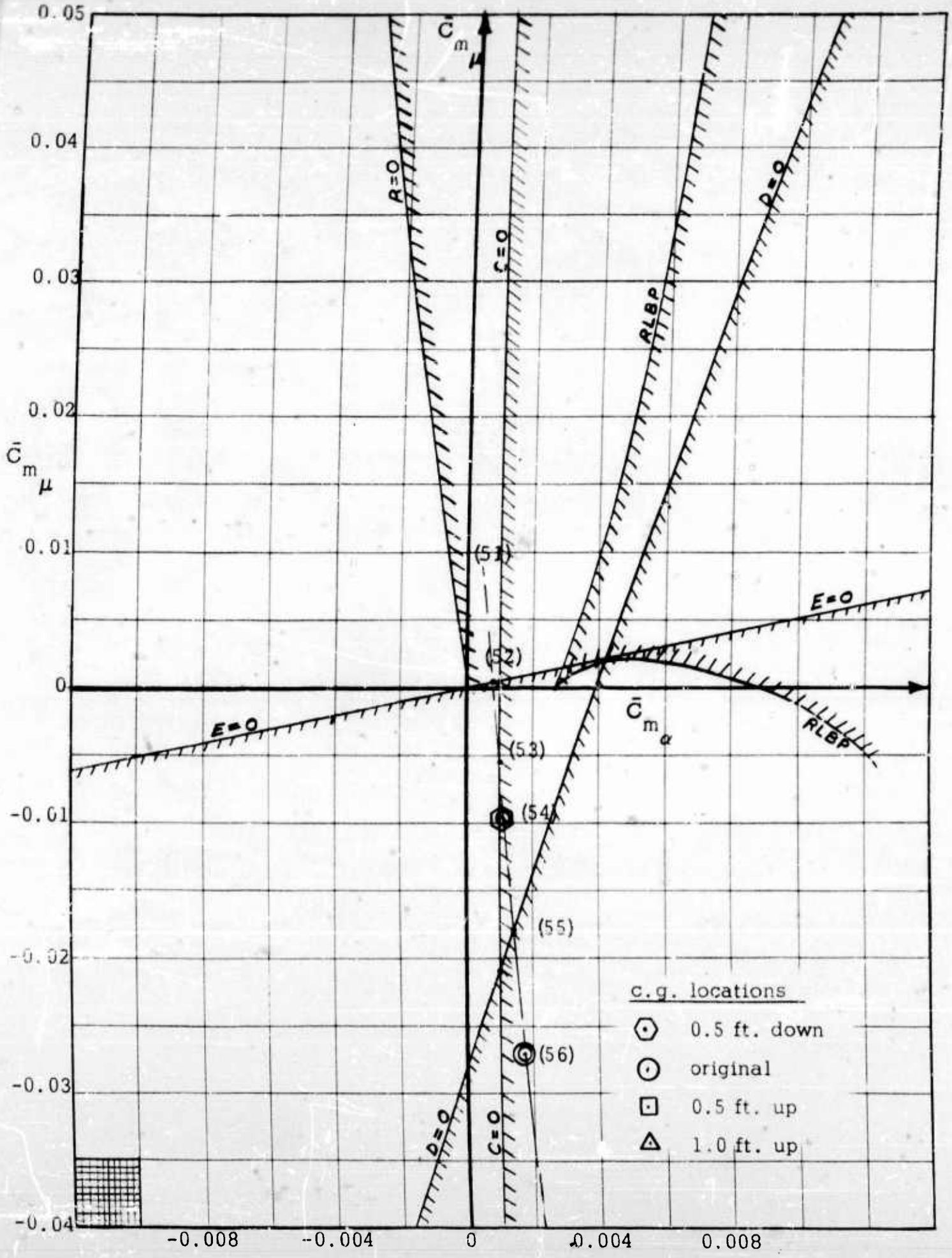

BOUNDARIES OF THE STABILITY QUARTIC S.C.D. μ = 0.10 V = 36 MPH

FIGURE 14A

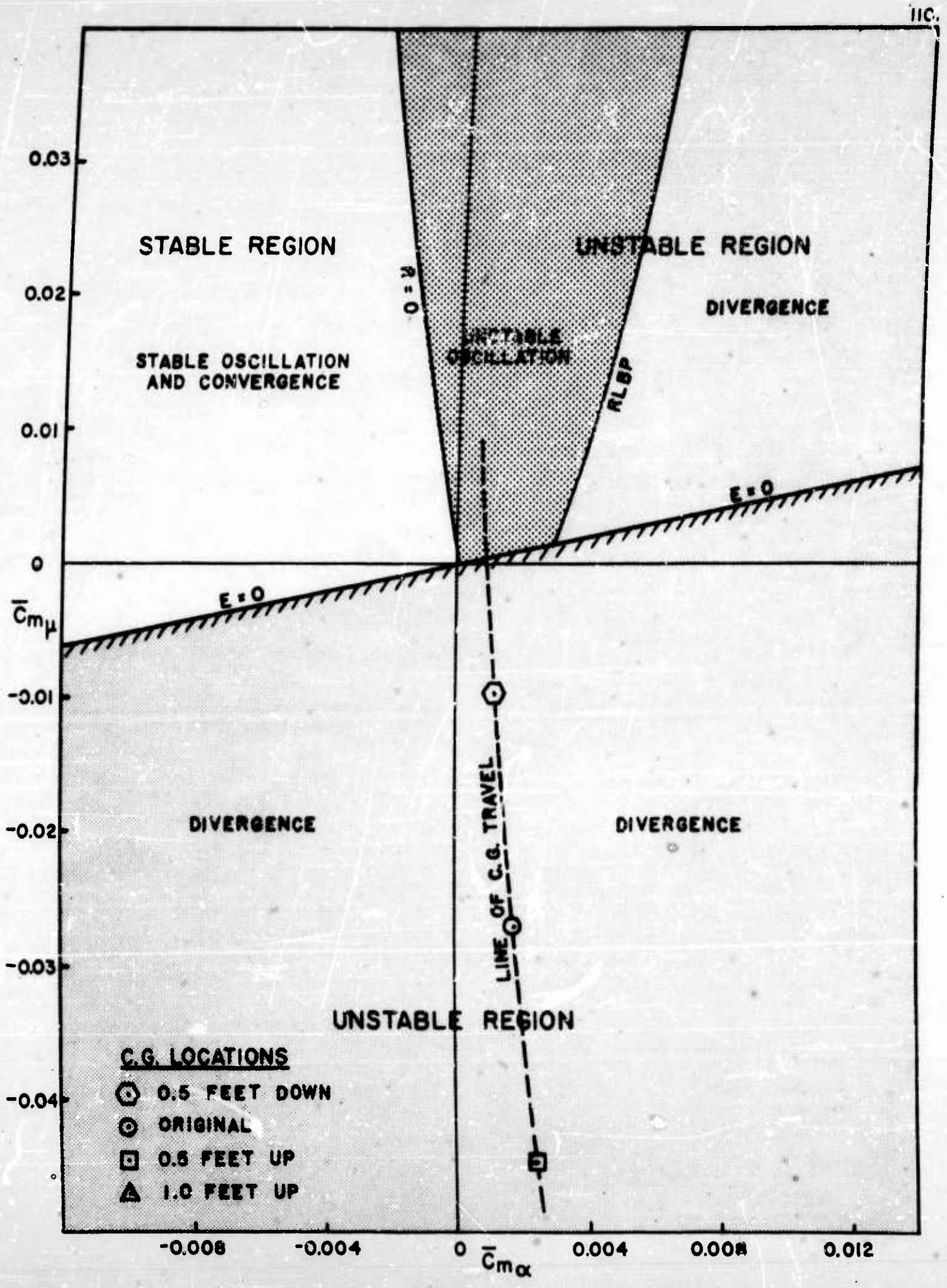

STABILITY DIAGRAM S.C.D. $\mu = 0.10$ V = 36 MPH

FIGURE 14B

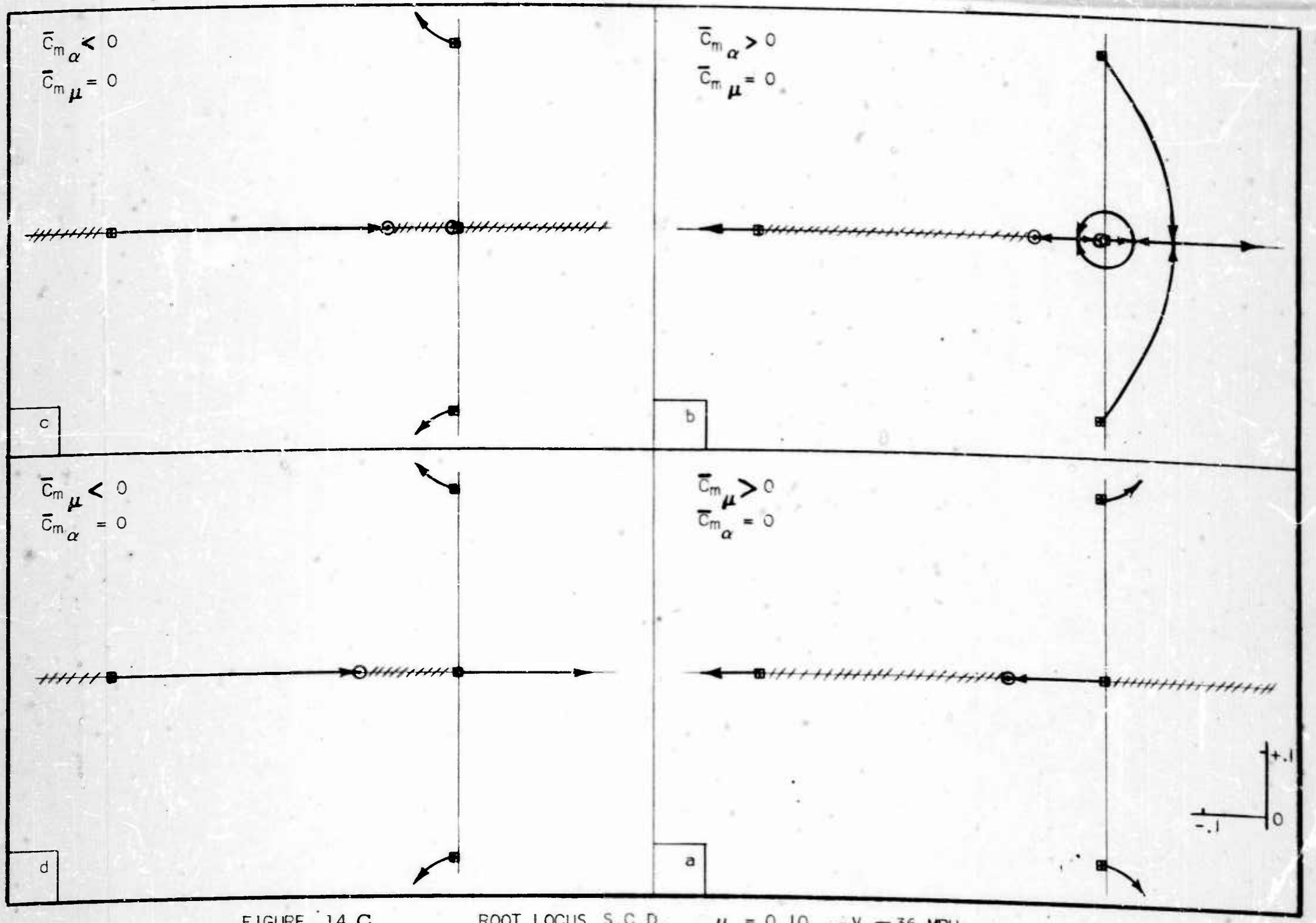

FIGURE 14 C ROOT LOCUS S.C.D. $\mu = 0.10$ V = 36 MPH

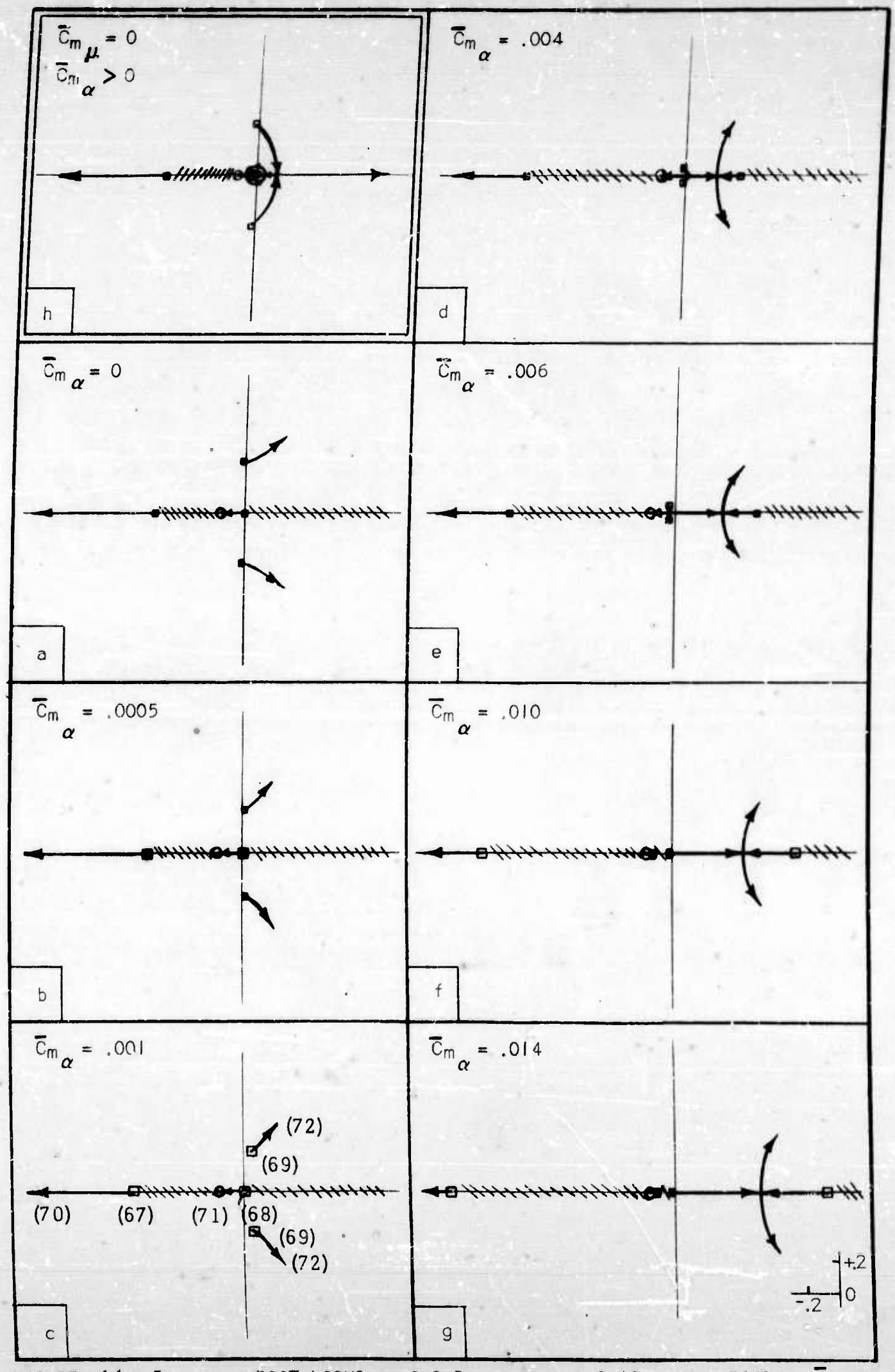

FIGURE 14 - I ROOT LOCUS S.C.D. $\mu = 0.10$ V = 36MPH $\bar{C}_{m_\mu} > 0$

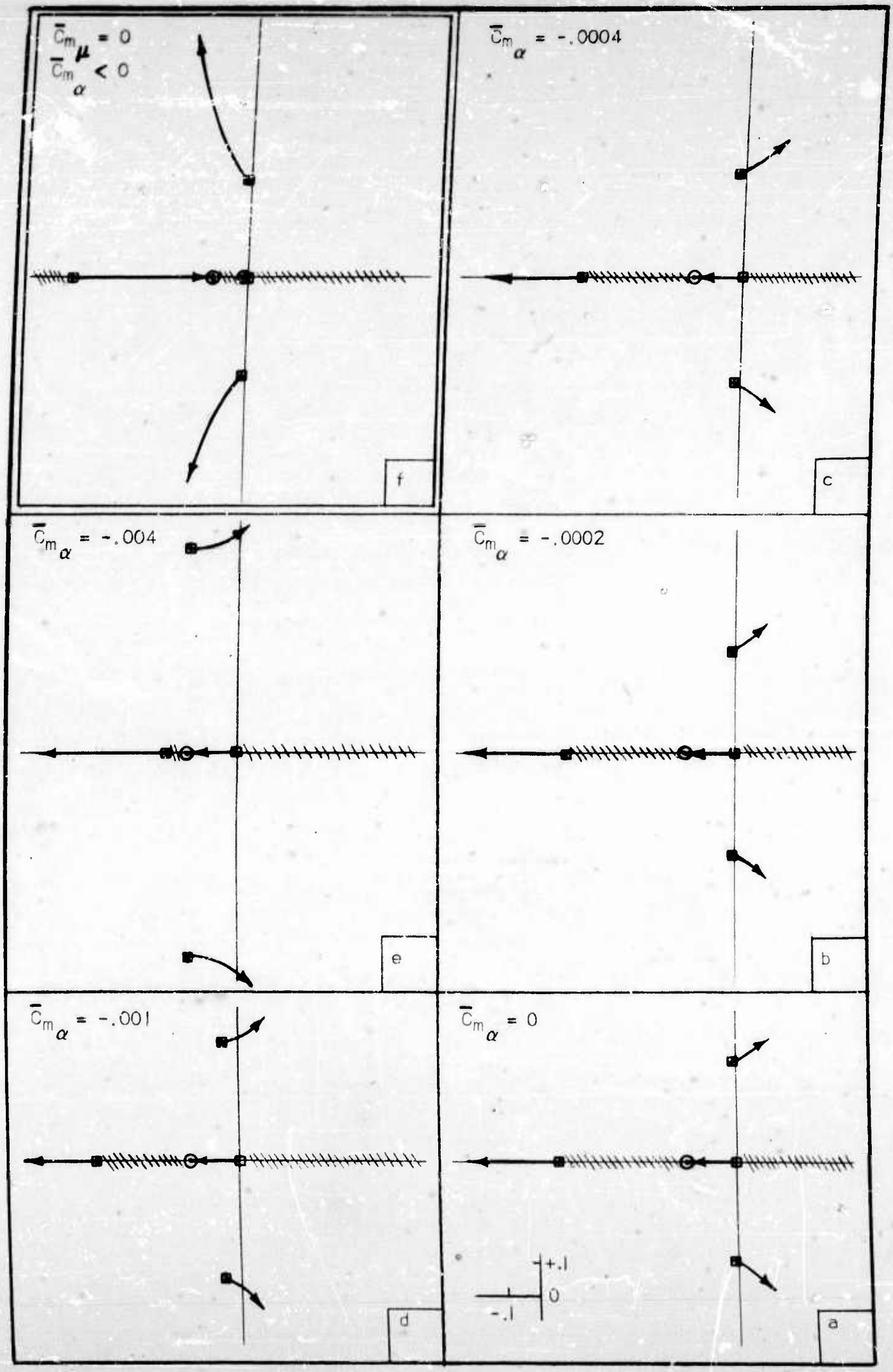

FIGURE 14 - II ROOT LOCUS S.C.D. $\mu = 0.10$ V = 36MPH. $\bar{C}_{m_\mu} > 0$

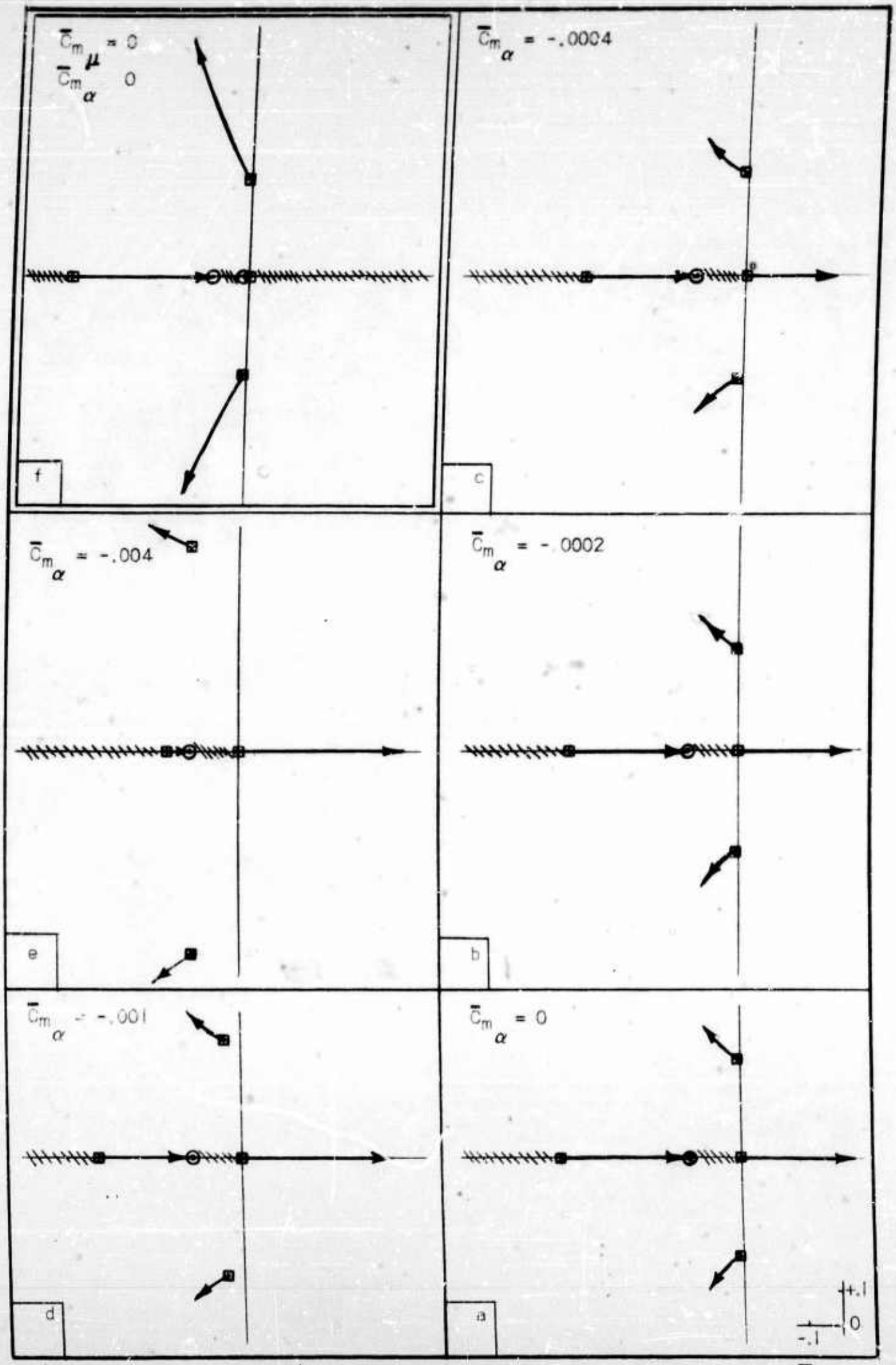

FIGURE 14 - III ROOT LOCUS S.C.D. $\mu = 0.10$ V = 35MPH $\bar{C}_{m_\mu} < 0$

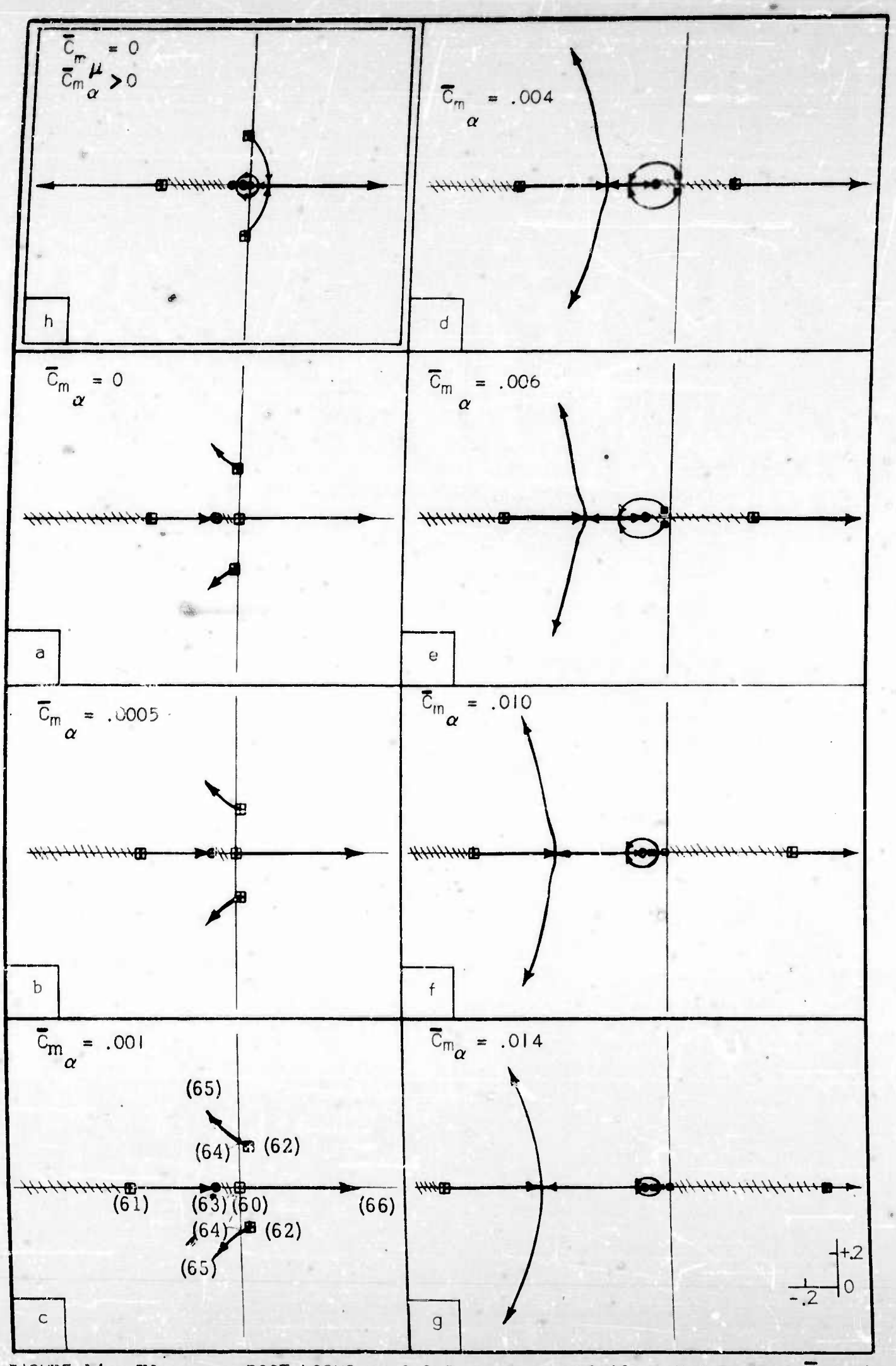

FIGURE 14 - IV ROOT LOCUS S.C.D. $\mu = 0.10$ V = 36MPH $\bar{C}_{m_\mu} < 0$

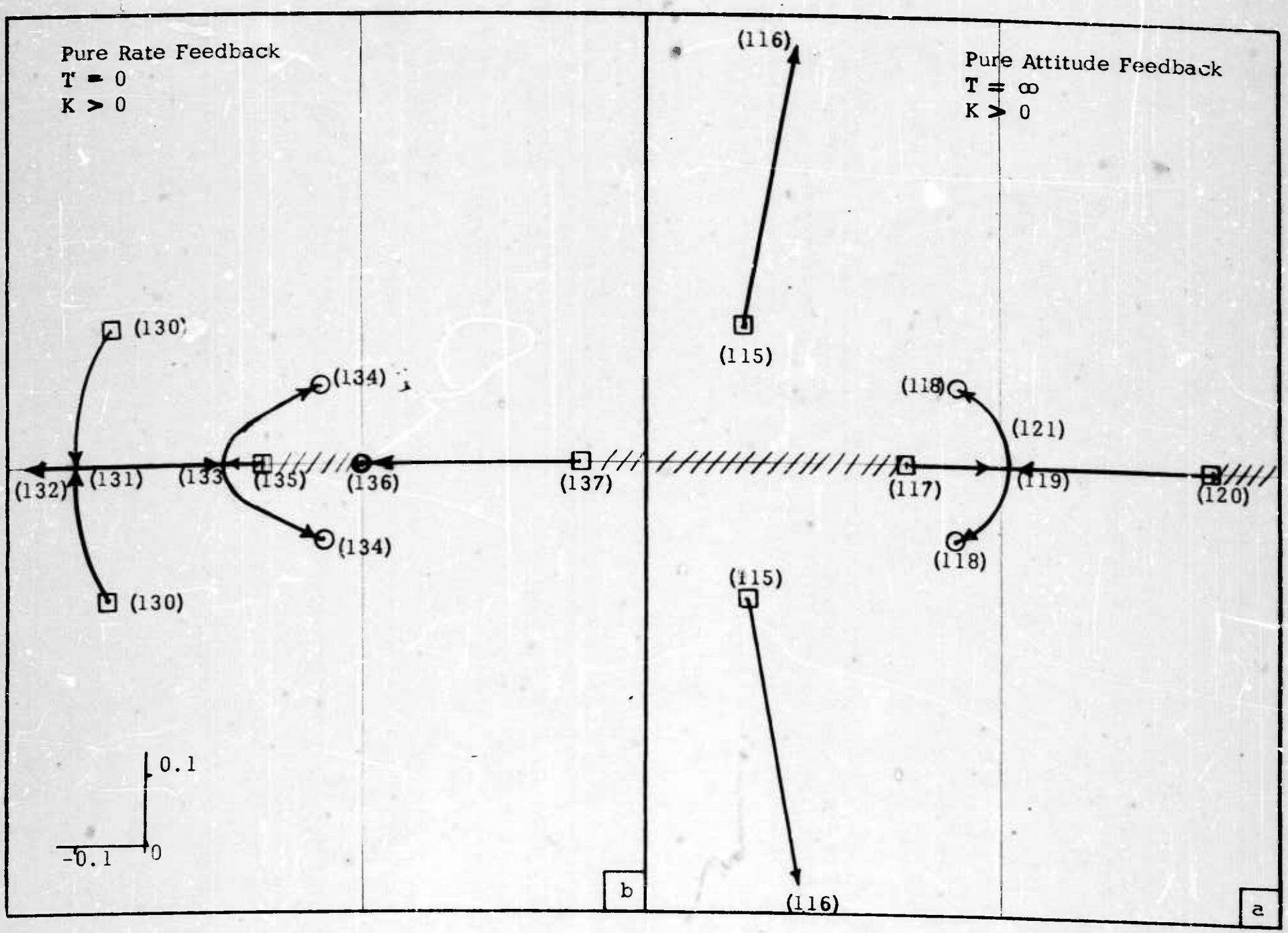

FIGURE 15 ROOT LOCUS S.C.D. $\mu = 0.10$ V = 36 MPH ARTIFICIAL STABILIZATION ADDED

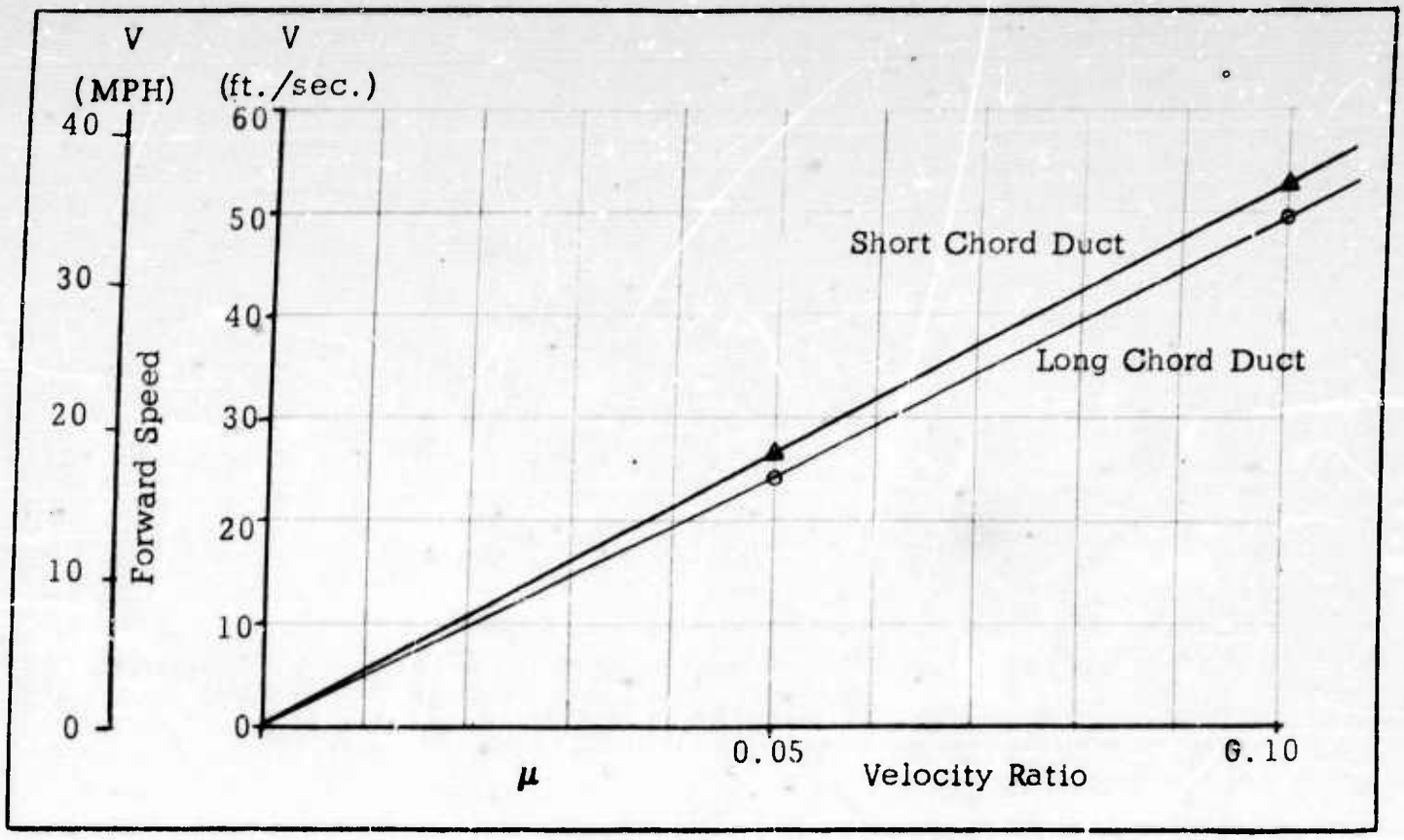

FIGURE 17 FORWARD SPEED VERSUS VELOCITY RATIO

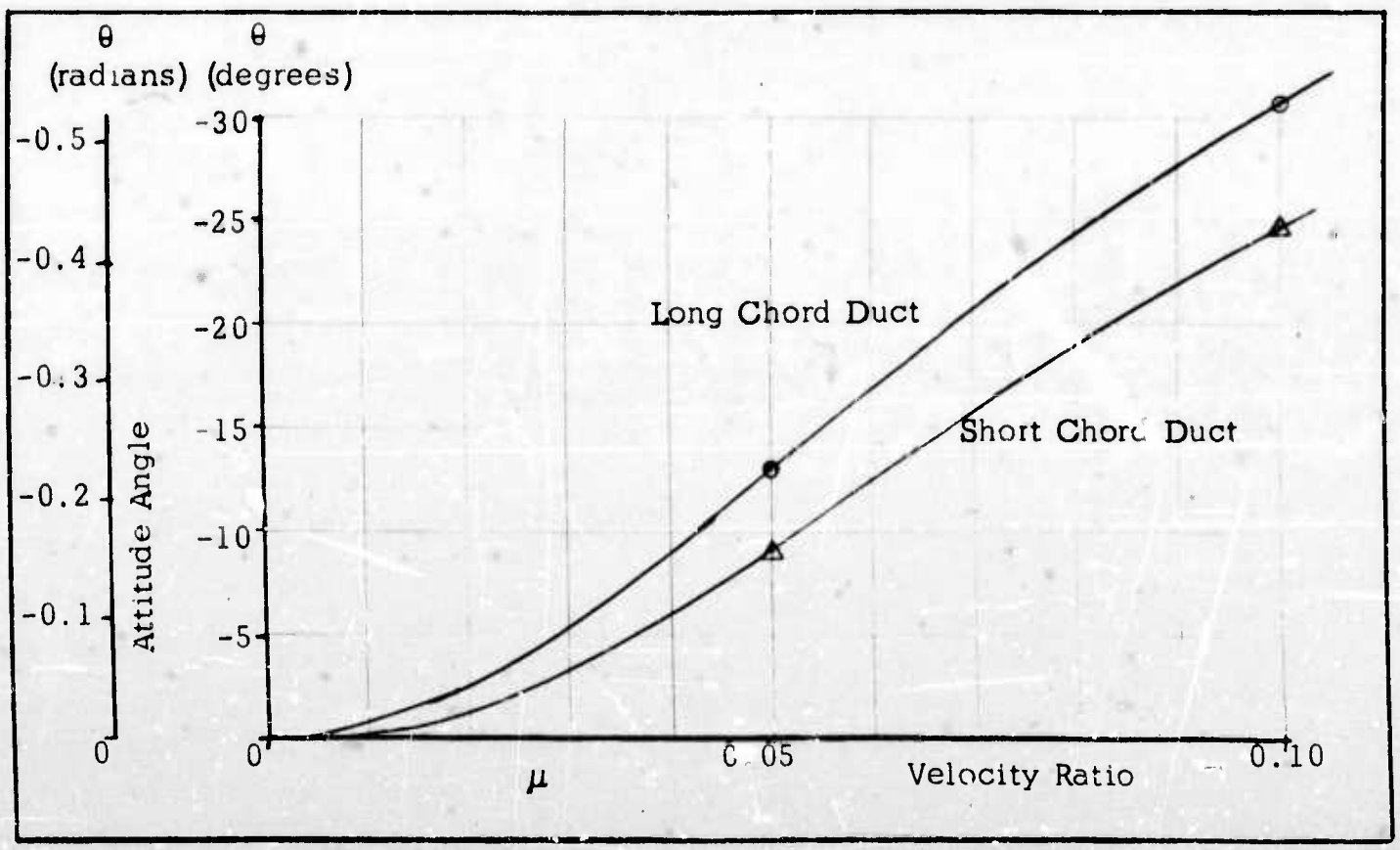

FIGURE 18 ATTITUDE ANGLE VERSUS VELOCITY RATIO

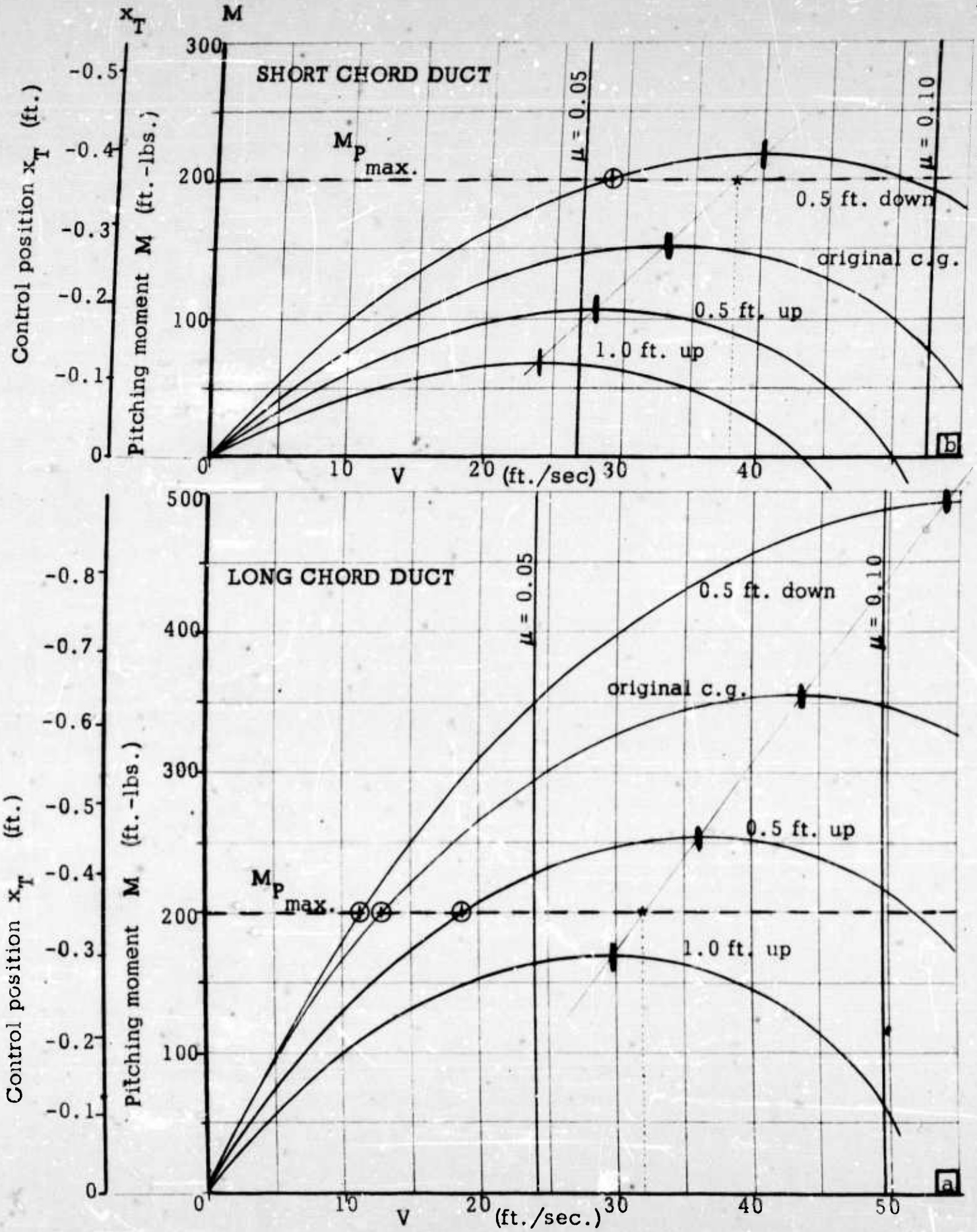

FIGURE 19 PITCHING MOMENT VERSUS FORWARD SPEED

APPENDIX I

EVALUATION OF STABILITY DERIVATIVES

The stability derivatives were evaluated from data obtained by wind tunnel tests conducted at the David Taylor Model Basin. A two foot diameter, 2/7 scale, model of a ducted-rotor Flying Platform was tested in the DTMB low-speed wind tunnel (Ref. 2). From the large variety of test runs made, portions of the data incorporating different duct designs were selected for the purpose of obtaining stability derivatives. The duct designs chosen were: one of relatively long chord length with a large leading edge radius, the other of shorter chord length and smaller leading edge radius (Fig. 2). The latter was chosen because it represented a considerable design change from the large leading edge, long chord duct.

The tests were conducted in the large settling chamber of the wind tunnel. The balance was designed so that forces were measured perpendicular and parallel to the rotor shaft and the moments were measured about the supporting structure.

The moment was arbitrarily transferred to the so-called quarter chord point of the duct. The forces and moments so measured were T, H and $M_{c/4}$ (Fig. 3).

All runs were made at constant velocity ratios as the angle of attack of the duct was varied. The tests were conducted principally at only three different velocity ratios, making accurate determination of derivatives with respect to μ somewhat difficult.

When summing all the forces and moments acting on the machine, it was necessary to include the drag force and moment caused by the pilot in addition to the forces and moments measured in the wind tunnel, (Fig. 3). This drag force, directed opposite and parallel to the relative wind, was

taken as acting through an assumed drag center of the pilot. In this report, the drag center for the typical pilot is located $3\frac{1}{3}$ feet above the pilot's feet.

Various methods are available to determine the drag coefficient or equivalent flat plate area of the pilot. A report published on the subject of airloads on human beings (Ref. 9), determines the drag coefficient of various men in standing positions. For the specific case of a six-foot, 200 pound, clothed man, standing erect, with arms and feet together, the equivalent flat plate area was determined as approximately nine and one half square feet. No attempt was made to modify this value due to the pilot stance with arms extended and feet apart, or to compensate for additional components, such as the cage around the pilot, instrumentation, fuel tanks, pilot helmet and equipment. It was felt that attempts to make accurate modifications on the drag of the pilot, in any way, would not be worthwhile unless investigations were made of the air flow to which the pilot is exposed. Therefore, for the purposes of this report, the value of the equivalent flat plate area of the pilot is assumed to be nine and one half square feet.

The original center of gravity position for the complete machine at normal gross weight was arbitrarily located at the pilot's stand-on platform or 0.42c above the top of the duct. Additional vertical center of gravity positions were selected above and below this original reference point (Fig. 16). All moments were resolved about these center of gravity locations and the stability derivatives evaluated for each case. (Table III).

The important requirement in the evaluation of the stability derivatives is that they be calculated at each initial, steady-state, equilibrium trim condition of the aircraft. For this steady flight condition, the sum of all the aerodynamic forces in the drag direction must be equal to zero and the sum of the forces in the lift direction must equal to the gross weight of the aircraft.

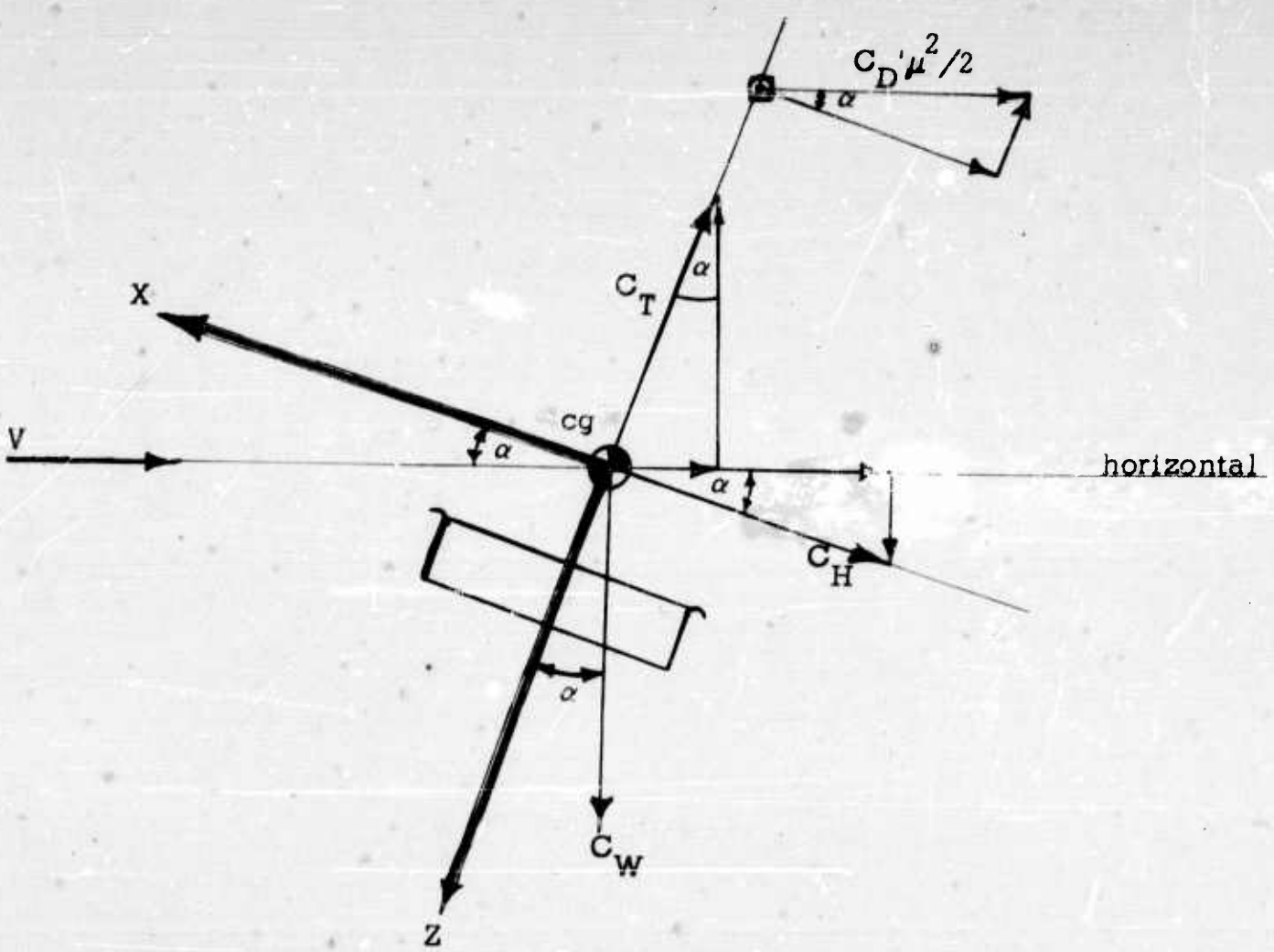

Fig. 20 Equilibrium Diagram

In Fig. 20 where α is a small angle, the summation of forces in the drag direction is:

$$\sum F_{HORIZONTAL} = -C_T \sin\alpha - C_H \cos\alpha - C_D' \frac{\mu^2}{2} = 0 \qquad (63)$$

This equation may be solved to determine the variation of the equilibrium angles of attack with forward speed.

Actually, this was accomplished graphically by plotting the horizontal force versus angle of attack for the various forward speeds (Fig. 21).

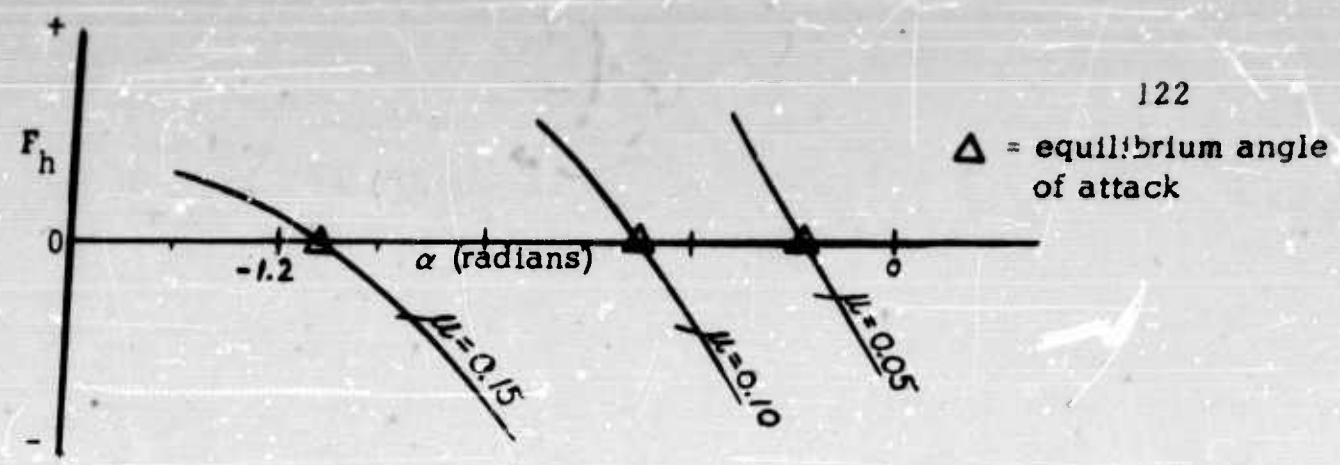

Fig. 21. Sketch of α versus F_h for various μ

Values of equilibrium angles plotted versus speed are shown for both ducts in Fig. 18 on page 117.

For vertical equilibrium in the initial steady-state level flight condition, (when the sum of the forces in the lift direction equals the gross weight) it is necessary to determine the variation of rotor angular velocity with forward speed from:

$$L = W = (+C_T \cos\alpha - C_H \sin\alpha)\, \rho\, \pi R^2 (\Omega R)^2 \qquad (64)$$

where R = 3.5 feet, W = 550 pounds and C_H, C_T and α are obtained from the wind tunnel data for the particular equilibrium angle and velocity ratio.

Then, for vertical equilibrium the actual flight speed may be determined from:

$$V = \mu\, \Omega R \qquad (65)$$

Actual values of ΩR at the various velocity or tip speed ratios are listed for both ducts in Table IV.

TABLE IV

ROTOR TIP SPEED (ft/sec) versus μ

Velocity Ratio	$\mu = 0$	$\mu = 0.05$	$\mu = 0.10$
ΩR Short Chord Duct	555	537	525
ΩR Long Chord Duct	488	478	495

When evaluating the stability derivatives, the forces and moments were put into coefficient form and plotted versus the angle of attack (measured in radians) and μ (dimensionless velocity ratio).

Typical sketches in the evaluation of the derivatives are shown in the following Figures.

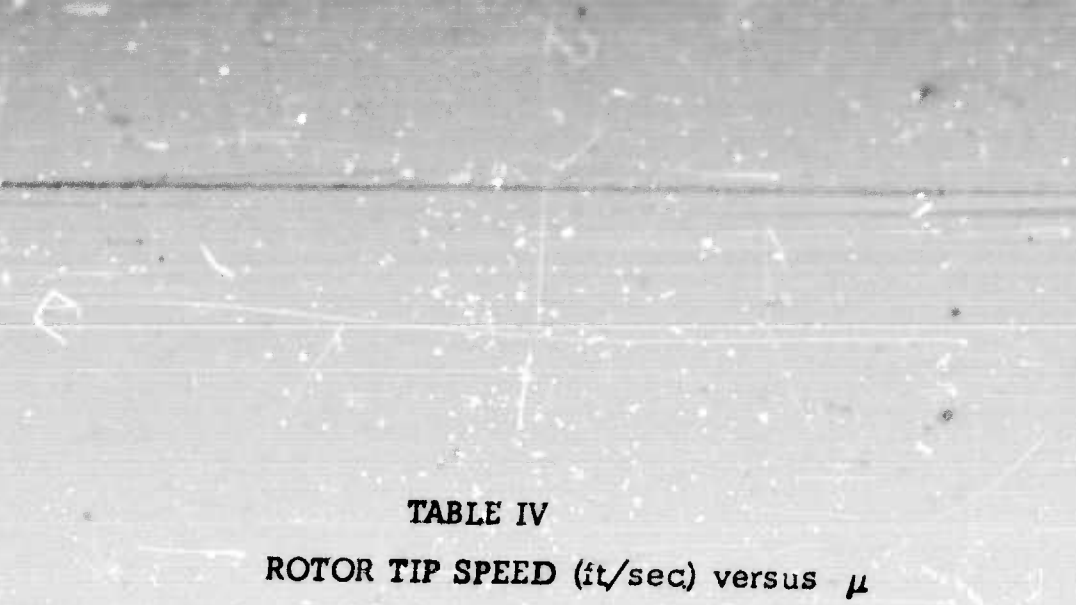

Fig. 22 Sketch of C_T versus α

The short vertical lines, on the constant μ curves, indicate the previously calculated equilibrium angles for each duct at each

velocity ratio. The stability derivative C_{T_α} must be evaluated at the equilibrium points by taking the slope of the curves at these points. Actual values of C_{T_α} versus μ are listed in Table V.

TABLE V

C_{T_α} versus μ

Velocity Ratio	$\mu = 0$	$\mu = 0.05$	$\mu = 0.10$
C_{T_α} Short Chord Duct	0	0.003	0.011
C_{T_α} Long Chord Duct	0	0.0047	0.0133

To obtain C_{T_μ} it is necessary to cross plot the former Figure of C_T versus α.

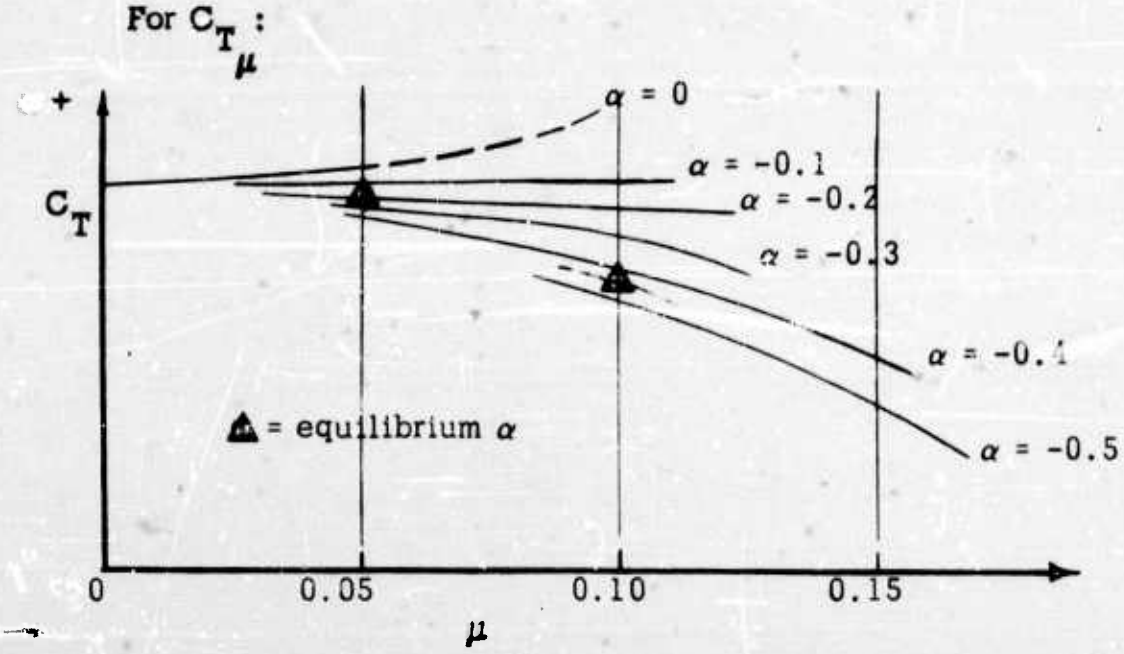

Fig. 23 Sketch of C_T versus μ

The stability derivative C_{T_μ} is obtained by taking the slope at the equilibrium angle for the particular μ.

Occasionally it was necessary to extrapolate in order to obtain the hovering values ($\mu = 0$) of derivatives taken with respect to μ. This can be avoided if more values at zero alpha are obtained at the higher μ or by additional data at lower velocity ratios.

Values of C_{T_μ} obtained from the data are listed in Table VI.

TABLE VI

C_{T_μ} versus μ

Velocity Ratio	$\mu = 0$	$\mu = 0.05$	$\mu = 0.10$
C_{T_μ} Short Chord Duct	0	0.044	0.016
C_{T_μ} Long Chord Duct	0	-0.004	-0.044

For C_{H_α} :

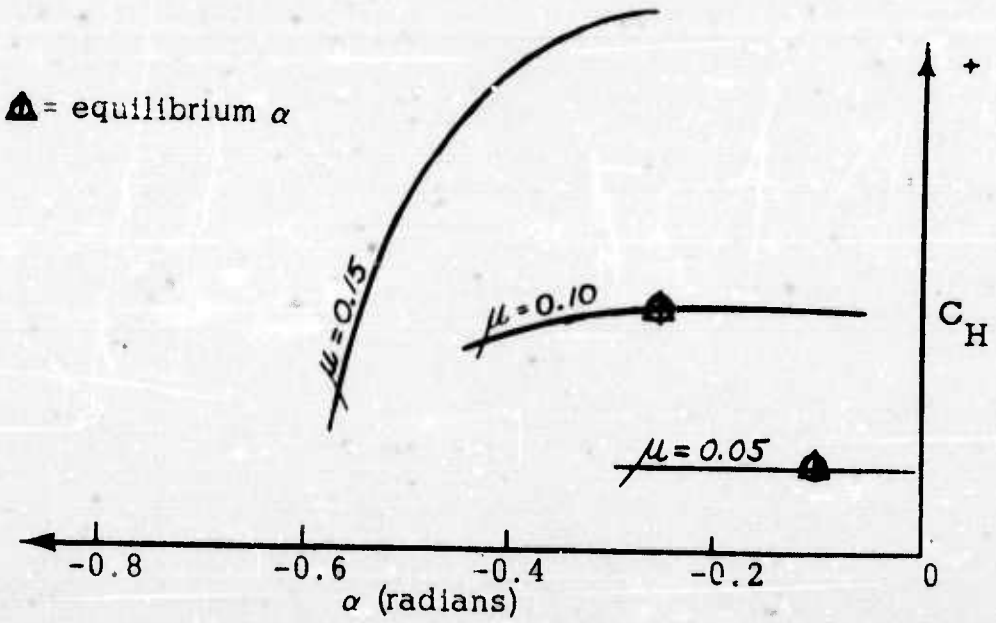

Fig. 24 Sketch C_H versus α

Equilibrium angles of attack for $\mu = 0.15$ were usually so large that they were not shown on the figures.

Values of C_{H_α} are listed in Table VII.

TABLE VII

C_{H_α} versus μ

Velocity Ratio	$\mu = 0$	$\mu = 0.05$	$\mu = 0.10$
C_{H_α} Short Chord Duct	0	0	0
C_{H_α} Long Chord Duct	0	0.0005	0.0015

Cross plotting for C_{H_μ} :

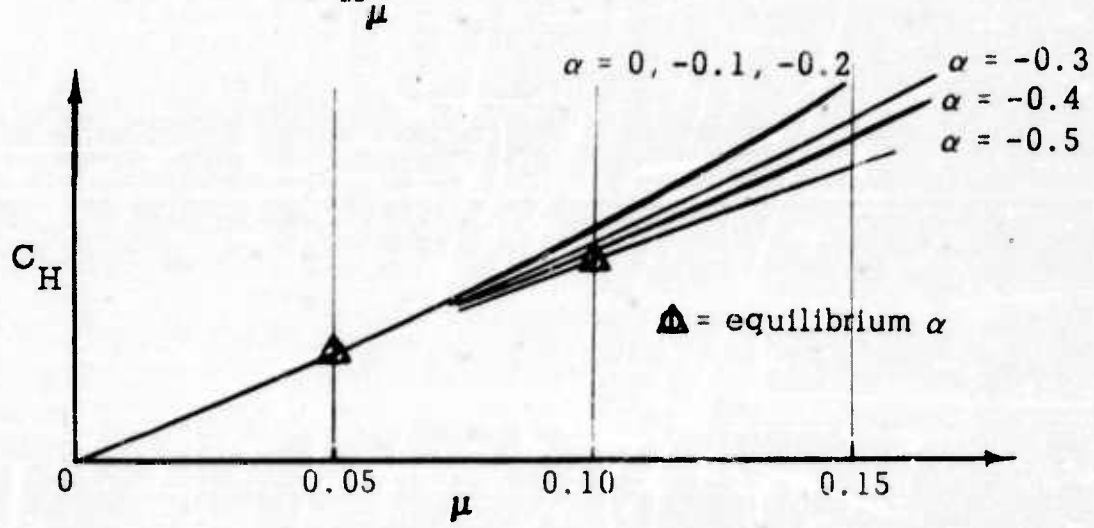

Fig. 25 Sketch of C_H versus μ

Values of C_{H_μ} are listed in Table VIII.

TABLE VIII

C_{H_μ} versus μ

Velocity Ratio	$\mu = 0$	$\mu = 0.05$	$\mu = 0.10$
C_{H_μ} Short Chord Duct	0.044	0.078	0.108
C_{H_μ} Long Chord Duct	0.118	0.118	0.136

For C_{m_α} :

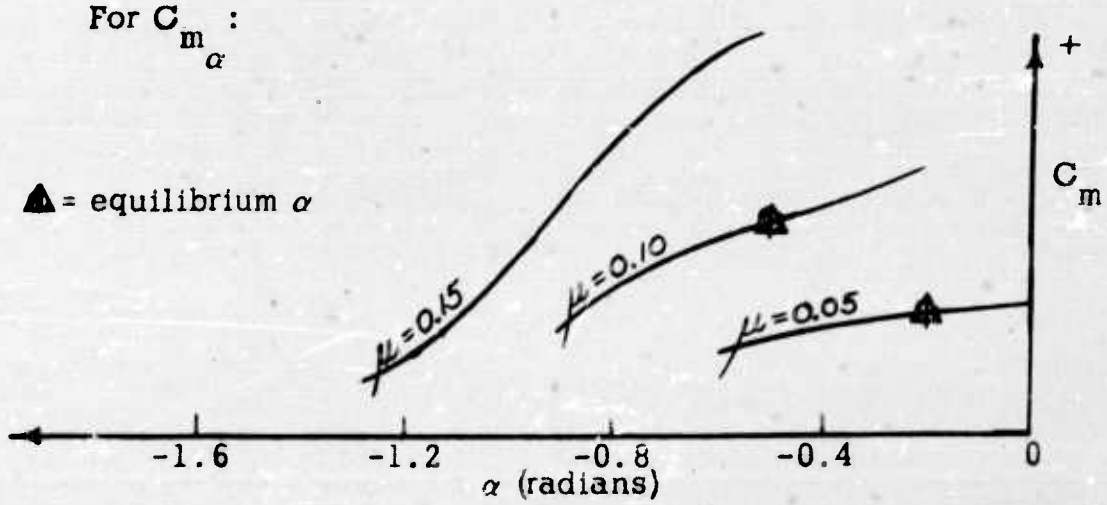

Fig. 26 Sketch of C_m versus α

Values for C_{m_α} are listed in Table IX.

TABLE IX

C_{m_α} versus μ

Velocity Ratio	0	0.05	0.10
C_{m_α} Short Chord Duct	0	0.00035	0.0023
C_{m_α} Long Chord Duct	0	0.0031	0.0046

Cross plotting for C_{m_μ}.

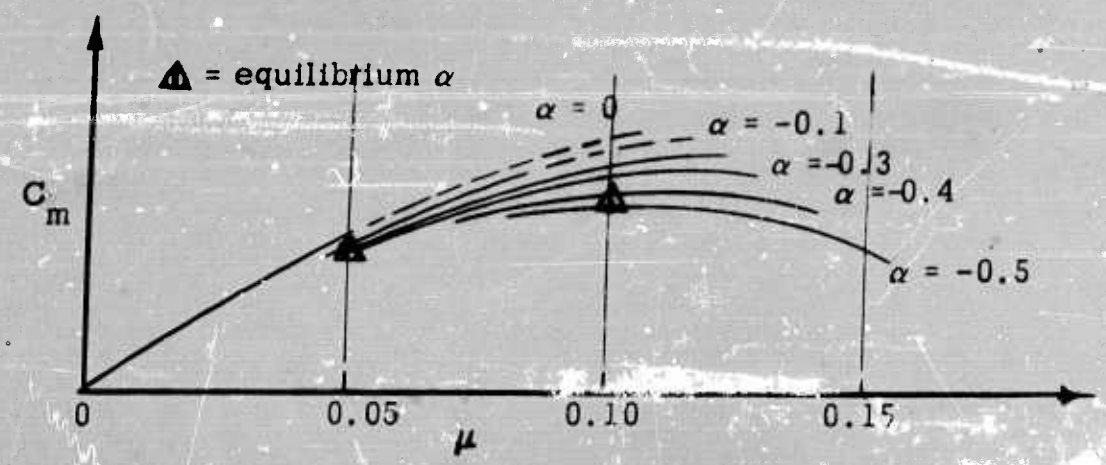

Fig. 27 Sketch of C_m versus μ

Values for C_{m_μ} versus μ are listed in Table X

TABLE X

C_{m_μ} versus μ

Velocity Ratio	$\mu = 0$	$\mu = 0.05$	$\mu = 0.10$
C_{m_μ} Short Chord Duct	0.055 (ext.)	0.03	-0.01
C_{m_μ} Long Chord Duct	0.2 (ext.)	0.06	0.044

The evaluation of the derivative $C_{H_{d(\Delta\theta)}}$ may be obtained by:

$$C_H = C_{H_\mu} \cdot \mu = C_{H_\mu} \cdot \frac{V}{\Omega R} \tag{66}$$

where:

$$V = (\Delta\dot{\theta}) \cdot (z_H) \tag{67}$$

therefore:

$$\frac{\partial C_H}{\partial(\Delta\dot{\theta})} = C_{H_\mu} \cdot \frac{z_H}{R\Omega}$$

$$\frac{\partial C_H}{\partial[d(\Delta\theta)]} = C_{H_\mu} \cdot \frac{z_H}{R} \cdot \frac{1}{\Omega\tau} \equiv C_{H_{d(\Delta\theta)}} \tag{68}$$

Values for $C_{H_{d\ (\Delta\theta)}}$ using the appropriate values of $C_{H_{\mu}}$, Ω, $z_{H/R}$, and τ are listed in Table XI.

TABLE XI

$C_{H_{d\ (\Delta\theta)}}$ versus μ

Velocity Ratio	$\mu = 0$	$\mu = 0.05$	$\mu = 0.10$
$C_{H_{d(\Delta\theta)}}$ Short Chord Duct	0.000275	0.000486	0.000673
$C_{H_{d(\Delta\theta)}}$ Long Chord Duct	0.000735	0.000735	0.000848

In the equations of motion the drag terms (Terms 5, 6 and 7 on page 19) are developed as a result of the drag of the pilot and may be evaluated directly. Their form in the equations may also be seen in Fig. 20 where the coefficient form of this force (acting parallel to the relative wind) is $\mu^2 C_D'/2$ (Eq. 13).

Using the small angle assumptions, the pilot drag force, $\mu^2 C_D'/2$ is resolved into components along the body axes. The derivatives are taken with respect to μ and α and must be evaluated at the initial condition, $\mu = \mu_o$ and $\alpha = \alpha_o$.

X component: $\frac{\mu^2}{2} C_D'$

Z component: $\frac{\mu^2 \alpha}{2} C_D'$

Taking the derivatives:

X axis: $\frac{C_D'}{2} \frac{\partial}{\partial \mu} (\mu^2) = \mu C_D' \Big|_o = \mu_o C_D'$

$\frac{C_D'}{2} \frac{\partial}{\partial \alpha} (\mu^2) = 0$

Z axis:

$$\frac{\alpha C_D'}{2} \frac{\partial}{\partial \mu} (\mu^2) = \alpha \mu C_D' \Big|_o = \alpha_o \mu_o C_D'$$

$$\frac{\mu^2 C_D'}{2} \frac{\partial}{\partial \alpha} (\alpha) = \frac{\mu^2}{2} C_D' \Big|_o = \frac{\mu_o^2}{2} C_D'$$

The forces in coefficient form are obtained by multiplying these terms by their respective perturbations:

H-force contribution: $\mu_o C_D' \Delta\mu$ (Term 5 page 19)

Thrust force contributions: $\alpha_o \mu_o C_D' \Delta\mu$ (Term 6 page 19)

$\frac{\mu_o^2}{2} C_D' \Delta\alpha$ (Term 7 page 19)

APPENDIX II

The remaining stability derivative to be evaluated is the over-all pitch damping derivative $\bar{C}_{m_{d(\Delta\theta)}}$ (Eq. 21g).

$$\bar{C}_{m_{d(\Delta\theta)}} = C_{m_{d(\Delta\theta)}} - \frac{z_H}{R} C_{H_{d(\Delta\theta)}} \qquad (21g)$$

The total damping moment in pitch for the unstabilized Flying Platform includes contributions from three sources, namely:

1. The pitch damping moment due to the change in H-force with pitch rate, $\frac{z_H}{R} \cdot C_{H_{d(\Delta\theta)}} \cdot d(\Delta\theta)$.
2. The pitch damping moment of the rotor due to a pitch rate.
3. The pitch damping moment of the duct due to a pitch rate.

Contributions (2) and (3) taken together are equal to the first term $C_{m_{d(\Delta\theta)}}$ in Eq. 21g.

Contribution (1) is obtained by solving Eq. 68 for $C_{H_{d(\Delta\theta)}}$

$$C_{H_{d(\Delta\theta)}} = C_{H_\mu} \cdot \frac{z_H}{R} \cdot \frac{1}{\Omega\tau} \qquad (68)$$

The values of C_{H_μ}, z_H, Ω, R and τ are all known. Then the pitch damping moment contribution due to change of H-force with pitch rate is:

$$\frac{z_H}{R} \cdot C_{H_{d(\Delta\theta)}} \cdot d(\Delta\theta) \qquad \text{(Term 17 page 21)}$$

Contribution (2) is obtained by using the expression developed in the Appendix of Ref. 4 for the moment generated by the rotor due to a pitch rate.

$$C_{m_{ROTOR}} = - \frac{abc_R(\Delta\dot{\theta})}{16\pi\Omega R}$$

$$C_{m_{d(\Delta\theta)_{ROTOR}}} = - \frac{abc_R\rho R^2}{16 W}$$

where c_R is the average chord of the rotor blade.

Contribution (3); the pitch damping moment of the duct due to a pitch rate may be derived in various ways.

The moment produced by this contribution is equal to the time rate of change of angular momentum. For a constant pitch rate, this is equal to the time rate of change of moment of inertia of the slipstream at the duct exit which is equal to the rate of mass flow times the square of the radius of gyration for the duct exit area about the pitching axis.

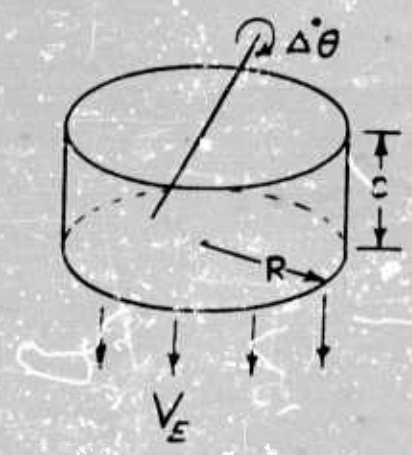

($\Delta\dot{\theta}$) - pitch rate about Y axis at top of duct.

πR^2 - duct exit area

c - duct chord length

V_E - slipstream velocity at duct exit.

This gives:

$$M = - \frac{d}{dt}(I\omega) = -(\Delta\dot{\theta})\frac{dI}{dt}$$

$$M = -(\Delta\dot{\theta})(\rho\pi R^2 V_E)\left(\frac{R^2}{4} + c^2\right)$$

where:

$\rho\pi R^2 V_E$ = rate of mass flow

$\frac{R^2}{4} + c^2$ = square of the radius of gyration for the duct exit area

The duct exit velocity is equal to (See Appendix III):

$$V_E = \sqrt{\frac{T}{\pi R^2 \rho}} = \Omega R \sqrt{C_T}$$

Therefore the pitch damping moment in coefficient form is:

$$C_m = -\frac{(\Delta\dot{\theta})\rho\pi R^2 \Omega R \sqrt{C_T}}{\rho\pi R^2 (\Omega R)^2 R}\left[\frac{R^2}{4} + c^2\right]$$

$$C_m = -\frac{(d\Delta\theta)\sqrt{C_T}\,\rho\pi R^2 R}{m}\left[\frac{1}{4} + \frac{c^2}{R^2}\right]$$

The pitch damping derivative is:

$$C_{m_{d(\Delta\theta)}} = -\frac{\sqrt{C_T}}{w}\left[\frac{1}{4} + \frac{c^2}{R^2}\right]$$

where w is equal to the aircraft relative density factor $m/\rho\pi R^2 R$.

For the long chord duct when R = 3.5 ft. and c = 1.75 ft, $c^2/R^2 = 1/4$.

The expression for contribution (3) is:

$$C_{m_{d(\Delta\theta)_{DUCT}}} = -\frac{\sqrt{C_T}}{2w}$$

The sum of the three moment contributions gives the total theoretical pitch damping moment used in this Report.

It is recognized that this theoretical pitch damping moment is probably too large, since it is not very likely that all three contributions provide their full theoretical value for the cases of the relatively short chord ducted rotors studied. In any event, this total value appears to be small compared to the amount required to produce desirable stability characteristics. Therefore, the stability characteristics together with the effects produced by additional damping were investigated and are discussed in this Report.

APPENDIX III

The expression for duct exit velocity may be developed from the so-called simple momentum theory of ducted-propellers by utilizing the common assumption that the velocity of the air at the duct exit is equal to the final slipstream velocity ($V_{exit} = V_\infty$).

The analysis is restricted to the inviscid, incompressible, static case and utilizes the ideal ducted propeller combination with an "actuator disk" and a simple cylindrical shroud.

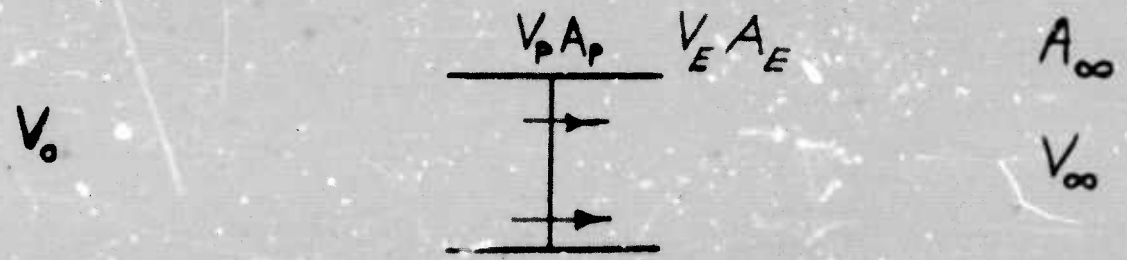

The velocity V is the same on both sides of the actuator disk because of the requirement of continuity.

The total thrust is:

$$T = \rho A_P V_P \cdot V_\infty$$

Utilizing the assumption of no slipstream contraction for a ducted propeller $A_P = A_E = A_\infty$.

By continuity:

$$A_P V_P = A_\infty V_\infty$$

$$T = \rho A_\infty V_\infty^2$$

$$T = \rho A_E V_E^2$$

$$V_E = \sqrt{\frac{T}{\rho A_E}}$$